Qiang Chen

Nanomechanics of Hierarchical Cellular Solids

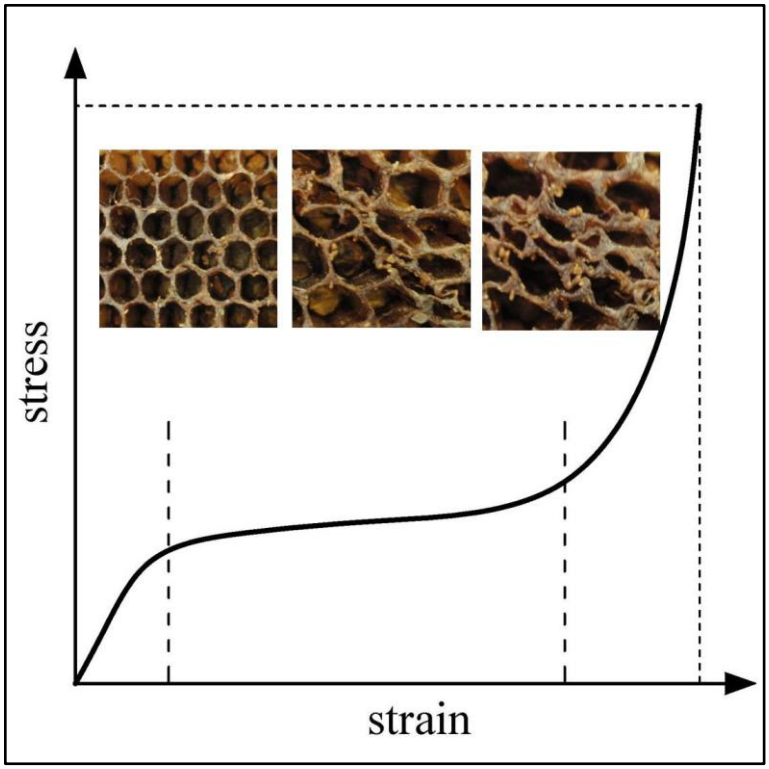

Dottorato di Ricerca in Ingegneria delle Strutture
Politecnico di Torino

Qiang CHEN

Nanomechanics of Hierarchical Cellular Solids

Tesi per il conseguimento del titolo di Dottore di Ricerca
XXIV Ciclo (A.A. 2008/09; 2009/10; 2010/11)

Dottorato di Ricerca in Ingegneria delle Strutture
Politecnico di Torino

Decembre 2011

Dottorato di Ricerca in Ingegneria delle Strutture
Politecnico di Torino
10129 Torino, Italia
Tutore: Prof. Nicola M. Pugno
Coordinatore: Prof. Alberto Carpinteri

Alla Mia Famiglia

To My Family

Acknowledgements

I am indebted to my tutor Prof. Nicola M. Pugno for his continuous supervision, and encouragement in the three-year PhD programme. He sets an excellent example to me and I am inspired by his pursuit on Science. Thanks also go to Chinese government. Without its support, I would not have a chance to study here. Also, I thank Southeast University in China, where I studied before and Politecnico di Torino in Italy. It is the cooperation between them that makes me become a qualified doctor. I want to express my gratitude to the members in our group, Abdalrahman Tamer, Lepore Emiliano, Sun Youngtao and all those who helped me in the past three years. Thanks my parents and my sister for their support and to my fiancée, who stands by me as always.

Contents

SUMMARY ..... **V**

1 INTRODUCTION **1**

1.1 INTRODUCTION 1
1.2 NACRE/SEASHELL 3
1.3 GECKO FEET 9
1.4 SPIDER SILK 14
1.5 EXOSKELETONS OF LOBSTERS/CRABS 20
1.6 ARMADILLO SHELL 22
1.7 TURTLE SHELL 26
1.8 PLANT STEM 29

2 HIERARCHICAL WOVEN TISSUES: ELASTICITY **35**

2.1 INTRODUCTION 35
2.2 MATRIX TRANSFORMATION AND STIFFNESS AVERAGING 39
2.3 GENERAL HIERARCHICAL THEORY 44
2.4 SELF-SIMILAR HIERARCHICAL STRUCTURES 47
2.4.1 Self-similar case (1) *47*
2.4.2 Self-similar case (2) *49*
2.4.3 Orthogonal yarns for both self-similar hierarchical structures *50*
2.4.4 Parametric Analysis *51*
2.4.5 Comparison between self-similar cases (1) and (2) *57*
2.5 INFLUENCE OF CONSTITUENTS ON OVERALL ELASTICITY OF TENDONS 58
2.5.1 Volumetric fractions of collagen and matrix *58*
2.5.2 Influence of different variables *58*
2.5.3 Influence of collagen orientation *60*
2.5.4 Influence of the total volume of collagen *62*
2.6 EXPERIMENTS ON THE AECHMEA AQUILEGIA LEAF 62
2.6.1 Experimental procedure *62*
2.6.2 Experimental results and discussion *63*

2.6.3 Prediction of the hierarchical theory *63*

3 HIERARCHICAL HONEYCOMBS: ELASTICITY **67**

3.1 INTRODUCTION 67
3.2 SURFACE EFFECT 70
3.3 ELASTIC CONSTANTS OF HIERARCHICAL NANO-HONEYCOMBS 71
3.3.1 Deflection of an orthotropic beam with surface effect *71*
3.3.2 "Bottom up" method to calculate material constants *72*
3.3.3 Stiffness efficiency *76*
3.4 ELASTIC BUCKLING OF HIERARCHICAL HONEYCOMB MATERIALS 77
3.4.1 Buckling load of the orthotropic beam with surface effect *77*
3.4.2 "Bottom up" method to calculate buckling loads with surface effect *77*
3.4.3 Strength efficiency *79*
3.5 PARAMETRIC ANALYSIS AND DISCUSSION 79
3.5.1 Linear-elastic analysis *79*
3.5.2 Buckling analysis *80*
3.5.3 Discussion *81*

4 HIERARCHICAL HONEYCOMB: ELASTIC BUCKLING **83**

4.1 INTRODUCTION 83
4.2 ELASTIC BUCKLING OF HIERARCHICAL HONEYCOMB 87
4.2.1 Euler buckling formula for orthotropic beams/columns *87*
4.2.2 "Top down" method to calculate buckling loads *87*
4.2.3 Local buckling load of the whole hierarchical structure *93*
4.2.4 Strength efficiency *93*
4.3 PARAMETRIC ANALYSIS 94
4.3.1 Local buckling stress *94*
4.3.2 Strength efficiency *96*
4.3.3 Progressive buckling collapse *97*
4.3.4 Constitutive laws and deformation energy *99*

5 HIERARCHICAL HONEYCOMB: STRENGTH AND TOUGHNESS **101**

5.1 INTRODUCTION 101
5.2 SURFACE EFFECT AND QUANTIZED FRACTURE STRENGTH 103

5.2.1 The surface effect *103*
5.2.2 The quantized fracture strength *104*
5.3 STRENGTH AND TOUGHNESS OF HIERARCHICAL HONEYCOMB 105
5.3.1 The effective strength of constituent materials (level 0) *105*
5.3.2 The effective strength and toughness of hierarchical honeycomb *106*
5.3.3 Relative-density ratio *112*
5.4 EXAMPLE AND DISCUSSION 113

6 HIERARCHICAL FOAM: ELASTICITY AND STRENGTH 115

6.1 INTRODUCTION 115
6.2 SURFACE EFFECT 117
6.3 YOUNG'S MODULUS 118
6.4 PLASTIC STRENGTH 122
6.4.1 Effective yield strength *122*
6.4.2 Analytic results *125*

7 CONCLUSIONS AND OUTLOOKS 129

BIBLIOGRAPHY 133

Summary

Materials Science and Engineering, a young and vibrant discipline with its inception in the 1950s, has expanded into three directions: metals, polymers, and ceramics (and their mixtures, composites). Beyond the traditional scope, biological materials have drawn much attention since 1990s due to their optimal structures, which rise from hundreds of million years of evolution. Generally, biological materials are complex composites and possess varieties of hierarchical structures, multifunctionality, self-organization and self-assembly. From the point of view of mechanics, mechanical properties of natural (or biological) materials are outstanding, although their constituent materials are weak. This is because the necessary mechanical support is in great need due to their surrounding environment. Therefore, their efficiency provides us with useful indications as to how to synthesize new materials inspired by natural ones, and thus drives scientists and engineers to reveal the mechanisms behind the observed phenomena of interest. In this regard, the tendency in the design of novel materials apparently holds a promising future in new Material Science. To date, it is widely accepted that the research on biological materials is a multidisciplinary field including chemistry, physics, and biology etc. Although some progress has been already made, there is still a long way to go to mass fabricate bio-inspired materials.

In this thesis, employing a "bottom-up" approach, we have devised three hierarchical models (2-D hierarchical woven, 2-D hierarchical honeycomb and 3-D hierarchical foam) inspired by structures found in natural materials and investigated their mechanical properties. The common characteristic of these structures is their being quasi-self-similar. Regarding the derivation of their mechanical properties, we consider the $(n\text{-}1)^{th}$ level structure to be a continuous medium and from it we calculate the mechanical properties of the n^{th} level structure.

In the first chapter, we introduce the motivation for this work. By reviewing the literature on both well-studied and less familiar natural materials, we summarize their structural characteristics and biomechanical mechanisms.

Chapter 2 deals with our first model—1-D or 2-D hierarchical woven tissue, and the elastic anisotropy of the structure is derived, based on the well-known stiffness averaging method by volumes. In order to verify the theory, an experiment on leaves,

which are modeled as one-dimensional hierarchical woven structures, is performed. Also, a comparison between theoretical predictions and experimental data on tendons from the literature is made. The considered structure could be used as a scaffold, which can provide the mechanical support and optimize tissue regeneration at each hierarchical level.

Chapters 3-5 discuss our second model—2-D hierarchical honeycomb. Incorporating the surface effect, the in-plane linear-elastic properties, elastic buckling properties, fracture strength and toughness are derived. Chapter 3 examines the linear elastic properties and the stiffness efficiency thanks to the minimum-weight analysis, and the parametric analysis shows that the structure can be optimized. Chapter 4 discusses elastic buckling by employing the Euler buckling formula; besides local buckling, progressive buckling is also investigated. The progressive failure behavior is found to be similar to that of *balsa* wood. Strength efficiency is also illustrated. Employing "Quantized Fracture Mechanics" (Pugno, 2002; Pugno and Ruoff, 2004), Chapter 5 modifies the classical strength formulas of the conventional honeycomb and investigates the defective hierarchical honeycomb; the fracture toughness of the perfect and defective hierarchical honeycomb are both derived. In general, hierarchical honeycombs can be used as energy-absorbing materials and bioscaffolds for directional tissue regeneration.

Chapter 6 models our third hierarchical structure—3-D hierarchical foam. The Young's modulus and plastic strength are derived based on structural analysis. When the characteristic size of the lowest level is very small (less than 10nm), surface effects play an important role in determining the mechanical properties of the structure. The hierarchical foam could be used as nano-porous gold.

Chapter 7 provides conclusions and an outlook for future work.

Chapter 1

Introduction

Natural selection and evolution develop a huge amount of biological materials in different environment (e.g. lotus in water and opuntia in desert). These biological materials possess many inspiring properties, which hint scientists and engineers to find some useful clue to create new materials and thus enrich the existing materials system. In this part, we highlight some well-studied (e.g. nacre shell) and newly-studied (e.g. turtle shell) natural materials, and summarize their hierarchical structures and mechanisms behind their mechanical properties, from animals to plants. These fascinating mechanisms suggest researchers to investigate natural materials deeply and broadly and to design and fabricate new bioinspired materials to serve our life.

1.1 Introduction

Nature, acting as a stealth hand, cultivates and shapes all lives in the planet (Thompson, 1945). It provides a huge amount of biological materials with different functions, such as, abalone nacre (Curry, 1977), crab exoskeleton (Chen et al., 2008), turtle shell (Rhee et al., 2009), armadillo shell (Chen et al., 2011), and gecko feet (Autumn et al., 2000). Several decades ago, most of these biological materials were explored only by biologists. However, since Material Science and Engineering (MSE), a vibrant discipline, emerged in 1950s, biological materials are being added to its interest from 1990s and have drawn much attention from material scientists and engineers due to their fascinating multifunctions (self-organization, self-assembling, self-healing, self-cleaning, etc) (Meyers et al., 2008). From a mechanical point of view, the natural materials usually exhibit many inspiring properties, e.g. light-weight,

high-toughness (Ritchie et al., 2009), mechanical-efficiency, e.g. higher stiffness-to-density (Wegst and Ashby, 2004), flexible-switch attaching and detaching (Tian et al., 2006), and self-cleaning properties (Cheng et al., 2006), etc. In particular, nacre shell, with brittle biomineralized tablets but small percent of organic matrix, has excellent mechanical properties (Jackson et al., 1988; Schäffer et al., 1997; Kamat et al., 2000; Lin et al., 2006; Espinosa et al., 2011), and its toughness is approximately 3000 times greater than that of a single crystal (Song et al., 2003); Bejan (1996) proposed a law for the occurrence of shape and structure configuration; after that, employing the law in minimizing the body heat loss and blood pumping power, and he predicted the proportionality between metabolic rate and body mass to the power 3/4 (West et al., 1997; Bejan, 2001, 2005 ; Guiot et al., 2006; Guiot et al., 2007; Pugno et al., 2008; Delsanto et al., 2008; Delsanto et al., 2009).

Even though natural materials, e.g. bone, show various abilities to adapt to the ambient environment (Srinivasan et al., 1991), they possess only two major constituents, i.e., biopolymer and biomineral, which are made of several fundamental elements, primarily C, N, Ca, H, O, Si (Chen et al., 2008; Meyers et al., 2008); the two constituents are often quite weak compared with their final smart "products" (Fratzl and Weinkamer, 2007). Then, questions rise: Why nature can build so strong/tough materials and structures with so weak constituents? Why natural materials have a variety of structures and functions, e.g. difference between bones and tendons, though they have same constituent? What is the structure-function relationship behind these properties? Although Wegst and Ashby (2004) have established the elevation indices, presenting them as materials property charts/Ashby map for natural materials, how nature develops the mechanical efficiency of natural materials is still unknown. With these doubts, material scientists and engineers are devoting themselves to dig the principles and mechanisms out (Smith et al., 1999; Autumn and Peattie, 2002; Qin et al, 2009; Nova et al., 2010) and try to pave a way to fabricate bio-mimetic materials. In this point, Fratzl (2007) provided a guideline to realize the process, which is categorized into three steps: 1) Elucidating structure-function relationships of biological materials; 2) Extracting the physical/chemical principles of the relationships; 3) developing manufacturing technologies to synthesize bioinspired materials.

To date, an abundant of experimental observations and developed theories on different natural materials are obtained, such as recent development on gecko (Autumn, et al. 2006; Pugno and Lepore, 2008a, 2008b;Varenberg et al., 2010), nacre (Espinosa

et al., 2011), Armadillo armor (Chen et al., 2011). These studies show that the hierarchical structures at many length scales, from nanoscale to macroscale, determine the functions of natural materials, and the structure at each hierarchical level optimized by Nature; this point is widely accepted now. Lakes (1993) reviewed some materials with structural hierarchy, which included man-made structures, e.g. the Eiffel tower, natural materials, e.g. tendon and hierarchical cellular solids, e.g. honeycomb. Recently, Fratzl and Weinkamer (2007) summarized some works on several natural cellular materials (bone, wood, and glass sponge skeletons) and an elastomer (tendon) about the basic principles, which dominate their mechanical properties; Buehler et al. (2008) focused on protein materials (e.g. spider silk) and employed multiapproaches (especially, large-scale atomistic simulations) to study and understand dynamic and fracture mechanisms that happen at nano- or meso-scale; furthermore, starting with the basic building blocks, i.e. biominerals, proteins and polysaccharide, Meyers et al. (2008) illustrated systematically the growth mechanism and hierarchical structures of the four types of natural materials, which are divided according to Wegst and Ashby (Wegst and Ashby, 2004); Currey (2010) reviewed some less familiar bony tissues, e.g. deer's antler; Bhushan and Jung (2011), addressing the properties of natural and biomimetic surfaces, reviewed the latest achievement and development.

In this chapter, we focus ourselves on the selected natural materials and concisely, summarize the biomimetic mechanisms. Nacre shell and gecko foot are well-known natural materials and have been studied for a very long time; here, we choose some classical and recent literature to discuss respectively the toughness and contact mechanisms. As for the exoskeleton of lobster or crab, armadillo shell, turtle carapace and plant stem, new developments on these studied objects are reviewed; the light-weight but mechanical–efficiency cellular structures are unveiled, and, the biomechanical mechanisms for them are illustrated. This chapter does not have the aim to present a complete review but rather to discuss some new results.

1.2 Nacre/Seashell

Nacre shells (Fig. 1.1) are comprised of aragonite platelets and organic matrices, and exhibit two-level crossed lamellar micro-architectures (Pugno, 2006); aragonite platelets (about 5~8 μm in diameter and about 0.5 μm in thickness) act as "brick" with

weight fraction 95~97% and organic matrices (about 20~30 nm thick) as “mortar” with weight fraction 3~5% (Curry, 1977; Stempfl é et al., 2010). The function of the platelet is increasing the structural stiffness and hardness; the function of proteins between layers is controlling the nucleation and growth of the inorganic phases in a bio-mineralization process of these structures (Kaplan, 1998; Rousseau et al., 2005; Rousseau et al., 2009). It is well-known that the key toughening mechanism is produced by the sliding of inter-platelets (Rim et al., 2011) and this is due to a precise interfacial design; addressing the problem, several important toughening mechanisms have been put forth by experimental observation.

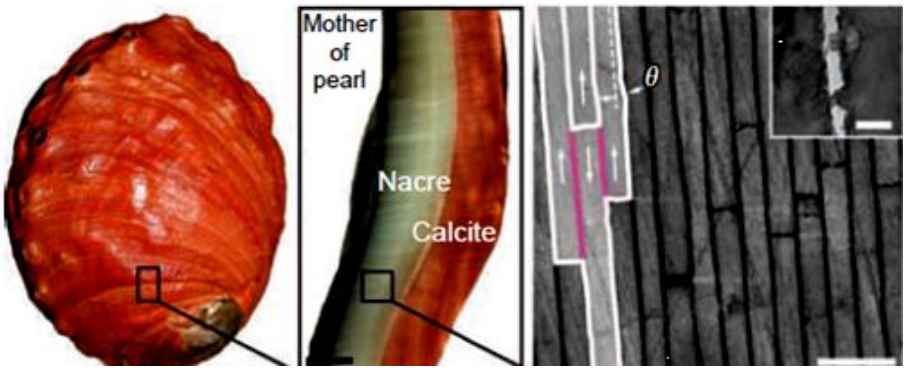

Fig. 1.1 Hierarchical and brick-mortar structure of Abalone nacre (Espinosa et al., 2011).

Interlocking of nano-asperities

The existence of nano-asperities and sliding between them can form multiple dilation bands at the interlamellar boundaries (Fig. 1.2a); on these boundaries, the stress is redistributed and thus, the deformation shows an inelastic behavior (Wang et al., 2001; Li, 2007). Besides, the interfacial sliding produces elastic friction and makes nano-grains (or waviness) on the surfaces of tablets interlock (Barthelat et al., 2007), (Fig. 1.2b), which can induce the anisotropy under loading conditions (Misra and Huang, 2011) and the interlocking effect provides a resistance to the sliding and establishes the level of the stress needed to attain the inelastic strain (i.e. strain hardening), which is considered as a dominated toughening mechanism (Espinosa et al., 2011); the interlocking can realize the overall structural integrity by topologizing the fragmental aragonite platelets (Estrin et al., 2010).

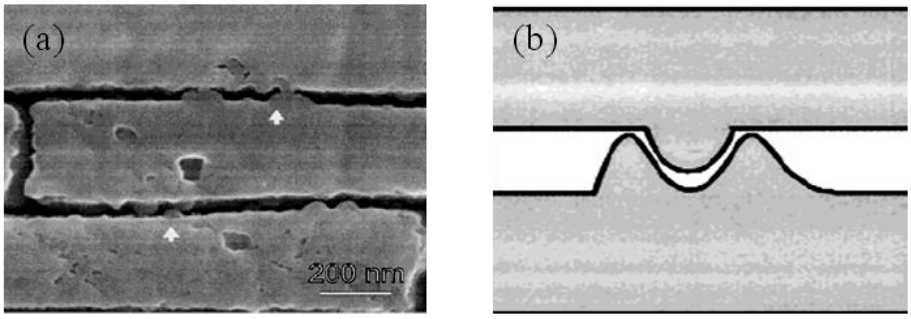

Fig. 1.2 (a) SEM image of nanoasperities on the surface of tablets, (b) Schematic of the interlocking between nanoasperities. (Wang et al., 2001)

Interlamellar mineral bridges

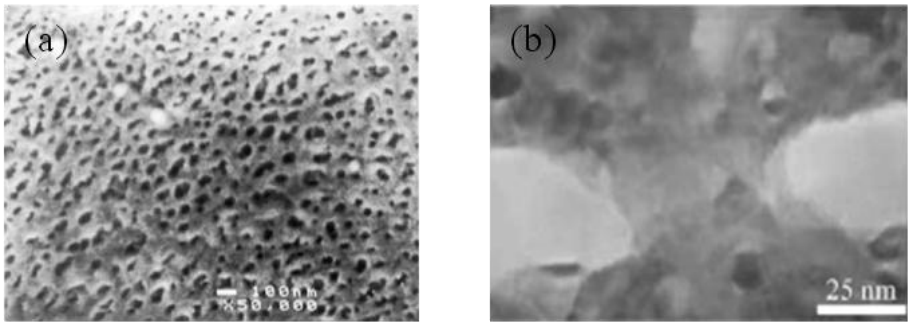

Fig. 1.3 (a) SEM image of interlamellar organic matrix layers with holes (Schäffer et al., 1997); (b) TEM image of mineral bridge between adjacent tablets (Song et al., 2003).

It is observed that there are pores in the sheet of organic matrix layers with 20~30nm thickness (Fig. 1.3a); these pores allow tablets to grow mineral bridges with 5~50nm in diameter (Fig. 1.3b) through them, connecting adjacent aragonite tablets. (Schäffer et al., 1997; Song et al., 2003; Meyers et al., 2008). When external force is imposed, the mineral bridges and organic matrices share the load at the beginning, and the mechanical behavior is approximate linear-elastic; as the force increases, the mineral bridges break; the friction between aragonite platelets emerges to resist the sliding movement; in this phase, the mechanism is similar to the aforementioned one and there is the strain hardening energy.

Weak organic interface

In this mechanism, the organic matrix is considered as an adhesive to glue the

tablelets together (Fig.1.4a). When shells are tensioned, the deformation is mostly caused by the interfacial shear and the high toughness is owed to the unfolded loops/domains of organic proteins (Smith et al., 1999; Fig.1.4b). The weak interfacial design permits stress redistribution around the strain-concentration sites and leads to crack path deflection due to the stress shielding (Clegg et al., 1990; Launey and Ritchie, 2008; Fig. 1.4c). Ritchie (1988) analyzed several toughening mechanisms, and for this phenomenon, the material toughness was expressed as $K_{\mathrm{I}} = K_{\mathrm{tip}} + K_{\mathrm{s}}$, where, K_{I} is the applied stress intensity factor, K_{tip} is the local near-tip stress intensity factor, and K_{s} is the stress intensity factor due to shielding. We can see that increasing K_{s} reduce K_{tip} at constant K_{I} and thus the material toughness is enhanced.

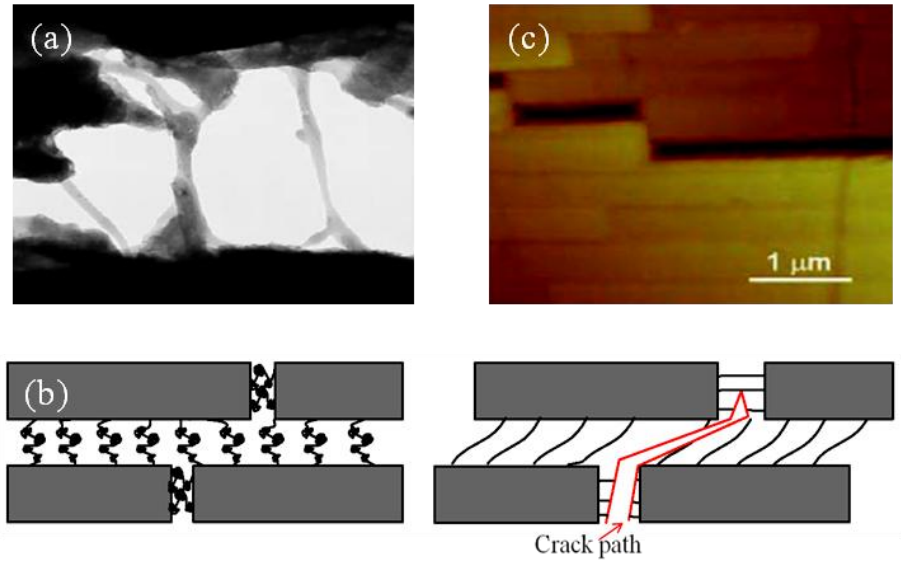

Fig. 1.4 (a) SEM image of adhesive ligaments between platelets (Smith et al., 1999); (b) Schematic sliding between platelets and crack deflection; (c) SEM image of crack deflection (Li, 2007).

Plastic deformation of individual tile

Li et al. (2004) carried out an experiment on a red abalone shell, and the result showed that aragonite platelets were not brittle in nature, but somewhat ductile; the shell deformed plastically accompanied by the sliding movement between aragonite platelets. Besides, the model basing on stiff aragonite platelets was not able to explain the particular mechanical behavior, which occurred under dynamic solicitations

(Stempflé and Pantalé, 2007); there authors found that the plasticity of individual platelet was due to the intracrystalline matrix (Fig. 1.5b), the elastic properties of which was two times lower than those of the intercrystalline one; they concluded that the intracrystalline matrix govern the plastic deformation of the single platelet and therefore the overall deformation of the nacre (Stempflé et al., 2010). Also, the fracture of individual platelet was investigated by Lin and Meyers (2009).

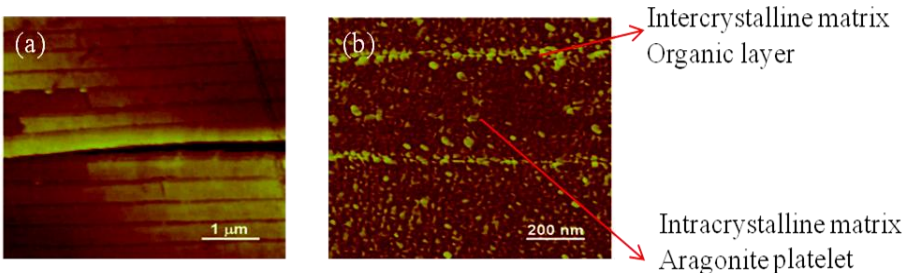

Fig. 1.5 (a) Cross-section of nacre; (b) Intercrystallinne matrix and intracrystalline matrix (Li et al., 2004).

Multiple cracking and large-scale crack bridging

As we know, high toughness usually is achieved during crack propagation (R-curve behavior), and materials can absorb more fracture energy (Lanuey and Ritchie, 2008). *Strombus gigas* conch shell has a spiral configuration and a lower strength compared with that of abalone nacre, due to their different microstructures (Lin et al., 2006); two energy-dissipating mechanisms are invoked, i.e. multiple microcracking in the outer layer at low loading levels and crack bridging in the middle layer at high loading levels (Kamat et al., 2000; Fig. 1.6). Under low loads, the external work is absorbed by the propagation of the microcracks at the outer layer, while the middle layer prevents the crack propagation (intrinsic toughening mechanism); as the loads increases, the energy absorption saturates in the outer layer and the cracks reach the middle layer and grow while the crack bridging developed in the outer layer restrains the crack growth in the middle layer (extrinsic toughening mechanism). The interacting process leads to the high toughness. Of course, the organic phase also plays an important role in the process (Kamat et al., 2004).

Structural models

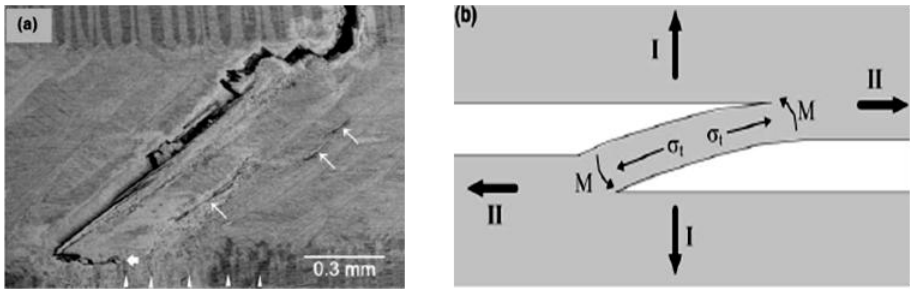

Fig. 1.6 (a) Ligament bridging a delamination between the middle and outer layers of the shell (Kamat et al., 2004); (b) Model for crack bridging by misaligned fibers (Cox and Marshsall, 1994).

Basing on the aforementioned mechanisms, some models and principles were extracted to build the structure-function relationship for future bio-inspired material design. A simple physical model of nacre (platelet-reinforced composites) was built by Jackson et al. (1989); the Young's modulus was predicted by the rule of mixture, incorporating shear-lag models, and the tensile strength determined by the interfacial shear was predicted by pull-out failure mode; the two predictions agreed with the experimental data very well, however, the model failed to mimic the fracture toughness. Lin et al. (2006) employed the classical Weibull statistic strength theory to compare the mechanical strengths of *Strombus Giga*, *Tridacna Gigas*, and *Haliotis Rufescens* seashells, and found $\sigma_{Tridacna} < \sigma_{strombus} < \sigma_{Haliotis}$. Tang et al. (2007) proposed an elasto-viscoplastic interface model with a constitutive relationship to understand the strengthening mechanism, and the numerical simulations showed a hardening deformation, which was consistent with the previous experimental results. Ji (2008) incorporated the tension-shear chain (Jäger and Fratzl, 2000; Ji and Gao, 2004, Fig. 1.7a) into the Dugdale model (Dugdale, 1960) to investigate the hybrid interfacial strength and estimate the fracture energy. Basing on the same arrangement, i.e. tension-shear chain, (Fig. 1.7b) and homogenization theory, Bertoldi et al. (2008) proposed a micromechanical model to study the macro-mechanical behavior of nacre, and the analytical results showed that Nacre was orthotropic and had different Young's modulus when compressed and tensioned, consistent with existing experimental and numerical data. Recently, Rim et al. (2011) have developed a composite-computational

model to investigate the influences of geometrical parameters and intrinsic material properties of constituents, incorporating the key morphological features; the results showed that the optimal geometry could increase the toughness by 70 times.

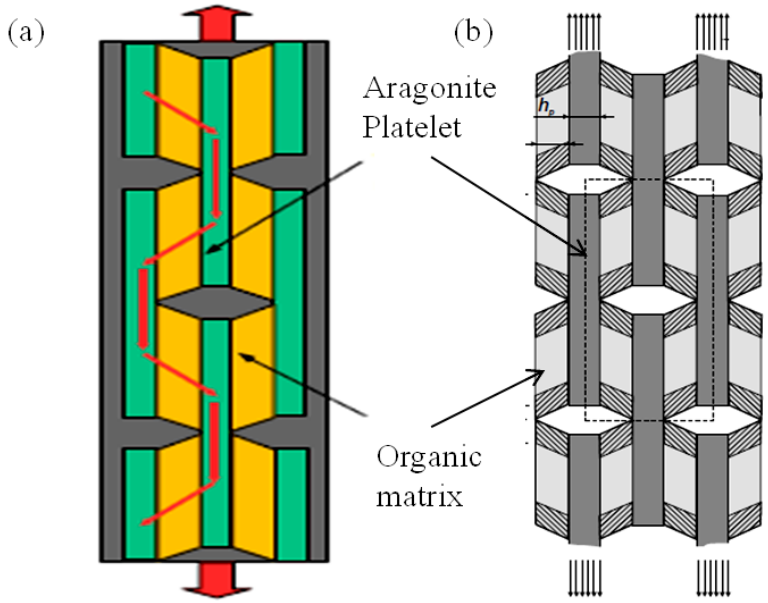

Fig. 1.7 Tension-shear chain model (Ji and Gao, 2004; Ji, 2008; Bertoldi et al., 2008)

1.3 Gecko feet

Gecko feet attract people's attention for a long time, because of the capacity running on a vertical wall freely. It is observed that a gecko foot is a typical hierarchical structure (Fig. 1.8) and it contains about 0.5 million setae (Autumn et al., 2000); the seta distribution density is 5000 setae/mm^2. One gecko foot can produce 10N adhesive force, which is much larger than gecko's body-weight, and thus, each seta carries 20 μN. This is why the gecko can stay on the vertical wall without slipping and explains the great adhesive ability. However, because geckos need to move fast on the wall when preying or escaping, also, they must detach easily from the attaching state. Therefore, in order to design gecko-pad-inspired materials, the attaching and detaching phenomena have driven many scientists to reveal the mechanism.

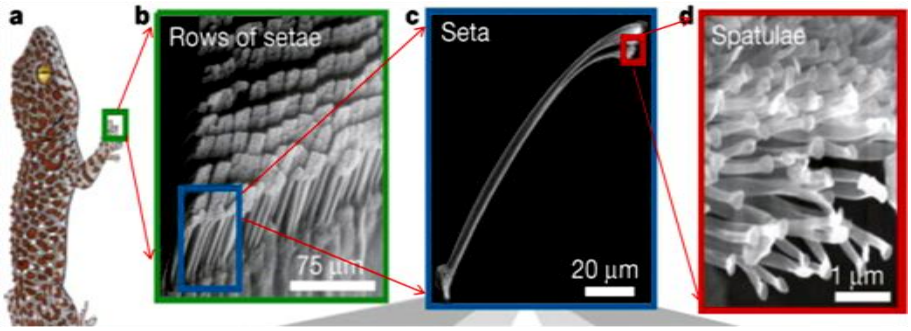

Fig. 1.8 Hierarchical structure of a gecko foot. (a) Gecko; (b) Seta row; (c) Single seta; (d) Spatulae (Autumn et al. 2000).

Attaching mechanisms

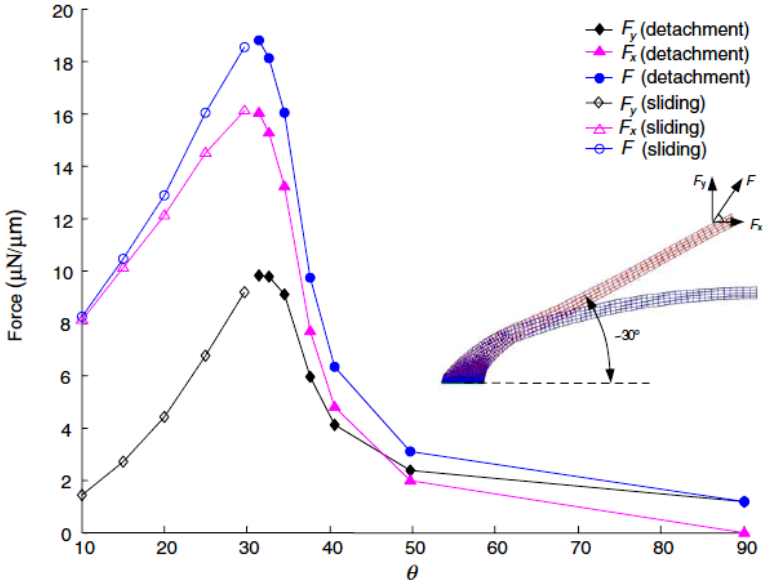

Fig. 1.9 Analysis of the pull-off force of a single seta as a function of the pulling orientation (Yao and Gao, 2006)

In the dry environment, employed a two-dimensional micro-electro-mechanical systems force sensor, a single setal force was measured directly by Autumn et al. (2000, 2002); the results denied the suction and friction mechanisms but supported the evidence that the intermolecular force—van der Waals force—played vital role in the single seta attachment. Meanwhile, a large difference between the adhesive force of the

single seta and that of measured in the whole gecko under a small normal preload was discovered; addressing this, later, Autumn and Peattie (2002) proposed an approach that integrates levels from molecules to gecko. Not strongly influenced by the surface chemistry, the intermolecular force was emphasized to be only influenced by the shape and size of the setal tip. Autumn and Peattie (2002) pointed out that the orientation of the setae was important in the detaching process and the detachment happened when the angle made by the setal axes and substrate exceeded 30^{o}, which was also numerically observed by Yao and Gao (2006; Fig.1.9).

In the wet environment, Huber et al. (2005) found an evidence of capillarity contributions by a nano-mechanical measurement on a single spatula, which is at the lowest level of the gecko-foot hierarchical structure. The different finding, from that provided by Autumn, is the influence on adhesion of humidity present between the spatula and substrate; recently, Prowse et al. (2011) reported that increasing humidity improved the adhesion and friction force and produced a significant influence on the mechanical properties (elasticity, strength, fracture and dynamics) of setae and setal lamina (Fig. 1.10).

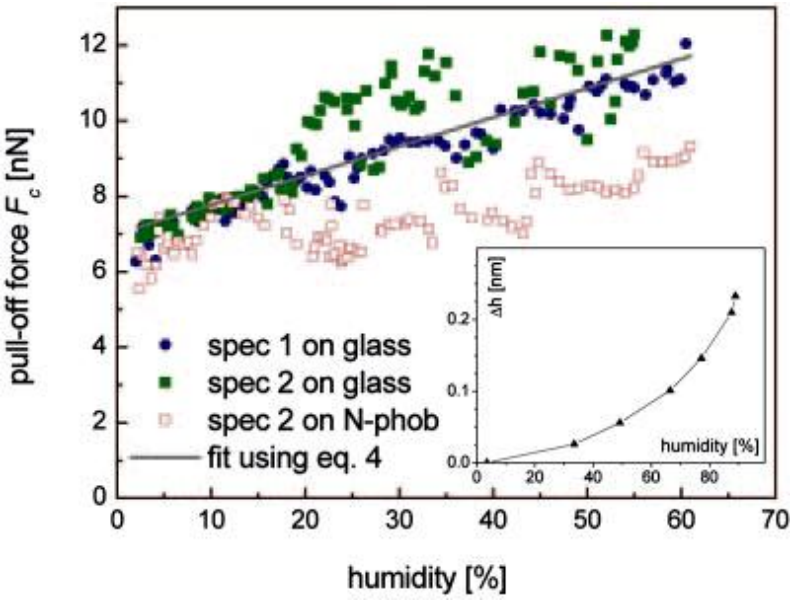

Fig. 1.10 Spatular pull-off forces on glass and N-phob vs. humidity at ambient temperature (Prowse et al., 2011).

Detaching mechanisms

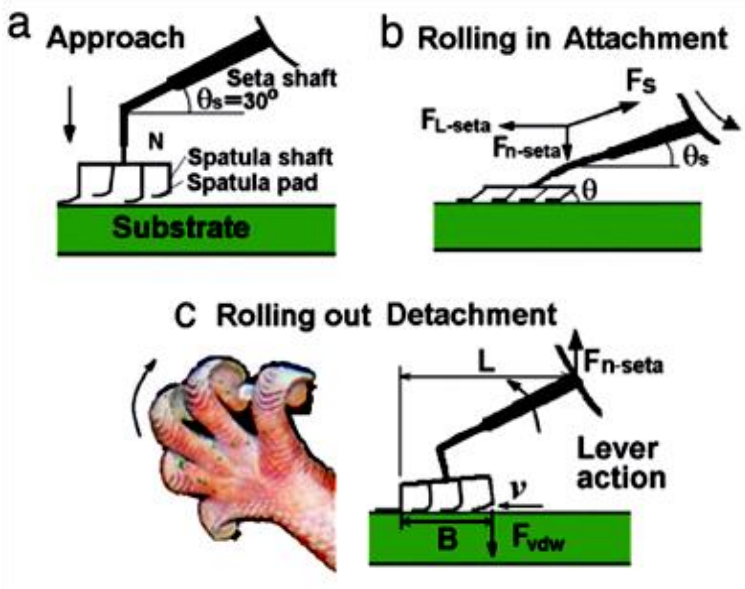

Fig. 1.11 Schematic of mechanisms of attachment and detachment. (a) A single seta, (b) Rolling down for attachment, (c) Rolling up for detachment (Tian et al. 2006).

Regarding the detaching mechanisms, they are well-known also at the micro-scale: the seta detaches when the shaft reaches a critical angle with the substrate; at the macro-scale, geckos hyperextend their toes. Peeling is the governing mechanism at all the different hierarchical level (Pugno, 2008; Varenberg et al., 2010; Pantano, et al., 2011). However, because the contact angle raises a question when gecko is inverted on the ceiling, Autumn et al. (2006) considered another adhesive mechanism—frictional based—and demonstrated that adhesion depends directly on shear force. Addressing the adhesion and friction contributions, Tian et al. (2006) theoretically analyzed the interaction between the spatula and substrate basing on a tape model; rolling down and gripping toes inward produced a small contact angle and made gecko able to obtain a strong attachment; by contrast, rolling toes up and back produced a low adhesion-to-friction ratio helping the perpendicular peeling off of the spatula off from the substrate (Fig. 1.11).

Optimization problems

Gao and colleagues (Gao et al., 2004) applied the principle of flaw tolerance (Gao et al., 2003) to the nanostructures of biological systems; they showed that spatula

geometry, the finest structure in the structure of gecko foot, has an influence in determining the adhesion strength (Fig. 1.12). Gao and Yao (2004) investigated the shape influence of the tip in fibrillar structures on the adhesive optimization; the result displayed that when the size of the diameter reduced to 100nm the variation in shape produces weaker influences. The flaw tolerant hypothesis was fully verified by an atomistic and continuum study at small scales (Buehler et al., 2006). These authors studied the adhesive properties with a hierarchical approach (Chen et al., 2008; Yao and Gao, 2006) and showed that the size of each hierarchical level is optimized as well.

Persson (2003) and Persson and Gorb (2003) studied the mechanism of the adhesion in biological system (e.g. gecko and fly) and developed a set of theory. They discovered that the small effective elastic modulus of the setae array was a basic influence on the adhesion on a hard but rough surface, and reported that the setae array had a large contact angle and exhibited a self-cleaning function; the self-cleaning was first analyzed, with water contact angle, by Autumn and Peattie (2002) and later verified by Hansen and Autumn (2005). Other authors (Pugno and Lepore, 2008a, 2008b; Lepore et al., 2008) investigated the adhesive time of male and female geckos on different rough surfaces and found that the time to failure obeys a Weibull statistical distribution. Autumn et al. (2006) studied the dynamics of geckos running on a vertical wall and found that different leg had different functions, to make gecko move faster.

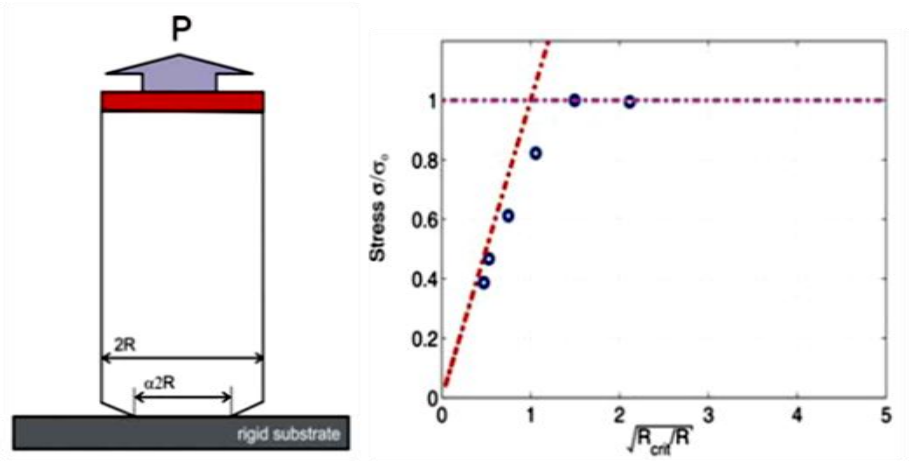

(a) (b)

Fig. 1.12 Flaw tolerant adhesion: (a) Schematic of the spatula; (b) Atomistic simulation results (Gao et al., 2004).

1.4 Spider silk

Spider silks have different functions, such as protective housing and traps (Foelix, 1996). However, the most interesting webs are adapted to capture high velocity insect in their middle-flight (Vollrath, 2000) and have a high damping capacity which is considered as a result of evolution and can dissipate kinetic energy caused by larger, energetically valuable preys (Kelly et al., 2011). In particular, the orb-weaving web are widely studied, and it is constructed by web frame and dragline, excreted by the major ampullate (MA) gland, and viscid silk, produced by the flagelliform (FL) gland, which have different properties (Fig.13; Gosline et al., 1999). Fig.13 shows that the dragline silk or web frame is stiffer, but viscid silk is tougher. This is probably because the grade of mechanical properties is more suitable for absorbing the impact energy caused by preys.

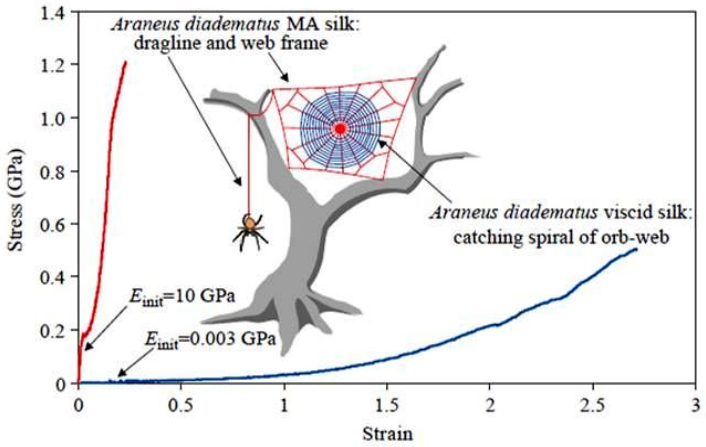

Fig. 1.13 Stress-strain relationships of two types of silks in orb-weaving spider web (Gosline et al., 1999)

Structure property

It is widely recognized that spider silk is a hierarchical structure, starting from nanostructures to macrostructure, and consists of the amorphous network chains and β-sheet crystals constructed by poly-(Gly-Ala) and poly-Ala domains (Ackbarow et al., 2007; Keten et al., 2010). Some of previous works (Ichimura and James, 1994; Colgin

and Lewis, 1998; Hayashi and Lewis, 1998) dedicated to reveal the genetic information on the amino acid sequence motifs present in spider fibroin. Basing on these works, Gosline et al. (1999) reported the molecular structure of spider silk, and analyzed the mechanical properties. And basing on scanning electron microscope and atomic force microscope images, Du et al., (2006) reported a new hierarchical model of spider silk (Fig.14). Recently, as the development of molecular dynamics simulations, Buehler and his colleague (Ackbarow et al., 2007; Buehler and Ackarow, 2008; Keten et al., 2010; Nova et al., 2010; Bosia et al., 2010; Giesa et al., 2011) made a huge amount of theoretical and numerical studies to reveal the influence of hierarchical structures on protein mechanical properties. They believed that the hierarchical architecture and seamless integration of material and structure, from nano to macro, plays an important role in the structure–property relationship of spider silk.

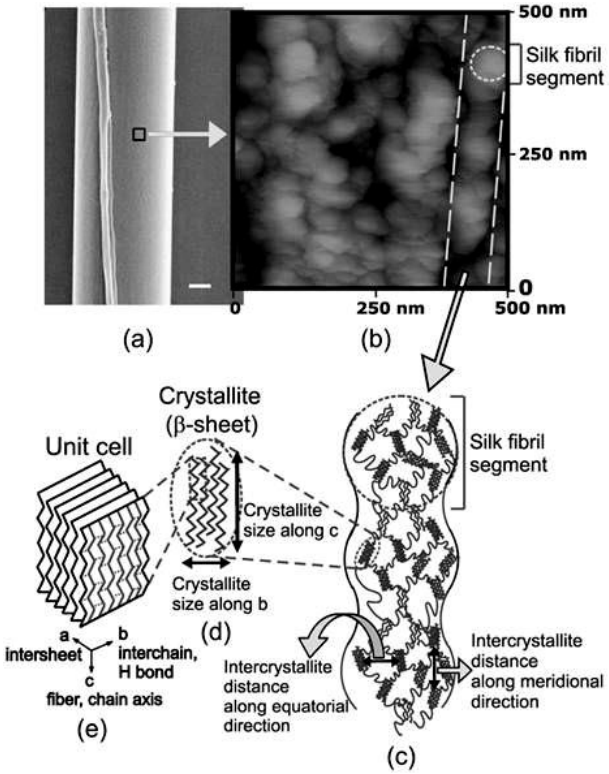

Fig. 1.14 Hierarchical structure of spider silk. (a) SEM image of spider dragline silk; (b) AFM image of silk fibril structure; (c) schematic of silk fibril structure; (d) schematic of crystallite; (e) Unit cell of silk crystallite (Du et al., 2006).

In general, due to their high strength, toughness, extensionality and torsional qualities that stop the spider twisting and swinging (Emile et al., 2006), it gains much attention from scientists and engineers, and understanding the mechanism or structure-property relationships can inspire scientists and engineers to fabricate new materials for different applications, e.g., in the fields of tissue engineering.

Toughening mechanisms

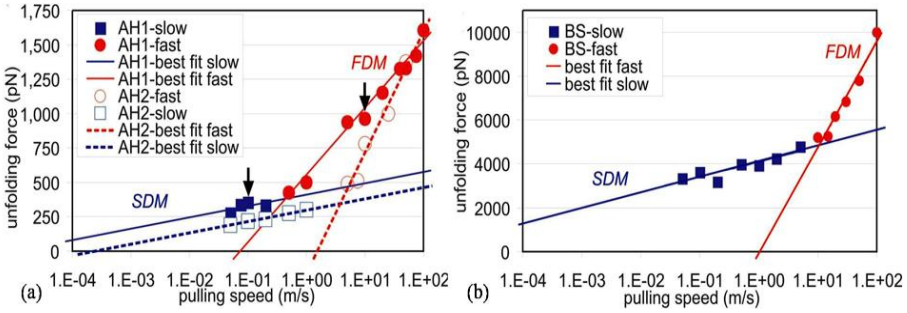

Fig. 1.15 (a) Unfolding force of α-helical domains (IHBs) *vs.* varying pulling speed; (b) unfolding force of β-sheet domains (SHBs)*vs.* varying pulling speed (Ackbarow et al., 2007).

The excellent mechanical properties of spider silk are owing to the interaction between different hierarchical levels. In terms of chemical composition and morphological structure, Porter et al. (2005) assumed stiffness and strength, on the one hand, are due to the high cohesive energy density of hydrogen bonding, and toughness, on the other hand, is due to the high energy absorption during post-yield deformation and employed mean field theory to study structure-property relations of spider silk. At nanoscale (hydrogen-bond level), Ackbarow et al. (2007) proposed two fracture mechanisms of biological protein materials by through atomistic simulations (Fig.15), i.e., the unfolding mechanism at fast pulling rates is sequential rupture of individual hydrogen bonds (IHBs) (Fig.15a) and unfolding at slow pulling rates proceeds by simultaneous rupture of several HBs (SHBs) (Fig.15b), which is a typical structure of the lowest level (Fig.14e). As for the influence of proline, the thermo-elastic measurements (Savage and Gosline, 2008) were employed to study it in the elastic mechanism of hydrated, spider silks and different structural organization in glycine-rich network chains and the mechanism of elasticity in proline-rich, and proline-deficient fibroins resulted in different mechanical properties. Finally, addressing the strain-hardening behavior of spider silk different from the silkworm silk,

the reason was attributed to the unfolding of the intra-molecular β-sheets in spider silk fibrils (Fig.16; Du et al., 2011), which is similar as the unfolded loops/domains of organic proteins between platelets in nacre (Smith et al., 1999). The mechanism is that protein backbones and nodes of the molecular network are stretched to support the load as the progressive unfolding and alignment of protein during fiber extension. The process was described by Euler (2008) as entropy springs, which play an important role in soft matter and underlie the intriguing mechanical properties of spider silk.

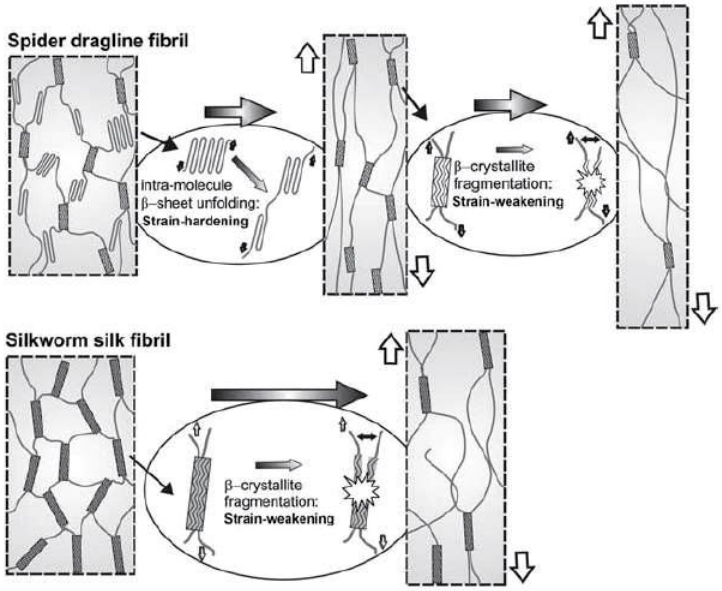

Fig. 1.16 A schematic model demonstrating stretching difference between silkworm and spider dragline fibers (Du et al., 2011).

As for the influence of crystal regions (Huemmerich et al., 2004), Du et al. (2006) reported that high strength of the spider dragline silk could be obtained by decreasing the size of the crystalline nodes in the polypeptide chain network while increasing the degree of orientation of the crystalline nodes. Keten et al. (2010) revealed that the strength of spider silk arises from β-sheet nanocrystals, this is counterintuitive due to the weak hydrogen bond, but they owed this result to nanoconfinement, and flaw tolerance (Qin and Buehler, 2011), which improved the strength, toughness and stiffness. Also, Cetinkaya et al. (2011) used a bottom-up approach and combined molecular dynamics and finite element analysis to analyze the effect of crystalline subunit size on the silk mechanics, and they reported that the silk Young's modulus

and toughness increased with the crystal length but decreased with the crystal cross-section area. In particular, they included both the crystalline and amorphous subunits, and concluded that the friction between entangled chains causing higher stiffness and energy absorbance, which homogenized the stress distribution.

Theoretically, Zhou and Zhang (2005) developed a hierarchical chain model (Fig.17a) with different motifs at different levels to investigate spider silk strength and elasticity according to (Fig.17b; Becker et al., 2003), and in this model, two element were considered the red part denoted crystallite and the lines bonds or amorphous bioploymers; the model obtained supports from the amino-acid sequence of the major flagelliform protein of spider capture silk. Ackbarow et al. (2007) employed the hierarchical Bell model to express a rigorous structure–property relationship from the point of statistical mechanics. Bosia et al. (2010) adopted a fiber bundle model approach with a hierarchical multiscale self-similar procedure to consider the hierarchical topology of natural materials; to some extent, they explained the energy dissipation mechanisms.

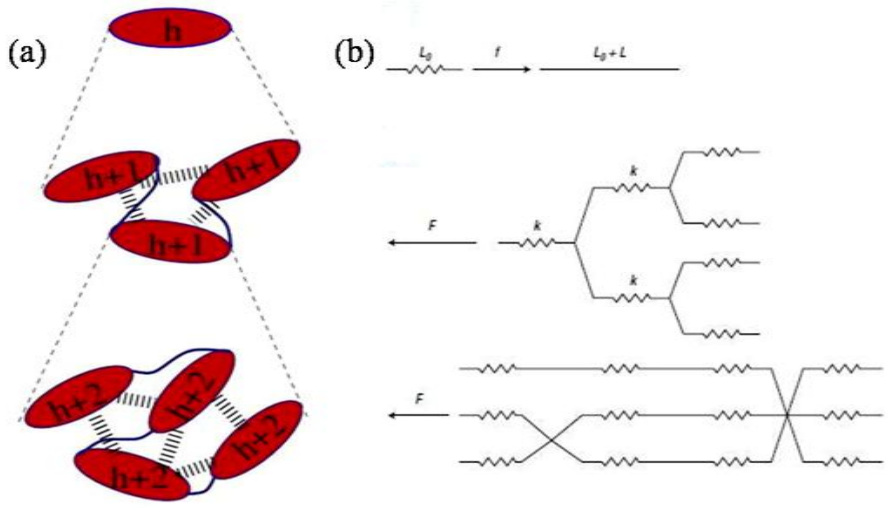

Fig. 1.17 (a) Hierarchical chain model, the broken line denotes sacrificial bonds and solids surviving bonds (Zhou and Zhang, 2005); (b) schematic of a network of identical springs in spider silk (Becker et al., 2003).

Other mechanisms

Besides, there are some other conditions influencing the mechanical properties of spider silk, such as spinning conditions, humidity and temperature etc. As for the

spinning conditions, Pérez-Rigueiro et al. (2005) developed a force silking procedure, which can measure the low force involved in the silking process and found that fibres spun at high silking force were stiff and fibres spun at low and very low silking forces were more compliant (Vollrath et al., 2001), of which tensile behavior corresponded to that of fibres naturally spun by the spider. And Liu et al. (2005) got the same result (Fig.18a); in the meanwhile, Vollrath et al. (2001) also reported that the high temperature could result in stiffer silk product than low temperature (Fig.18b). Agnarsson et al. (2009) performed two types of tests to examine the influence of water on the mechanical properties of spider silk, which is so-called "supercontraction" (Work, 1977), and they found that the cyclic humidity caused the cyclic stress response (Fig.18c), which induced the contract and relax on drying and wetting environment, respectively. From the point of the evolution, Boutry and Blackledge (2010) explained the mechanism of supercontraction in spider silk, which was induced by a rearrangement of GPGXX motifs, and found the structure–function relationship to tailor the silk properties. Finally, Venner and Casas (2005) explored the relationship between the size of prey and the spider web and reported that spiders cannot survive or produce eggs without catching these large but rare preys and increasing web size increases the daily number of prey caught and thus long-term survival and fecundity.

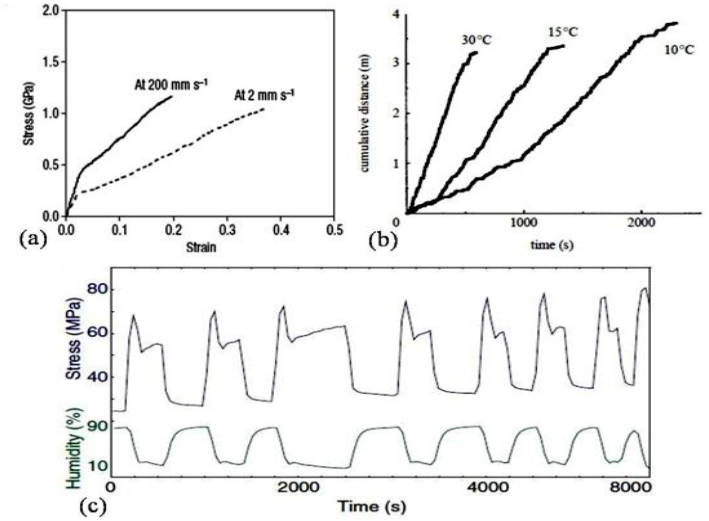

Fig.18 (a) Silk spun at 2 mm/s vs. that at 200 mm/s (Liu et al., 2005); (b) the influence of temperature on web-building speed (Vollrath et al., 2001); (c) dragline silk repeatedly contracts and relax with humidity (Agnarsson et al., 2009).

1.5 Exoskeletons of Lobsters/crabs

Structural property

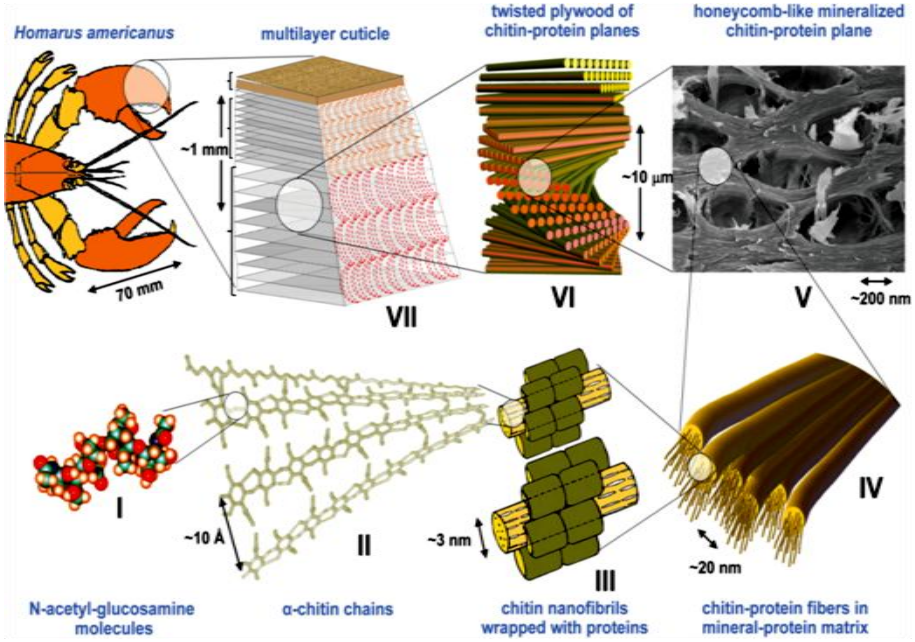

Fig. 1.19 Hierarchical structure of the lobster cuticle (Nikolov et al., 2010).

Lobster or crab cuticle (Fig. 19) is another widely-studied natural material with high mineralization, which is divided into three layers, i.e., epicuticle, exocuticle and endocuticle (Fig. 1.19Ⅶ). These layers, from exterior to interior, have decreasing densities (Raabe et al., 2005). Fabritius et al. (2009) reviewed the progress in the study of lobster and systematically elaborated the structural and mechanical properties of the biological composites, and made an outlook for future study.

Firstly, the twisted plywood or Bouligand structure (Fig. 1.19Ⅵ), which is frequently encountered in Nature, especially in the skeletal and protective mineral tissue (e.g. compact bone), is the prominent building principle to develop the mechanical behaviors of the biocomposite (Fabritius et al., 2009). Secondly, the honeycomb structure (Fig. 1.19Ⅴ), which was formed by the interconnected fibers bend around the pore canals and discovered by Raabe et al. (2005), is another

important and effective building principle. Besides, Raabe et al. (2006, 2007) studied perferred crystallographic texture of the α-chitin–protein network in the exoskeleton of the lobster and elucidated crystallographic building principles in crystalline organic tissue; at the end, they made a conclusion that complex hierarchical structure could be simply described by crystallographic textures.

Mechanical property

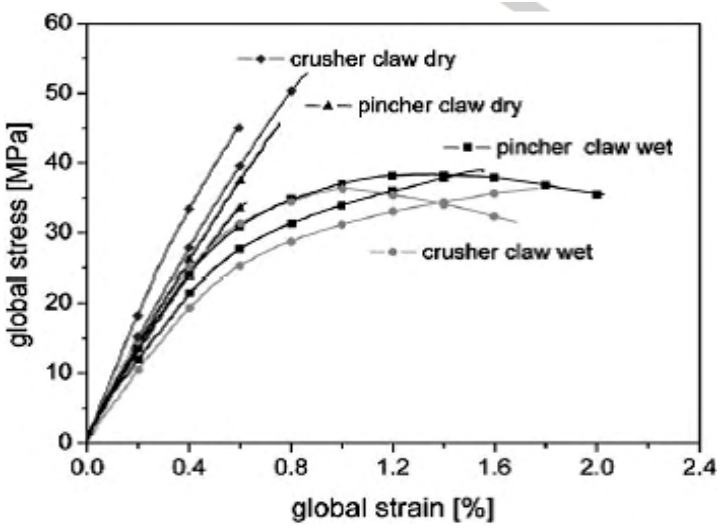

Fig. 1.20 Global stress-strain relationship of the endocuticle from the pincher and crusher claws both in dry and wet state under tensile loading (Sachs et al., 2006).

As mentioned before, Raabe et al. (2005) studied the mechanical and structural gradients of the exoskeleton by experiments on stiffness and hardness, and they found that, from out layer to inner layer, the stiffness decreased from 9GPa to 4GPa or so and hardness from 130MPa-270MPa to 50MPa; they also pointed out that there is an important influence of the interfaces between layers on the overall mechanical behavior. Employing nanoindentation Sachs et al. (2006) and Romano et al. (2007) also revealed gradient and anisotropy in the hardness of such dehydrated materials; in order to fully understand the mechanical properties of the natural material, Sachs et al. (2006) continued to perform a tensile experiment on both dry and wet samples to examine elastic-plastic deformation behavior of the lobster cuticle, combining with a detailed global and local strain analysis (Fig. 1.20); they found that the heterogeneity by local strain analysis and the existence of water both enhances the plastic deformation ability.

In addition, Sachs et al. (2008) illustrated the influence of microstructures on deformation anisotropy of the exoskeleton under different loading directions, e.g. in the normal direction (out-of-plane) to the cuticle and in the transverse direction (in-plane) (Fig. 1.21); Fig. 1.21 shows that the mechanical behaviors in the two directions are similar to the out-plane and in-plane behaviors of conventional honeycombs (Papka and Kyriakides, 1994, 1998a, 1998b).

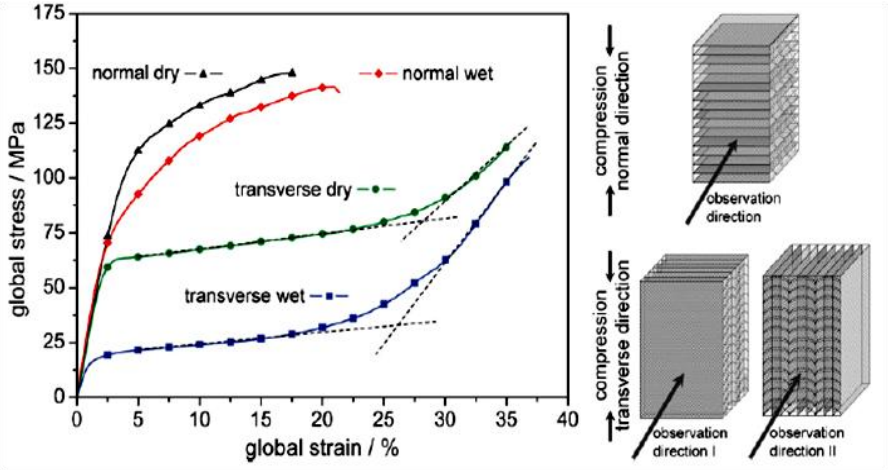

Fig. 1.21 Global stress-strain relationship of the endocuticle and schematic figure of the compression tests (Fabritius et al., 2009).

In particular, incorporating quantum mechanics and density functional theory, Nikolov et al. (2010) recently proposed a method to investigate structure–property relations of the lobster at all length scale and developed a hierarchical model: it included *ab initio* calculations at the nanometer scale and mean-field homogenization for higher hierarchy levels, proper linked. By a bottom up approach, Tang et al. (2009) and Chen and Pugno (2011a, 2011b) derived the mechanical properties at a given hierarchical level starting from those of the previous level; thus the properties at all length scales are obtained.

1.6 Armadillo Shell

Armadillo (Fig. 1.22), as a natural carrier of the leprosy bacillus, has been studied extensively and deeply for the immunology, chemotherapy, and epidemiology of the

disease (Truman et al., 1991; Truman, 2008). The armadillo's shell as also an ideal armor structure, recently attracts attention from material researchers.

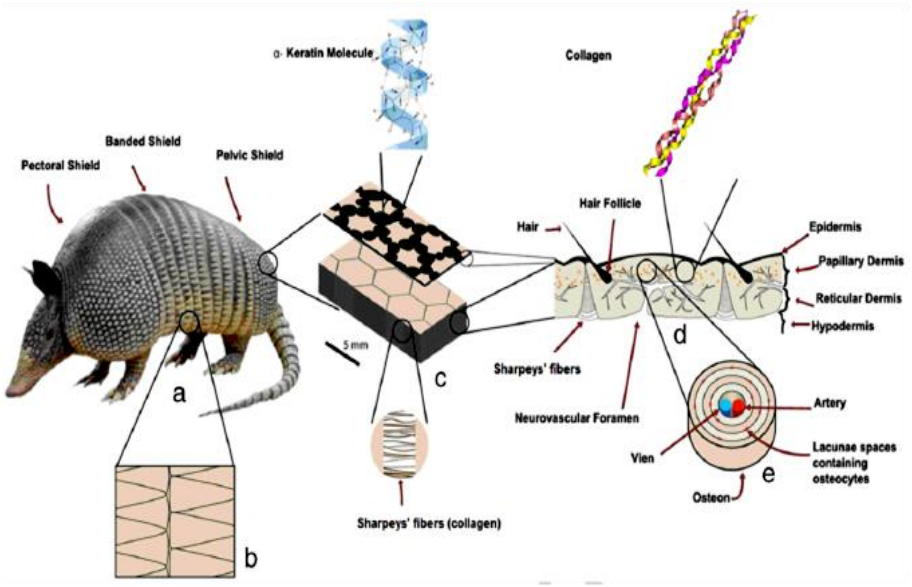

Fig. 1.22 Hierarchical structure of the nine-banded armadillo's dermal shells. (a) Armodillo; (b) Triangle scales of band shell; (c) Hexagonal scales of rear shell; (d) Cross-sectional view of rear shell (Chen et al., 2011).

Composition

From the appearance, the armor shell (or osteoderm) is divided into three types, i.e., forward shell (pectoral shield), band shell (banded shield), and rear shell (pelvic shield), Fig. 1.22, which are formed by a number of overlapped scales with different shapes (triangle in the band and hexagonal in forward and rear shells). Rhee et al. (2011) analyzed their chemical components using X-ray spectroscopy technique, finding significant amount of calcium (Ca), phosphorous (P), sodium (Na), and magnesium (Mg) in the mineral constituent and the elements of carbon (C), oxygen (O), sulfur (S) in β-keratin and collagen. For the hexagonal scales, basing on drying and ashing experiments, Chen et al. (2011) found they contain 13.6±0.4 (wt%) water and 64.8±1.3 (wt%) mineral, and the remaining part is mainly composed by collagen and keratin.

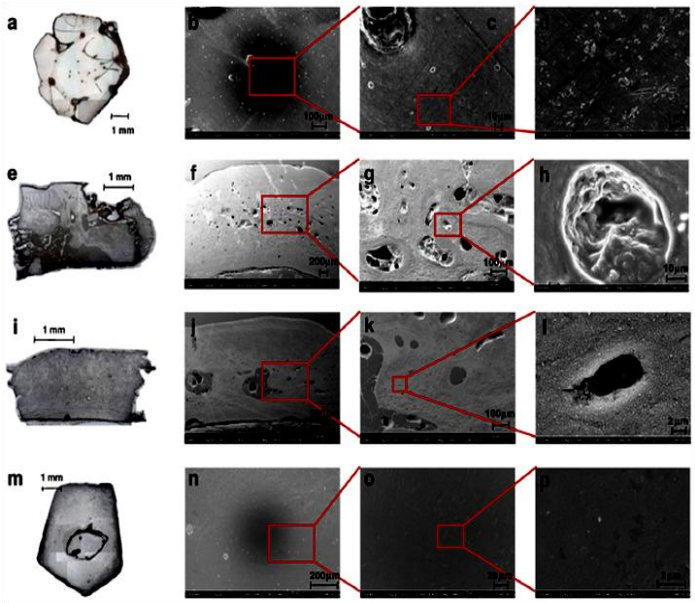

Fig. 1.23 SEM images of the hierarchical structure of the forward shell: (a-d) top view; (e-h) front view; (i-l) side view; (m-p) bottom view (Rhee et al., 2011).

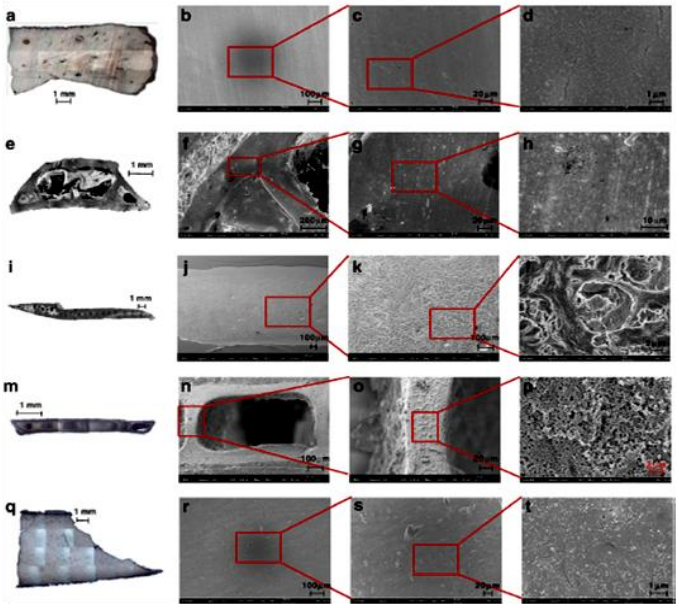

Fig. 1.24 SEM images of the hierarchical structure of the band shell: (a-d) top view; (e-h) front view; (i-l) side view; (m-p) back view; (q-f) bottom view (Rhee et al., 2011).

Structural property

Addressing the microstructures of the three mentioned parts, Rhee et al. (2011) employed Scanning Electronic Microscope (SEM) to fully characterize them. The forward and rear shells (Fig. 1.23) share a common structural property, and both are sandwich composite structures; they contain a hard and dense exterior layer and a porous interior layer, which is similar to the structure of bone (Vickaryous and Hall, 2006) and turtle shell (Rhee et al., 2009). As for the band shell, it is more complicated and sophisticated (Fig. 1.24); each band is overlapped at the rear part of the anterior one and is thicker than that of the rear part (Fig. 1.24(i-l)); the structure of the thick forward part of each band is similar to those of the forward and rear shells but with a larger pores (Fig. 1.24(e-h)), while the structure of the thin rear part of each band shows a regular single-layer wood-cell-like structure (Fig. 1.24 (e-h)). Besides, the collagen (Sharpey's fibers) connects scales together, and enhances the armor flexibility by collageneous retraction to make the body bend (Fig. 1.25). This is different from that of nacre, in which the organic layer is mainly between calcium carbonate platelets, and the nacre has a weaker flexibility but with stronger in-plane strength and toughness. The difference depends on their functions of the tissues.

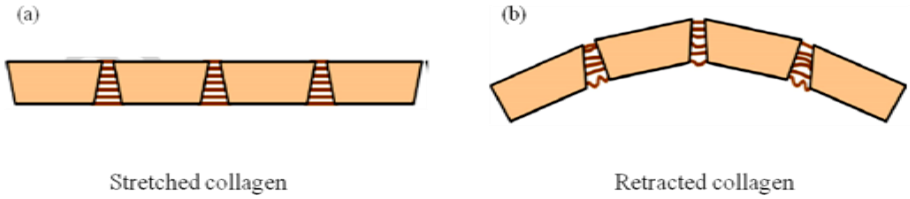

Fig. 1.25 Schematic of connection between tiles and collagen fiber (Chen et al., 2011).

Rhee et al. (2011) employed Vickers hardness tester to test related tissue hardness, and Instron electromechanical test apparatus to test their strength. They found that the bottom and top surface were harder (~53 Hv) than the front and side surfaces (~45 Hv), which meant denser surfaces; they also found that the strength of the forward shell (~1.5 GPa) was three times than that of the band shell (0.5 GPa), and the former mechanical behavior was akin to that of the foam materials (Gibson and Ashby, 1997); this is probably due to the inelastic deformation mechanism of microbuckling while the intrinsic material behavior was approximately linear elastic. Chen et al. (2011) performed experiments on both dry and wet shell samples without considering which part the samples were from; they found that Young's moduli of the dry samples (~425

MPa) were almost three times than those of the wet samples (~150 MPa), tensile strength of the dry samples (~23 MPa) two times than those of the wet samples (~13 MPa), and toughness of the dry samples (~1.1 MJ/m^3) two times than those of the wet samples (~0.53 MJ/m^3).

1.7 Turtle shell

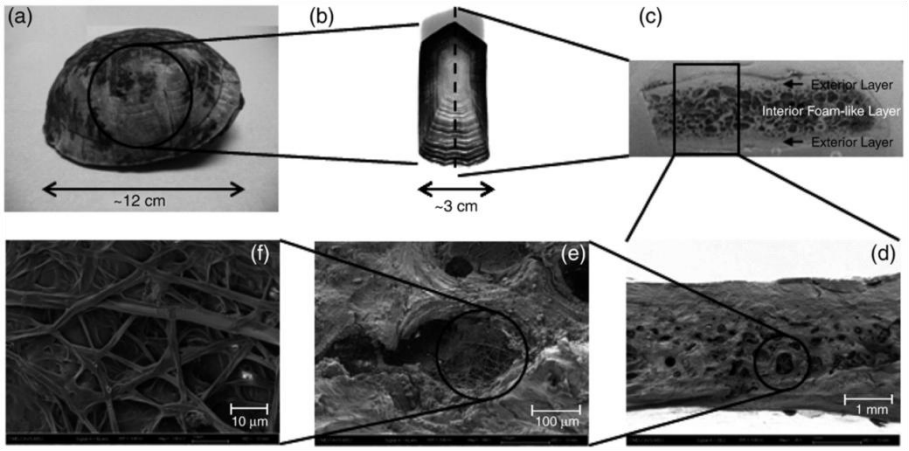

Fig. 1.26 Hierarchical structure of carapace shell: (a) the turtle carapace shell; (b) a costal scale; (c) form-like cross-sectional view; (d) a SEM image of cells; (e) a magnified SEM image of cells; (f) fibrous structure inside a cell (Rhee et al., 2009).

Turtle is one of the eldest vertebrates and is believed to have existed for 200 million years. Its shell, composed of a dorsal shell (carapace, usually a strong and rigid structure; Fig. 1.26) and a ventral shell (plastron), represents an evolutionary novelty (Gilbert et al., 2001; Krauss et al., 2009); it plays a significant role in physical protection and reserving water, fat, or wastes. Therefore, many works investigated the evolutionary and morphogenesis of its box-shell structure, from carapacial ridge-specific gene to embryonic development of the shell and biologists try to uncover how turtle forms its shell (Kuraku et al., 2005; Rieppel, 2009). However, as for the armadillo shell, about the microstructure-mechanical relationship has not been studied extensively, and so we here review pioneering works, only recently developed, on the shell microstructure and its mechanical properties.

Composition

Rhee et al. (2009), using an energy dispersive X-ray (EDX) technique, analyzed the outermost keratin layer of the carapace shell and found the basic elements of carbon (C), oxygen (O), nitrogen (N), sulfur (S), which are main constituents of proteineous materials; while, in the layer right underneath the outmost keratin layer and the inside surface of the carapace shell, they found abundant mineral elements, such as calcium (Ca, 15–20 wt.%), phosphorous (P, 7–10 wt.%), sodium (Na), chlorine (Cl), and magnesium (Mg).

Structural property

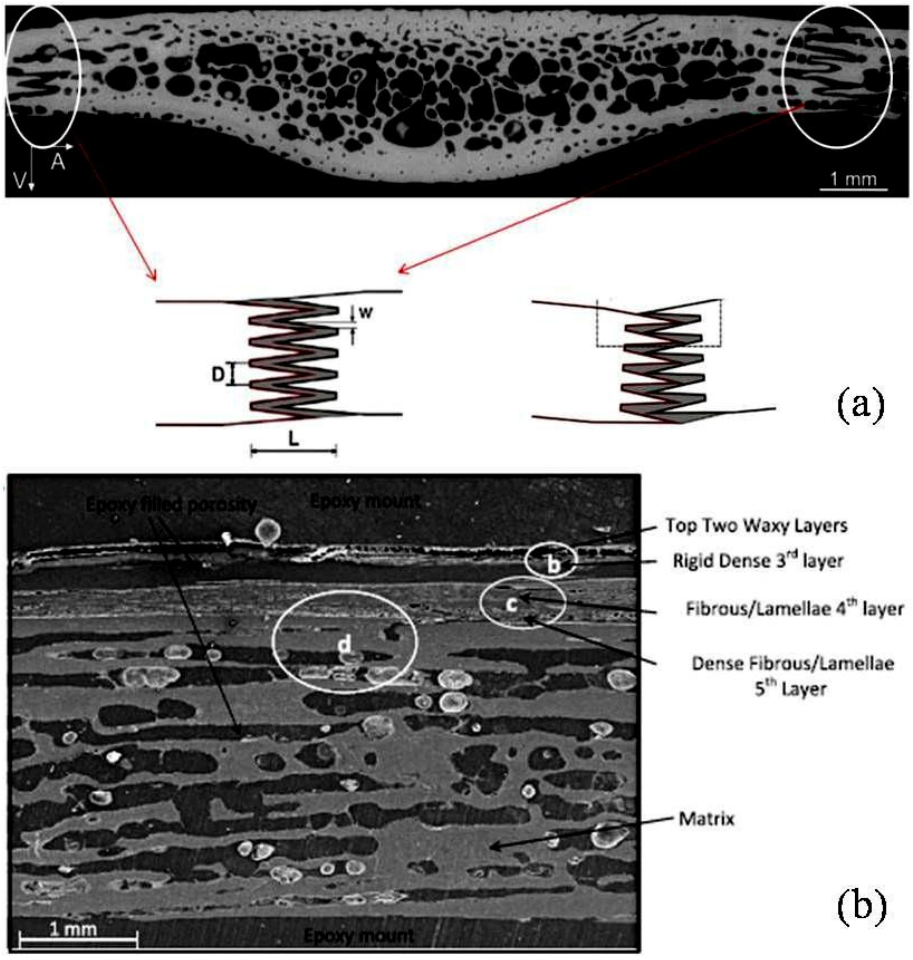

Fig. 1.27 (a) Sandwich structure of the turtle carapace shell; (b) Schematic of the interlocking joint; (c) Micromovement of the joint (Krauss et al., 2009).

It is recognized that the structure of the carapace shell is a sandwich structure, like that in the armadillo shell (discussed above). The sandwich structure consists of two thin but dense layers, which are known as endocortical and exocortical bone layers, and the porous trabecular bone, which can be often found in bones of other species (Fig. 1.25c or Fig. 1.26a; Krauss et al., 2009). The carapace shell is formed by series of individual plates, which are connected by zigzag joints (interlocking mechanism) and covered by a layer of keratinized scutes, which is the *β*-keratins (also found in armadillo, and crocodilian; Rhee et al., 2009; Valle et al., 2009), acts as a 'glue' to connect individual scutes together. In particular, Krauss et al. (2009) investigated the joint area (Fig. 1.27) in detail (50-80μm wide, 150-180μm long, and rotated by 35^{o}-45^{o} with respect to the normal axis of the shell surface), which enables turtles to move flexibly and bears high-magnitude impact loading when attacked by predators; they also presented a fundamental concept of structure-mechanics relationship to explain how the shell functions when imposed by loads with different magnitudes. Balani et al., (2011) explicited the multifunctions of turtle's carapace: (i) the waxy layer on surface is for slipping away from predators and reducing drag force while swimming, (ii) the third dense layer provides further shielding, (iii) multilayer and porous structures absorb shock caused by fall, and (iv) porous structure storing nutrient and fluids.

Mechanical property

A three bending experimental was performed by Krauss et al. (2009) to reveal the function of the suture (joint area) in the deformation process and the results showed that the stiffness of the samples with suture was low in the initial phase (slight movement due to walk) and gradually transited to a high stiffness as loads increased (external attack), while the stiffness of the samples without suture started with a high value (Fig. 1.28a). The behavior provided a good explanation about the mechanical properties during the locomotion and protection. Rhee et al. (2009) performed hardness, compression and flexure tests, respectively. They reported that the hardness of the exterior and interior layer of the sandwich structure were comparable (≈1 GPa) and also for their elastic modulus (≈20 GPa). The deformation mechanism was attributed to the middle porous layer which had a similar behavior as that of honeycombs, i.e. linear-elastic phase (due to trabecular beam bending), platform phase (trabecular beam buckling), and densification phase (trabecular beam crushing; Papka and Kyriakides, 1994; Gibson and Ashby, 1997), because of the single exterior and interior layers have

no platform phases (Fig. 1.28b).

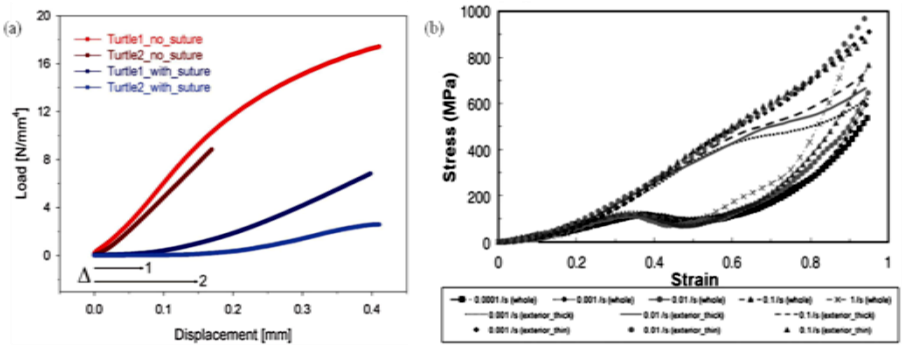

Fig. 1.28 (a) Mechanical function of the suture (Krauss et al., 2009); (b) The constitutive curves of the sandwich structure, single interior layer, and single exterior layer (Rhee et al., 2009).

1.8 Plant stem

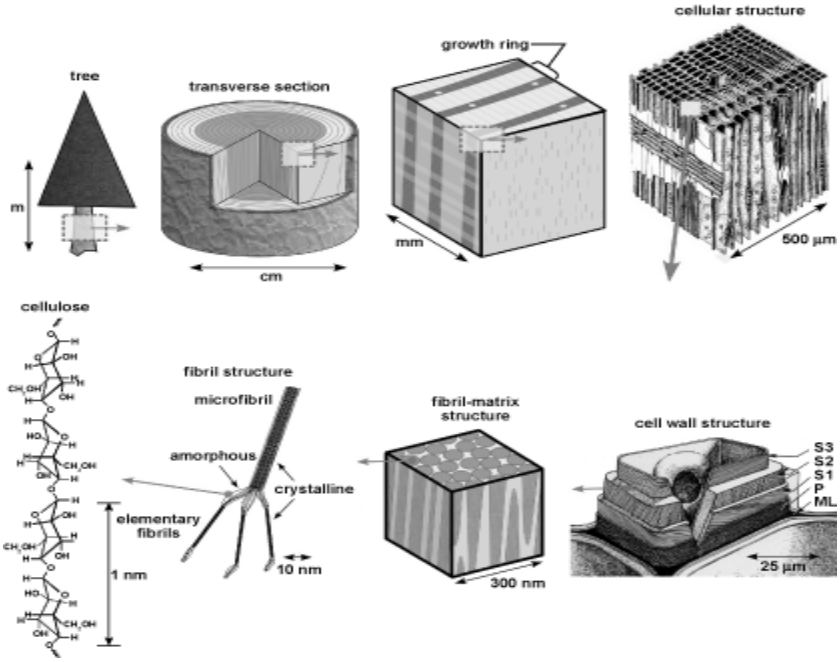

Fig. 1.29 Schematic of hierarchical structure of wood (Moon, 2008)

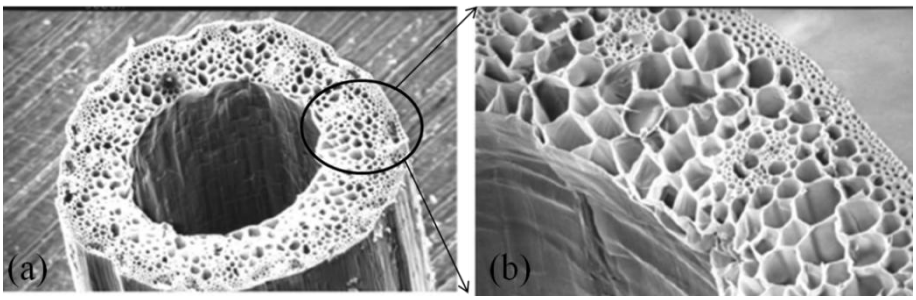

Fig. 1.30 (a) Cross-section of the grass stem; (b) Magnification of the part in (a) (Gibson, 2005).

Plant stem plays an important role in the growth process, and one of the most important functions is providing the mechanical support in order to adapt to surrounding environment. We can understand this easily by imagining that the plant stem carries torque/bending moment and vibrates when wind comes. Most of plant stems are circular and porous structure (Bejan, 2000), e.g. tree stem (Fig. 1.29) and grass stem (Fig. 1.30). This is because the circular shape possesses a largest area compared with other polygons under the condition of the same perimeter and the porous architecture has the low-weight and stronger energy-absorbing properties.

Structural models

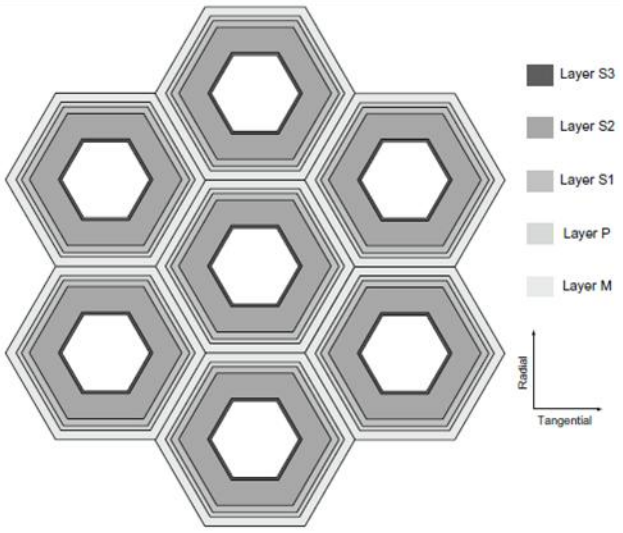

Fig. 1.31 Schematic of the cross-section of the hierarchical model (Qing and Mishnaevsky, 2009).

Regarding hierarchical structure of the plant stem (Fig. 1.29), Hofstetter and Gamstedt (2008) reviewed the developments in the field of hierarchical modeling of the hygro-elastic behavior of wood. They focus on the on composite micromechanical models for the wood cell wall and on multiscale models for wood resting upon hierarchical finite element models; meanwhile, they pointed out that to understand fundamental aspects of wood required taking into account the heterogeneity, anisotropy and hierarchies. Qing and Mishnaevsky (2009) built a 3D hierarchical model (Fig. 1.31) with heterogeneous multiple-layer cell walls, which are similar to that of the natural honeycomb (Zhang et al., 2010); moreover, they studied the influences of the microfibril angles, thickness of the cell walls, layers, shape of the cell cross-section and wood density on the elastic constants.

Mechanical investigation

The structure of plant stems was treated as a cylindrical shell with foam by Karam and Gibson (1994)—the outer shell was full dense materials and porous structure was the core (Fig. 1.29); at the same time, the elastic buckling behavior of the thin-walled structure was analyzed by theoretical investigation (Karam and Gibson, 1995a) and verified by experiments (Karam and Gibson, 1995b). Basing on the thin-walled tubes/shell, Niklas (1997a, 1998) examined material properties (Young's modulus and critical stress) of stem tissues by examining the mechanical behavior of hollow internodes with transverse nodal septa subjected to bending and twisting and the failure modes of hollow, septate stems; also, he studied the vibrating responses of the tube stem with node (e.g. bamboo) and found that the nodes acted mechanically like a series of spring, which could be used to store strain energy except stiffening the hollow cylindrical structure (Niklas, 1997b). In order to determine sclerenchyma cells are the main components that resist stem bending and the mechanical properties of stems, Evans et al. (2007) studied 42 species of grass plants and discovered that 59% of all sclerenchyma cells in stems occur in the outer one-fifth radius of stems (Fig. 1.30), which is the main support for stem integrity.

About the formation of the hollow structure, here we give an obvious explanation: The hollow natural structure is explained in the view of torsion, the critical shear stress $\tau=Tr/J$, where r is the external radius of the tube, T is the moment of torque, and J is the polar moment of inertia. From the expression of the critical shear stress, we can see that the larger r, the larger τ; in other words, the shear capacity increases as r increases,

therefore, the mass distribution is better when the shell is far from the core.

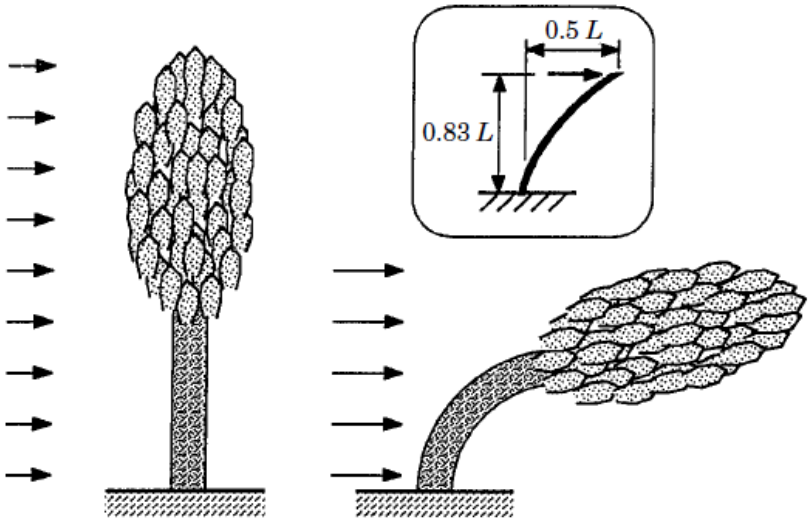

Fig. 1.32 Simple model of passive automatic adjustment (Schulgasser and Witztum, 1997).

As for the structural efficiency, Wegst and Ashby (2007) optimized the mechanical properties of orthotropic tube, stalk and stem, which included the shape and anisotropy, by considering stiffness, strength and Failure by ovalisation, instability and local kinking. Incorporating heterogeneity and highly anisotropy, Schulgasser and Witztum (1997) investigated the strength of vascular plant stems and they reported that the plant stem sacrifices the strength and vertical stability in order to reduce the external bending moment (Fig. 1.32), which is the so-called "passive automatic adjustment" mechanism, and that as the height increases, the plant tends to develop a high anisotropic tissue arrangements in order to gain high bending stiffness to maintain its stability. For the mechanics of natural cellular materials, which is one type of the four kinds of natural materials, Gibson (2005) reviewed their mechanics and discussed their roles in natural sandwich structure (e.g. skull, trabecular bone) basing on their developed theory (Gibson and Ashby, 1997).

Chen and Pugno (2011) here discuss out-plane mechanical efficiency for a circular and hexagonal honeycomb (Fig. 1.33), and according to the elevation indices, the critical condition is computed in Fig. 1.34. We can see that under the line, circular honeycomb is more efficient; above the line, the hexagonal honeycomb is more efficient.

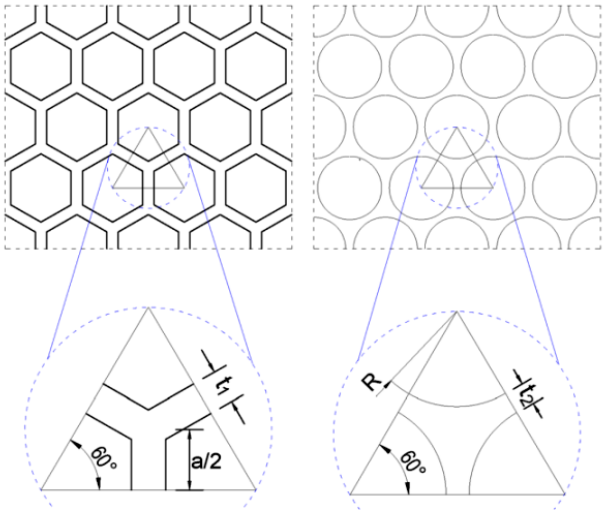

Fig. 1.33 Circular and hexagonal honeycomb structure.

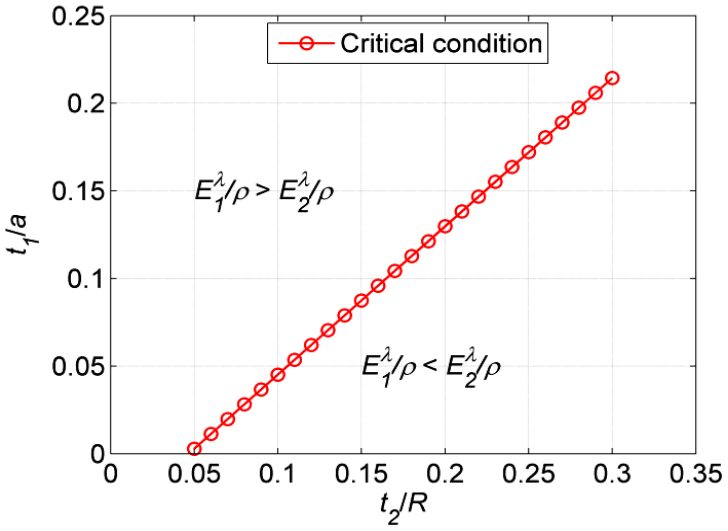

Fig. 1.34 Efficiency between the two kinds of honeycomb.

Chapter 2

Hierarchical Woven Tissues: Elasticity

In this Chapter, the elastic properties of 2-D woven hierarchical tissues are modeled, considering matrix transformation and stiffness averaging, assuming for the warp and fill yarns (level 0) an orthotropic material. The tissues at level 1 are considered as the fabric composed of warp or fill yarn at level 0. Warp and fill yarns at level 1 are defined as "pieces" of such 1-level tissue and have a different mismatch between the inclination of their longitudinal axes and those of the composing sub-fibers. Similarly, based on warp and fill yarns at level 1, we generate warp and fill yarns at level 2 and thus tissues with 2 hierarchical levels, and so on. We compare our theory with experiments on tendons from the literature and on leaves performed by ourselves. The result shows the possibility of designing a new class of hierarchical 2-D scaffolds by tailoring the elastic anisotropy, better matching the anisotropy of the biological tissues and thus maximizing the regeneration at each hierarchical level.

2.1 Introduction

Tissue engineering seeks to repair or regenerate tissues through combinations of implanted cells, biomaterial scaffolds and biologically active molecules. The rapid restoration of tissue biomechanical function needs to replicate structural and mechanical properties using novel scaffold design (Moutos et al., 2003). The structure of a tissue may be described at several levels, with dimensions ranging from nano-scale

to macro-scale, e.g. in describing a tendon, there are several distinctive levels from collagen molecule to the tendon itself (Cowin and Doty, 2007; Baer et al., 1992). Many soft biological or artificial tissues exhibit the anisotropic, inhomogeneous and nonlinear mechanical behaviors (Pugno, 2006, 2010; Pugno and Carpinteri, 2008; Pugno et al., 2008), because of the random orientation and mechanical properties of collagen molecule, e.g. the heart valve tissue (Cox et al., 2008).

Accordingly, many contributions are today devoted to create bio-scaffolds with varieties of structures in order to match the structural and mechanical properties of natural tissues, a key requirement to maximize the tissue regeneration; moreover, a broad range of fabrication technologies are employed from earlier textile technologies to computational topology design (CTD) and solid free-form fabrication (SFF) (Ma, 2004; Liu et al., 2007; Hollister, 2005). Even so, the structural hierarchy is still difficult to be produced, or if some hierarchical structures can be developed, they are not controllable. In this regard, it seems that a little success has been achieved. Moutos et al. (2003) developed a three-dimensional woven composite scaffold with the proper anisotropy for cartilage tissue engineering; experimental results showed that the mechanical properties are comparable to those of the native articular cartilage.

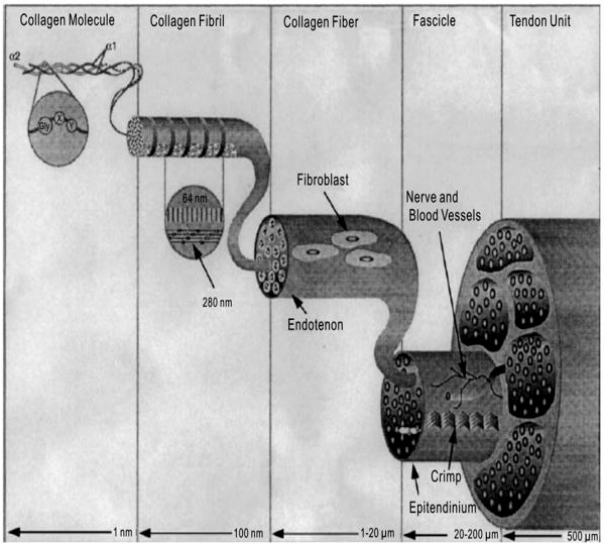

Fig.2.1 Schematic of the structural hierarchy in tendons

Moreover, recent literature focuses on multiscale modeling of biological

materials in physiological and disease states (Buheler and Yung, 2009), and specifically on applications to collagenous tissues such as bone and others (Ritchie et al., 2009). Especially, Buehler and his group studied the collagen molecule and fibril by molecular simulation, respectively (Buehler and Wong, 2007; Buehler, 2006). Besides, from the evolutionary angle, they explained how nature can built a strong hierarchical structure by weak materials (Buheler, 2010a, 2010b).

Differently from other multiscale models, based on self-similar or quasi-self-similar statistics (Pugno, 2006; Zhang et al., 2010), we here consider a fully deterministic approach. The intrinsic material properties appearing at the zero level in our woven fabric hierarchical model could be *ab-initio* derived from fully atomistic simulations, as successfully done by Tang et al. (2009) for nonwoven hierarchical composites.

Tendons are typical hierarchical biological structures. They have five hierarchical levels, ranging from the collagen molecule, collagen fibril, collagen fiber, fascicle and the tendon itself, see Fig. 2.1 (Silver et al., 2003). The mechanical properties of the first three levels were investigated by Yang (2008) basing on atomic force microscopy (AFM). Sasaki & Odajima (1996a, 1996b) and Bozec & Horton (2005) investigated the mechanical properties of the single collagen molecule by X-ray diffraction technology and AFM: the former determined stress-strain relationship and estimated the longitudinal Young's modulus of the collagen molecule; the later focused on the mechanical response of type I collagen monomer. Van der Rijt et al. (2006) found the Young's modulus of the single fibril in ambient conditions and in aqueous media by AFM, respectively, (Yang et al., 2008) using scanning mode bending tests performed with an AFM, gave the bending moduli of single electrospun type I collagen fibers, both at ambient conditions and in phosphate buffered saline (PBS). As for the collagen fascicles, Yin & Elliott (2004) built a transversely isotropic biphasic mixture model and studied the viscoelastic properties of collagen fascicles from mouse tail tendons; also Young's moduli and Poisson's ratios were reported.

Leaf is another example of hierarchical biological material. Due to its interesting mechanical properties (for instance, tensile strength and elastic modulus), plant fibers used in some composite materials have drawn attention. Some papers (Arib et al., 2006; Devi et al., 1998; George et al., 1995; Mishra et al., 2004) about mechanical property of pineapple leaf fiber and sisal fiber and their related bio-composites have contributed to this topic.

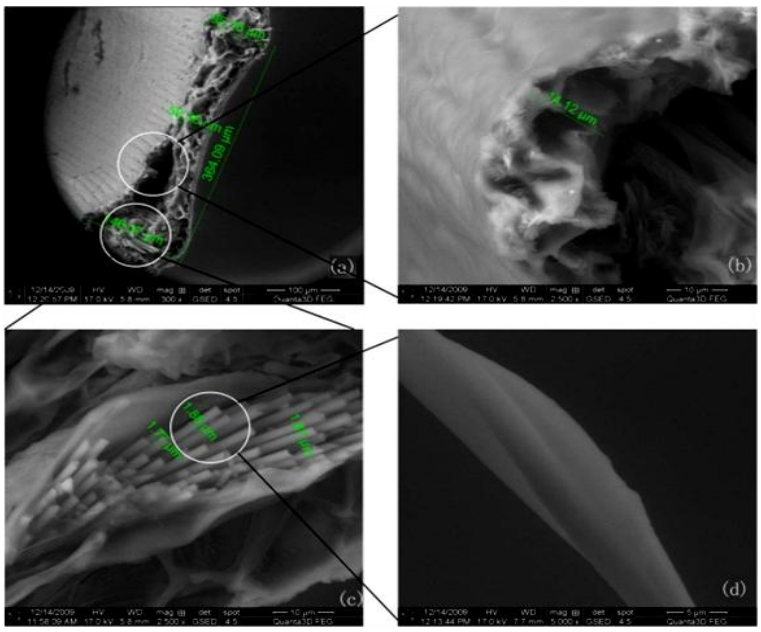

Fig.2.2 The structural hierarchy of the Aechmea aquilegia leaf sample under SEM. (a, leaf, (b) fiber bundle, (c) single fiber.

In this chapter, the 2-dimensional hierarchical woven tissues, treated with the methods of continuum mechanics and the stiffness averaging, are investigated in order to design scaffolds with desired anisotropic elasticity. In particular, the anisotropy of the scaffolds is controllable by changing the angle between fill and warp yarns and/or the volumetric fractions of fibers at different hierarchical levels. Experimental results of tendons from the literature and performed by ourselves on leaves are compared with the theoretical predictions. We investigate here the hierarchical properties of the Aechmea aquilegia leaf. Aechmea aquilegia leaf is modeled with three hierarchical levels, according to observations of the cross sections that we made with a scanning electron microscopy (SEM) (Fig. 2.2).

This chapter is organized into seven sections: after this Introduction, Section 2.2 presents the theory which is used in the design of tissues. The derivation formulas of elastic properties for general hierarchical tissues are derived in Section 2.3. In Section 2.4, two kinds of self-similar structures are introduced and investigated in detail, and parametric analyses are performed for the orientation angles and the relative volumetric ratios of warp to fill yarns. In Section 2.5, the comparison of tendons between theoretical prediction and experimental results from the literature proceeds. In Section

2.6, experiments on the Aechmea aquilegia leaf that we carried out are described and compared with our hierarchical theory. Finally, concluding remarks are made in Section 2.7.

2.2 Matrix Transformation and Stiffness Averaging

In this section, two fundamental steps that we use to model hierarchical tissues, i.e. matrix transformation and stiffness averaging, are illustrated.

It is well known in the mechanics of composite (Christensen, 1979) that the stiffness matrix of composite structures can be obtained by linear volumetric averaging for particular conditions, including the case of plane reinforcement composites. Since our theory treats only the in-plane elastic behavior of the tissue, we adopt here, as done in previous papers (Fu et al., 2007), the stiffening average method. The complexity of our model is in fact not due to out-of-plane configurations but rather to the considered hierarchical geometry. Other more sophisticated methods, such as the principle of equivalent homogeneity and polydisperse or three-phase model could also be invoked.

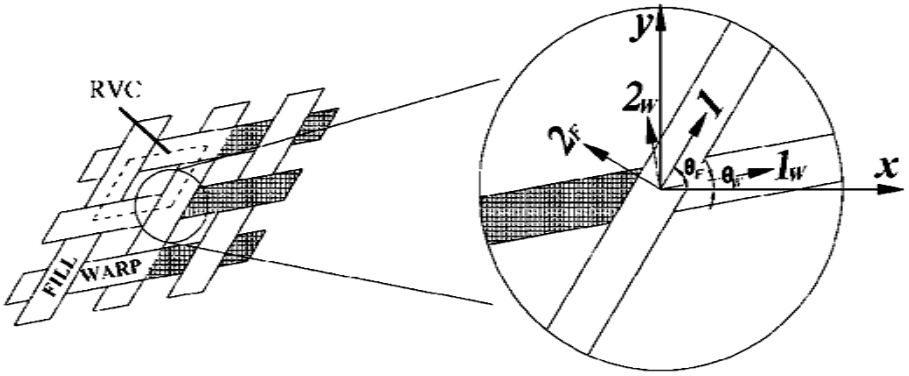

Fig. 2.3 Schematic of the woven structure.

Two local coordinate systems (1_W-2_W for warp yarns and 1_F-2_F for fill yarns) and a global coordinate system (x-y) are introduced (Fig. 2.3). Warp and fill yarns are assumed to be orthotropic. According to the coordinate system transformation matrix [T], in the global coordinate system, the stress-strain relationship of single yarn (fill and warp) can be expressed by the stress $\{\sigma_{\alpha\beta}\}$ and strain tensor $\{\varepsilon_{\alpha\beta}\}$ as (Gibson,

1994):

$$\{\sigma_{\alpha\beta}\}=[T]^{-1}\{\sigma^*_{\alpha\beta}\}=[T]^{-1}\left[Q^*\right]\{\varepsilon^*_{\alpha\beta}\}=[T]^{-1}\left[Q^*\right][T]\{\varepsilon_{\alpha\beta}\} \quad \alpha,\beta=1,2 \tag{2.1}$$

where $\left[Q^*\right]$ is the elastic matrix in the local coordinate system.

then, the new elastic matrix $[Q]$ in the global coordinate system can be expressed as a function of the fiber elastic properties and fiber orientation:

$$[Q]=[T]^{-1}\left[Q^*\right][T] \tag{2.2}$$

thus, for fill (warp) yarns, the relationship between the elastic matrices $\left[Q^*\right]_i$ and $[Q]_i$ is:

$$[Q]_i=[T(\theta_i)]^{-1}\left[Q^*\right]_i[T(\theta_i)] \quad (i=F,W) \tag{2.3}$$

$[T(\theta_i)]$ is the transformation matrix for an orientation angle θ_i made by the local coordinate axis 1_i and the global coordinate axis x (Fig. 2.3); the angle θ_i is defined as a positive when it is counterclockwise.

For the 2-dimensional case, the elastic matrix of fill (warp) yarns in local coordinate system is:

$$\left[Q^*\right]_i=\begin{pmatrix} Q^*_{11,i} & Q^*_{12,i} & 0 \\ Q^*_{21,i} & Q^*_{22,i} & 0 \\ 0 & 0 & 2Q^*_{66,i} \end{pmatrix} \tag{2.4}$$

where $Q^*_{\alpha\beta,i}$ are components of the elastic matrix (2.4), which are defined as:

$$Q^*_{11,i}=\frac{E_{1,i}}{1-\mu_{12,i}\mu_{21,i}},\ Q^*_{12,i}=\frac{\mu_{21,i}E_{1,i}}{1-\mu_{12,i}\mu_{21,i}},\ Q^*_{22,i}=\frac{E_{2,i}}{1-\mu_{12,i}\mu_{21,i}},\ Q^*_{66,i}=G_{12,i}$$

with $E_{\alpha,i}$ Young's moduli, $\mu_{\alpha\beta,i}$ Poisson's ratios and $G_{\alpha\beta,i}$ shear moduli, of fill yarns along the specified directions.

thus, the elastic matrix of fill (warp) yarns in the global coordinate system is:

$$[Q]_i=\begin{pmatrix} Q_{11,i} & Q_{12,i} & 2Q_{16,i} \\ Q_{21,i} & Q_{22,i} & 2Q_{26,i} \\ Q_{61,i} & Q_{62,i} & 2Q_{66,i} \end{pmatrix} \tag{2.5}$$

the transformation matrix $[T(\theta_i)]$ is:

$$[T(\theta_i)]=\begin{pmatrix}\cos^2\theta_i & \sin^2\theta_i & 2\cos\theta_i\sin\theta_i\\ \sin^2\theta_i & \cos^2\theta_i & -2\cos\theta_i\sin\theta_i\\ -\cos\theta_i\sin\theta_i & \cos\theta_i\sin\theta_i & \cos^2\theta_i-\sin^2\theta_i\end{pmatrix} \tag{2.6}$$

note that the relationship: $[T(\theta_F)][T(\theta_W)]=[T(\theta_F+\theta_W)]=[T(\theta_W)][T(\theta_F)]$ holds; moreover, when $\theta_F+\theta_W=k\pi$, (k=0, ±1, ±2…), $[T(\theta_F)]$ and $[T(\theta_W)]$ are reciprocal.

If warp and fill yarns are treated as two different materials, then, based on the stiffness averaging method, we find the elastic matrix for the woven structure (Bogdanovich and Pastore, 1996):

$$[Q]=\sum_i\left(\frac{V_i}{\sum_i V_i}[Q]_i\right)+\left(1-\frac{V_i}{\sum_i V_i}\right)[Q]_M=\sum_i\left(v_i[Q]_i\right)+\left(1-\sum_i v_i\right)[Q]_M \tag{2.7}$$

in which we assume the presence of a filling matrix (subscription *M*), otherwise:

$$[Q]=\sum_i\left(\frac{V_i}{\sum_i V_i}[Q]_i\right)=\sum_i\left(v_i[Q]_i\right) \tag{2.8}$$

where, V_i is fill-yarn (warp-yarn) volumes in a representative volumetric cell (RVC) (Fig. 2.3); v_i is fill-yarn (warp-yarn) volumetric fractions; $[Q]_M$ is the stiffness matrix of the matrix.

Following Lee et al. (2003) and extending their results of plain woven, the calculations of these volumetric fractions are given below. Firstly, two geometric arrangements are assumed (Mcbride and Chen, 1997):

(1) The cross-sectional shape of yarns is assumed to be lenticular (Fig. 2.4);
(2) Yarns are incompressible and yarn to yarn distance between two overlaps is constant.

taking fill yarns for an example and basing on these two assumptions, the main geometric parameters are expressed as follows (Fig. 2.4) (Lee et al., 2003):

$$a_F=\frac{a_F^{90}}{\sin(\theta_F-\theta_W)} \tag{2.9}$$

$$r_F = \frac{1}{4d_F}(d_F^2 + a_F^2) \tag{2.10}$$

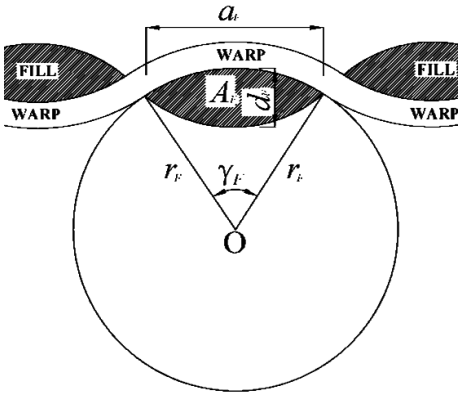

Fig. 2.4 Schematic of the fill yarn's cross-section.

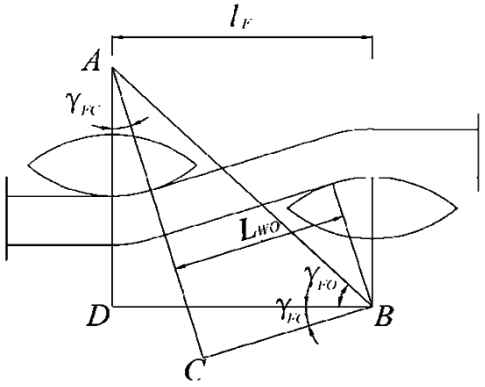

Fig. 2.5 Geometrical relationships

$$\gamma_F = 2\sin^{-1}\left(\frac{2a_F d_F}{d_F^2 + a_F^2}\right) \tag{2.11}$$

$$A_F = r_F^2(\gamma_F - \sin\gamma_F) \tag{2.12}$$

where a_F^{90} denotes fill yarn width when fill and warp yarns are perpendicular to each other, a_F and d_F are its width and thickness, respectively; r_F , γ_F and A_F are radius, central angle and cross-sectional area of fill yarns, see Fig. 2.4 for details.

A simple geometric analysis (Fig. 2.5) gives the length of the segments AD and AC:

$$\overline{AD} = 2r_F + d_W - d_F\,;\ \ \overline{AC} = 2r_F + d_W \tag{2.13}$$

with the above outcomes, the length of the segment *AB* can be obtained ($l_F = \overline{DB}$) as:

$$\overline{AB} = \sqrt{{l_F}^2 + \left(2r_F + d_W - d_F\right)^2} \tag{2.14}$$

thus, the "crimp angle" γ_{FC} , see Fig. 2.5, is calculated as:

$$\gamma_{FC} = \left(\gamma_{FO} + \gamma_{FC}\right) - \gamma_{FO} = \sin^{-1}\left(\frac{2r_F + d_W}{\sqrt{{l_F}^2 + \left(2r_F + d_W - d_F\right)^2}}\right) - \sin^{-1}\left(\frac{2r_F + d_W - d_F}{\sqrt{{l_F}^2 + \left(2r_F + d_W - d_F\right)^2}}\right)$$

(2.15)

where, γ_{FO} is defined in Fig. 2.5.

then, formulas used to calculate the crimp, oblique and horizontal lengths of single warp yarn in a representative unit cell are respectively found as:

$$L_{WC} = \gamma_{FC}\left(2r_F + d_W\right) \tag{2.16}$$

$$L_{WO} = \sqrt{l_F{}^2 - 2d_F\left(2r_F + d_W\right) + d_F{}^2} \tag{2.17}$$

$$L_{WH} = 0 \tag{2.18}$$

Likewise, we can get the lengths of three parts for fill yarns by substituting the subscript *W* with *F* into Eqs. (2.9)-(2.18). Thus, V_W and V_F can be determined.

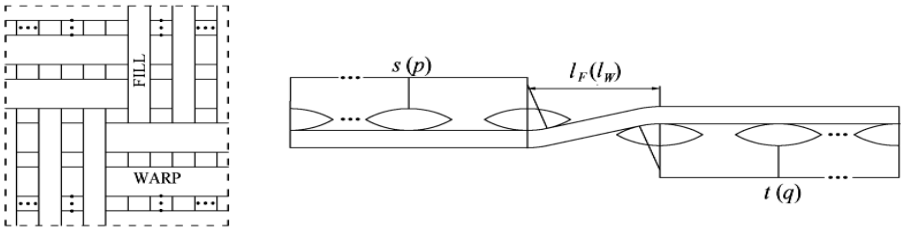

Fig. 2.6 Schematics of a generalized woven fabric.

For the generalized textile (Fig. 2.6), we similarly find:

$$V_U = (d_F + d_W)(s+t-1)l_F\,(p+q-1)l_W\,;\begin{cases} V_W = (p+q-1)A_W\,(L_{WC} + L_{WO} + L_{WH}) = N_W A_W L_W \\ V_F = (s+t-1)A_F\,(L_{FC} + L_{FO} + L_{FH}) = N_F A_F L_F \\ V_P = V_U - V_W - V_F \end{cases}$$

(2.19)

$$v_W = \frac{V_W}{V_W + V_F + V_P} = \frac{V_W}{V_U}\,;\quad v_F = \frac{V_F}{V_W + V_F + V_P} = \frac{V_F}{V_U} \tag{2.20}$$

where N_W and N_F are the total numbers of warp and fill yarns in the representative unit cell; L_W and L_F are the lengths of warp and fill yarns, respectively, in the representative unit cell. Also, it is worth noting that L_{WC} and L_{WO} are identical to those calculated by Eqs. (2.16) and (2.17); however, L_{WH} and L_{FH} are no longer

equal to zero (for the previous case, in fact, $s+t=p+q=1$):

$$L_{WH}=(s+t-1)l_F;\ L_{FH}=(p+q-1)l_W \tag{2.21}$$

where, s and t (p and q) are the numbers of fill (warp) yarns above and below warp (fill) yarns in the representative unit cell, see Fig. 2.6; l_F or l_W is yarn-to-yarn distance in the fill or warp direction.

2.3 General Hierarchical Theory

At each hierarchical level, the structure is modeled as a continuum (Lakes, 1993). For the sake of simplicity, we begin by neglecting the matrix (Fig. 2.7).

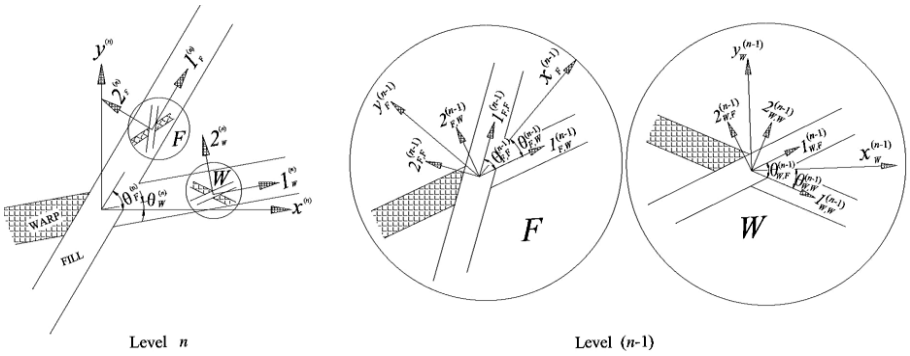

Fig. 2.7 Schematic of the hierarchical tissue.

The level 1 structure has four independent geometric parameters, i.e. the two volumetric fractions and the two orientation angles, the level 2 structure has thus twelve independent geometric parameters, and a tissue composed by n hierarchical levels has $4\times(2^n-1)$ independent geometric parameters, in addition to the eight elastic constants of the two materials at level 0.

Level 1 structure:

We define the level 0 structure as the single yarn (fill or warp) which is composed by parallel fibers. Eqs. (2.3)-(2.6) can be rewritten as:

$$[Q]_i^{(0)}=\left[T(\theta_i^{(1)})\right]^{-1}\left[Q^*\right]_i^{(0)}\left[T(\theta_i^{(1)})\right] \tag{2.22}$$

$$\left[Q^*\right]_i^{(0)} = \begin{pmatrix} Q^{*(0)}_{11,i} & Q^{*(0)}_{12,i} & 0 \\ Q^{*(0)}_{21,i} & Q^{*(0)}_{22,i} & 0 \\ 0 & 0 & 2Q^{*(0)}_{66,i} \end{pmatrix} \tag{2.23}$$

with $Q^{*(0)}_{11,i} = \dfrac{E^{(0)}_{1,i}}{1-\upsilon^{(0)}_{12,i}\upsilon^{(0)}_{21,i}}$, $Q^{*(0)}_{12,i} = \dfrac{\upsilon^{(0)}_{21,i}E^{(0)}_{1,i}}{1-\upsilon^{(0)}_{12,i}\upsilon^{(0)}_{21,i}}$, $Q^{*(0)}_{22,i} = \dfrac{E^{(0)}_{2,i}}{1-\upsilon^{(0)}_{12,i}\upsilon^{(0)}_{21,i}}$, $Q^{*(0)}_{66,i} = G^{(0)}_{12,i}$

$$\left[Q\right]_i^{(0)} = \begin{pmatrix} Q^{(0)}_{11,i} & Q^{(0)}_{12,i} & 2Q^{(0)}_{16,i} \\ Q^{(0)}_{21,i} & Q^{(0)}_{22,i} & 2Q^{(0)}_{26,i} \\ Q^{(0)}_{61,i} & Q^{(0)}_{62,i} & 2Q^{(0)}_{66,i} \end{pmatrix} \tag{2.24}$$

$$\left[T(\theta_i^{(1)})\right] = \begin{pmatrix} \cos^2\theta_i^{(1)} & \sin^2\theta_i^{(1)} & 2\cos\theta_i^{(1)}\sin\theta_i^{(1)} \\ \sin^2\theta_i^{(1)} & \cos^2\theta_i^{(1)} & -2\cos\theta_i^{(1)}\sin\theta_i^{(1)} \\ -\cos\theta_i^{(1)}\sin\theta_i^{(1)} & \cos\theta_i^{(1)}\sin\theta_i^{(1)} & \cos^2\theta_i^{(1)} - \sin^2\theta_i^{(1)} \end{pmatrix} \tag{2.25}$$

The elastic matrices of warp and fill yarns at the 0th hierarchical level transformed from the local coordinate systems to the global coordinate system, can be expressed as:

$$\left[Q\right]_{i,j}^{(0)} = \left[T(\theta_{i,j}^{(1)})\right]^{-1}\left[Q^*\right]_j^{(0)}\left[T(\theta_{i,j}^{(1)})\right] \quad (i, j = F, W) \tag{2.26}$$

by volumetric averaging, the final result for the 1st level is found:

$$\left[Q\right]_i^{(1)} = \sum_j v_{i,j}^{(1)}\left[T(\theta_{i,j}^{(1)})\right]^{-1}\left[Q^*\right]_j^{(0)}\left[T(\theta_{i,j}^{(1)})\right] \tag{2.27}$$

employing Eqs. (2.19) and (2.20), the fiber volumes and volumetric fractions in warp and fill yarns can be determined:

$$V_{i,j}^{(1)} = N_{i,j}^{(1)} A_{i,j}^{(0)} L_{i,j}^{(1)} \tag{2.28}$$

$$v_{i,j}^{(1)} = V_{i,j}^{(1)} / V_{i,U}^{(1)} \tag{2.29}$$

$A_{i,j}^{(0)}$ are calculated using Eq. (2.12); $L_{i,j}^{(1)}$ are obtained thanks to Eqs. (2.16), (2.17) and (2.21).

Level 2 structure:

Similarly, for the second level we can write:

$$\left[Q\right]_{i,j}^{(1)} = \left[T(\theta_{i,j}^{(2)})\right]^{-1}\left[Q^*\right]_j^{(1)}\left[T(\theta_{i,j}^{(2)})\right] \tag{2.30}$$

$$[Q]_i^{(2)} = \sum_j v_{i,j}^{(2)} \left[T(\theta_{i,j}^{(2)})\right]^{-1} \left[Q^*\right]_j^{(1)} \left[T(\theta_{i,j}^{(2)})\right] \tag{2.31}$$

$$V_{i,j}^{(2)} = N_{i,j}^{(2)} A_{i,j}^{(1)} L_{i,j}^{(2)} \tag{2.32}$$

$$v_{i,j}^{(2)} = V_{i,j}^{(2)} / V_{i,U}^{(2)} \tag{2.33}$$

Level *n* structure:

Thus, in general, we have:

$$[Q]_{i,j}^{(n-1)} = \left[T(\theta_{i,j}^{(n)})\right]^{-1} \left[Q^*\right]_j^{(n-1)} \left[T(\theta_{i,j}^{(n)})\right] \tag{2.34}$$

$$[Q]_i^{(n)} = \sum_j v_{i,j}^{(n)} \left[T(\theta_{i,j}^{(n)})\right]^{-1} \left[Q^*\right]_j^{(n-1)} \left[T(\theta_{i,j}^{(n)})\right] \tag{2.35}$$

$$V_{i,j}^{(n)} = N_{i,j}^{(n)} A_{i,j}^{(n-1)} L_{i,j}^{(n)} \tag{2.36}$$

$$v_{i,j}^{(n)} = V_{i,j}^{(n)} / V_{i,U}^{(n)} \tag{2.37}$$

where, $\left[Q^*\right]_j^{(n-1)}$ are the stiffness matrices of fill (or warp) yarns of level (n-1) in the local systems at level n; $T(\theta_{i,j}^{(n)})$, $[Q]_{i,j}^{(n-1)}$ and $v_{i,j}^{(n)}$ are transformation matrix, post-transformation stiffness matrix and volumetric fraction of fill (or warp) yarns at level (n-1), composing the fill (or warp) yarns at level n; $[Q]_i^{(n)}$ are stiffness matrices of fill (or warp) yarns at level n, in the global coordinate system; $V_{i,j}^{(n)}$, $N_{i,j}^{(n)}$, $A_{i,j}^{(n-1)}$ and $L_{i,j}^{(n)}$ are volume, number, cross-sectional area and length of fill (warp) yarns at level n.

This process can also be used in the presence of just one type of fiber, e.g. by removing the warp yarns. Then, simplifying Eqs. (2.34), (2.35) and adding the matrix term, we have:

$$[Q]_i^{(n)} = \prod_{m=1}^{n} v_i^{(m)} \times \left[T(\sum_{m=1}^{n} \theta_i^{(m)})\right]^{-1} \left[Q^*\right]_i^{(0)} \left[T(\sum_{m=1}^{n} \theta_i^{(m)})\right] + (1 - \prod_{m=1}^{n} v_i^{(m)})[Q]_M \quad (i = F, W) \tag{2.38}$$

where, $v_i^{(m)}$ and $\theta_i^{(m)}$ are the volumetric fraction and orientation angle of the fiber at the m^{th} level, respectively; $\left[Q^*\right]_i^{(0)}$, $[Q]_M$ are the stiffness matrices of the fiber at the

0^{th} level in the local coordinate system and the matrix, respectively.

2.4 Self-similar hierarchical structures

The general hierarchical theory is complicated and in order to explain the process in a simple way, two kinds of self-similar hierarchical structures (Fig. 2.8(a) and (b)) are introduced here.

2.4.1 Self-similar case (1)

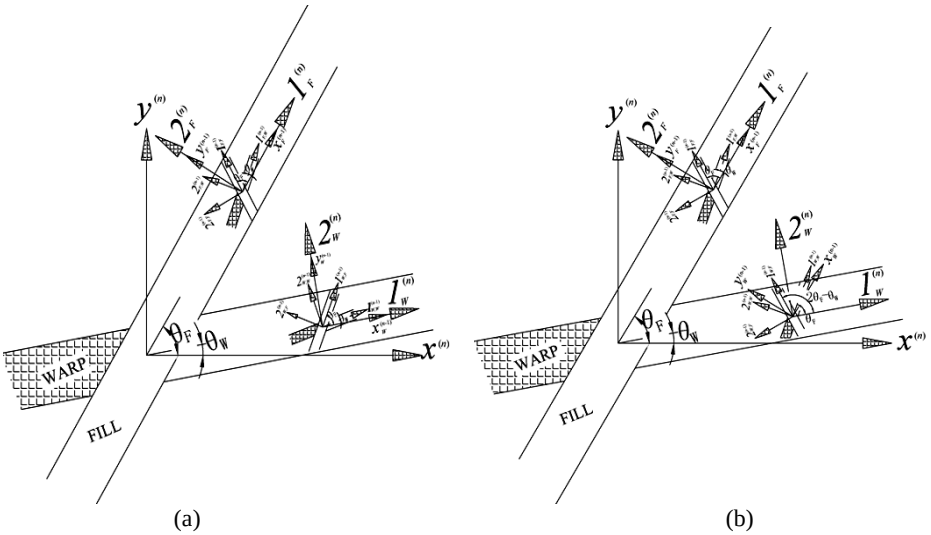

(a) (b)

Fig. 2.8 Schematic of the self-similar hierarchical structures.

In this case, the global coordinate systems of fill and warp yarns at the $(n-1)^{th}$ level are coincident with the local coordinate systems of fill and warp yarns at the n^{th} level, respectively; the configuration satisfies a set of self-similar conditions:

$$v_i = v_{j,i}^{(m)}, \quad \theta_i = \theta_{j,i}^{(m)} \tag{2.39}$$

thus, fill and warp yarns have identical sub-structure, i.e. $\left[Q^*\right]_F^{(i)} = \left[Q^*\right]_W^{(i)}$.

Level 1 structure:

Basing on Fig. 2.8(a) and the self-similar condition (2.39), Eq. (2.27) becomes:

$$[Q]_F^{(1)} = [Q]_W^{(1)} = v_F \left([T(\theta_F)]^{-1} \left[Q^* \right]_F^{(0)} [T(\theta_F)] \right) + v_W \left([T(\theta_W)]^{-1} \left[Q^* \right]_W^{(0)} [T(\theta_W)] \right) \quad (2.40)$$

Level 2 structure:

Correspondingly, the elastic matrices at the second level are expressed as:

$$\begin{aligned} [Q]_F^{(2)} = [Q]_W^{(2)} = {} & v_F^2 \left([T(2\theta_F)]^{-1} \left[Q^* \right]_F^{(0)} [T(2\theta_F)] \right) + v_F v_W \left([T(\theta_W + \theta_F)]^{-1} \left[\left[Q^* \right]_F^{(0)} + \left[Q^* \right]_W^{(0)} \right] [T(\theta_W + \theta_F)] \right) \\ & + v_W^2 \left([T(2\theta_W)]^{-1} \left[Q^* \right]_W^{(0)} [T(2\theta_W)] \right) \end{aligned} \quad (2.41)$$

Level n structure:

Likewise, using the recursive process and compacting the result, we find the elastic matrix of the n^{th} level as:

$$[Q]_F^{(n)} = [Q]_W^{(n)} = \sum_{m=0}^{n} v_F^{n-m} v_W^m \left([T(m\theta_W + (n-m)\theta_F)]^{-1} \left[a_{n,m} \left[Q^* \right]_F^{(0)} + b_{n,m} \left[Q^* \right]_W^{(0)} \right] [T(m\theta_W + (n-m)\theta_F)] \right) \quad (2.42)$$

where the coefficients ($a_{n,m}$, $b_{n,m}$) satisfy the following recursive relationship:

$$\begin{cases} a_{n,m} = a_{n-1,m-1} + a_{n-1,m} \\ b_{n,m} = b_{n-1,m-1} + b_{n-1,m} \\ C_n^m = a_{n,m} + b_{n,m} \end{cases} \quad (2.43)$$

with combination C_n^m.

Let us define $v_f = v_F + v_W$ as the fiber volumetric fraction and $\theta_m = n\theta_F + m(\theta_W - \theta_F)$, $\lambda = V_W / V_F$. Considering the filling of a matrix, we have:

$$\begin{aligned} [Q]^{(n)} = {} & \sum_{m=0}^{n} a_{n,m} v_f^n \frac{\lambda^m}{(1+\lambda)^n} \left([T(\theta_m)]^{-1} \left[Q^* \right]_F^{(0)} [T(\theta_m)] \right) + \sum_{m=0}^{n} b_{n,m} v_f^n \frac{\lambda^m}{(1+\lambda)^n} \left([T(\theta_m)]^{-1} \left[Q^* \right]_W^{(0)} [T(\theta_m)] \right) \\ & + \left(1 - v_f^n\right) [Q]_M \end{aligned} \quad (2.44)$$

The coefficients ($a_{n,m}$, $b_{n,m}$) are listed in Table 2.1 for n=1-8.

Furthermore, if volumetric fractions of fill and warp yarns are equal, i.e. $v_F = v_W$, Eq. (2.44) becomes:

$$[Q]^{(n)} = \left(\frac{v_f}{2} \right)^n \left\{ \sum_{m=0}^{n} a_{n,m} \left([T(\theta_m)]^{-1} \left[Q^* \right]_F^{(0)} [T(\theta_m)] \right) + \sum_{m=0}^{n} b_{n,m} \left([T(\theta_m)]^{-1} \left[Q^* \right]_W^{(0)} [T(\theta_m)] \right) \right\} + \left(1 - v_f^n\right) [Q]_M \quad (2.45)$$

Finally, when $\left[Q^*\right]_F^{(0)} = \left[Q^*\right]_W^{(0)} = \left[Q^*\right]_f^{(0)}$ and $\theta_F = \theta_W$, from Eq. (2.45), we have:

$$[Q]^{(n)} = v_f^n \left([T(n\theta_F)]^{-1} \left[Q^*\right]_f^{(0)} [T(n\theta_F)] \right) + \left(1 - v_f^n\right)[Q]_M \tag{2.46}$$

Eq. (2.46), which can also be obtained from Eq. (2.38) using the self-similar conditions (2.39), suggests that our theory is self-consistent.

Table 2.1 Coefficients ($a_{n,i}$, $b_{n,i}$) for n=1-8.

n	**($a_{n,0}$, $b_{n,0}$)**	**($a_{n,1}$, $b_{n,1}$)**	**($a_{n,2}$, $b_{n,2}$)**	**($a_{n,3}$, $b_{n,3}$)**	**($a_{n,4}$, $b_{n,4}$)**	**(a_{n5}, $b_{n,5}$)**	**($a_{n,6}$, $b_{n,6}$)**	**($a_{n,7}$, $b_{n,7}$)**	**($a_{n,8}$, $b_{n,8}$)**
1	(1,0)	(0,1)	-	-	-	-	-	-	-
2	(1,0)	(1,1)	(0,1)	-	-	-	-	-	-
3	(1,0)	(2,1)	(1,2)	(0,1)	-	-	-	-	-
4	(1,0)	(3,1)	(3,3)	(1,3)	(0,1)	-	-	-	-
5	(1,0)	(4,1)	(6,4)	(4,6)	(1,4)	(0,1)	-	-	-
6	(1,0)	(5,1)	(10,5)	(10,10)	(5,10)	(1,5)	(0,1)	-	-
7	(1,0)	(6,1)	(15,6)	(20,15)	(15,20)	(6,15)	(1,6)	(0,1)	-
8	(1,0)	(7,1)	(21,7)	(35,21)	(35,35)	(21,35)	(7,21)	(1,7)	(0,1)

2.4.2 Self-similar case (2)

In this case, the global coordinate systems of the $(n-1)^{\text{th}}$ level in fill and warp yarns are both coincident with the local coordinate system of fill yarns at the n^{th} level; and the configuration satisfies a set of self-similar conditions:

$$v_i = v_{j,i}^{(m)} \quad (i, j = F, W); \quad \theta_{F,F}^{(m)} = \theta_F, \quad \theta_{F,W}^{(m)} = \theta_W, \quad \theta_{W,F}^{(m)} = 2\theta_F - \theta_W, \quad \theta_{W,W}^{(m)} = \theta_F \tag{2.47}$$

thus, warp and fill yarns are composed of parallel sub-fibers i.e. $[Q]_F^{(m)} = [Q]_W^{(m)}$.

Based on Fig. 2.8(b) and the self-similar conditions (2.47), like case (1), the results from the 1st level to n^{th} level are expressed as:

Level 1 structure:

$$[Q]_F^{(1)} = [Q]_W^{(1)} = v_F \left([T(\theta_F)]^{-1} \left[Q^*\right]_F^{(0)} [T(\theta_F)] \right) + v_W \left([T(\theta_W)]^{-1} \left[Q^*\right]_W^{(0)} [T(\theta_W)] \right) \tag{2.48}$$

Level 2 structure:

$$[Q]_F^{(2)} = [Q]_W^{(2)} = (v_F + v_W)\left(v_F\left([T(\theta_F)]^{-1}\left[Q^*\right]_F^{(0)}[T(\theta_F)]\right) + v_W\left([T(\theta_W)]^{-1}\left[Q^*\right]_W^{(0)}[T(\theta_W)]\right)\right) \tag{2.49}$$

Level n structure:

$$[Q]_F^{(n)} = [Q]_W^{(n)} = (v_F + v_W)^{n\text{-}1}\left[v_F\left([T(n\theta_F)]^{-1}\left[Q^*\right]_F^{(0)}[T(n\theta_F)]\right) + v_W\left([T(\theta_W + (n-1)\theta_F)]^{-1}\left[Q^*\right]_W^{(0)}[T(\theta_W + (n-1)\theta_F)]\right)\right] \tag{2.50}$$

Defining $v_f = v_F + v_W$ and $\lambda = V_W / V_F$ and considering the effect of the matrix, Eq. (2.50) becomes:

$$[Q]^{(n)} = v_f^n \frac{1}{1+\lambda}\left([T(n\theta_F)]^{-1}\left[Q^*\right]_F^{(0)}[T(n\theta_F)]\right) + v_f^n \frac{\lambda}{1+\lambda}\left([T(n\theta_F + \theta_W - \theta_F)]^{-1}\left[Q^*\right]_W^{(0)}[T(n\theta_F + \theta_W - \theta_F)]\right) + \left(1 - v_f^n\right)[Q]_M \tag{2.51}$$

If volumetric fractions of fill and warp yarns are equal, i.e. $v_F = v_W$, Eq. (2.51) can be written as:

$$[Q]^{(n)} = \frac{v_f^n}{2}\left(\left([T(n\theta_F)]^{-1}\left[Q^*\right]_F^{(0)}[T(n\theta_F)]\right) + \left([T(n\theta_F + \theta_W - \theta_F)]^{-1}\left[Q^*\right]_W^{(0)}[T(n\theta_F + \theta_W - \theta_F)]\right)\right) + \left(1 - v_f^n\right)[Q]_M \tag{2.52}$$

If $\left[Q^*\right]_F^{(0)} = \left[Q^*\right]_W^{(0)} = \left[Q^*\right]_f^{(0)}$ and $\theta_F = \theta_W$, Eq. (2.52) is further simplified:

$$[Q]^{(n)} = v_f^n [T(n\theta_F)]^{-1}\left[Q^*\right]_f^{(0)}[T(n\theta_F)] + \left(1 - v_f^n\right)[Q]_M \tag{2.53}$$

we can see that Eqs. (2.53) and (2.46) are identical, suggesting the self-consistency of our approach again.

2.4.3 Orthogonal yarns for both self-similar hierarchical structures

Case (1): if $\theta_W = 0$ and $\theta_F = \pi/2$, Eq. (2.44) becomes:

$$[Q]^{(n)} = \sum_{m=0}^{n} a_{n,m} v_F^{n-m} v_W^m \left(\left[T((n-m)\frac{\pi}{2})\right]^{-1}\left[Q^*\right]_F^{(0)}\left[T((n-m)\frac{\pi}{2})\right]\right) + \sum_{m=0}^{n} b_{n,m} v_F^{n-m} v_W^m \left(\left[T((n-m)\frac{\pi}{2})\right]^{-1}\left[Q^*\right]_W^{(0)}\left[T((n-m)\frac{\pi}{2})\right]\right) + \left(1 - v_f^n\right)[Q]_M$$

(2.54)

It can be seen that the transformation matrix is dependent on $(n-m)$; thus, the final expression is:

$$[Q]^{(n)} = \sum_{m=0}^{n} a_{n,i} v_F^{n-m} v_W^m \left(\frac{1-(-1)^{n-m}}{2} \left[\overrightarrow{Q^*} \right]_F^{(0)} + \frac{1+(-1)^{n-m}}{2} \left[Q^* \right]_F^{(0)} \right) + \sum_{m=0}^{n} b_{n,m} v_F^{n-m} v_W^m \left(\frac{1-(-1)^{n-m}}{2} \left[\overrightarrow{Q^*} \right]_W^{(0)} + \frac{1+(-1)^{n-m}}{2} \left[Q^* \right]_W^{(0)} \right) + \left(1-v_f^n\right)[Q]_M$$

(2.55)

Herein, matrices $\left[\overrightarrow{Q^*} \right]_F^{(0)}$ and $\left[\overrightarrow{Q^*} \right]_W^{(0)}$ can be obtained by transforming $\left[Q^* \right]_F^{(0)}$ and $\left[Q^* \right]_W^{(0)}$ with the transformation matrix $\left[T(90^o) \right]$.

Case (2): when $\theta_W = 0$ and $\theta_F = \pi / 2$, Eq. (2.51) becomes:

$$[Q]^{(n)} = v_f^{n-1} v_F \left(\left[T(n\frac{\pi}{2}) \right]^{-1} \left[Q^* \right]_F^{(0)} \left[T(n\frac{\pi}{2}) \right] \right) + v_f^{n-1} v_W \left(\left[T((n-1)\frac{\pi}{2}) \right]^{-1} \left[Q^* \right]_W^{(0)} \left[T((n-1)\frac{\pi}{2}) \right] \right) + \left(1-v_f^n\right)[Q]_M$$

(2.56)

The transformation matrix is dependent on *n*, and the final expression is:

$$[Q]^{n} = v_f^{n-1} v_F \left(\frac{1+(-1)^{n}}{2} \left[Q^* \right]_F^{(0)} + \frac{1-(-1)^{n}}{2} \left[\overrightarrow{Q^*} \right]_F^{(0)} \right) + v_f^{n-1} v_W \left(\frac{1+(-1)^{n}}{2} \left[\overrightarrow{Q^*} \right]_W^{(0)} + \frac{1-(-1)^{n}}{2} \left[Q^* \right]_W^{(0)} \right) + \left(1-v_f^n\right)[Q]_M$$

(2.57)

where matrices $\left[\overrightarrow{Q^*} \right]_F^{(0)}$ and $\left[\overrightarrow{Q^*} \right]_W^{(0)}$ are the same as those introduced in Eq. (2.55).

2.4.4 Parametric Analysis

Eqs. (2.44) and (2.51) hint that the elastic matrices at the n^{th} level are dependent on the fiber orientation angles θ_W and θ_F and the relative volumetric ratio λ of warp to fill yarns when the total fiber volumetric fraction v_f^n is fixed. Here, assuming the

both self-similar models, we investigate the influence of its specific components employing elastic parameters of a collagen molecule (Table 2.2). The changes of the six elastic parameters ($E_x^{(n)}$, $E_y^{(n)}$, $\mu_{xy}^{(n)}$, $G_{xy}^{(n)}$, $Q_{16}^{(n)}$ and $Q_{26}^{(n)}$, i.e. Young's moduli, Poisson's ratio, shear modulus and shear-coupling parameters in global coordinate system of the hierarchical level *n*) are reported below.

Table 2.2 Material constants of each level in tendon (MPa). (Note: 1=Lavagnino et al., 2008; 2=Yang, 2008; 3=Yang, et al., 2008; 4=Van der Rijt et al., 2006; 5=Kato et al., 1989; 6=Magnusson et al., 2007; 7=Yin and Elliott, 2004; 8=Lemos et al., 2008; 9=Quapp and Weiss, 1998; 10=Lynch et al., 2003)

(0^o)	Matrix	Molecule		Fibril		Fiber		Fascicle		Tendon
	Input	T	R	T	R	T	R	T	R	Input
E_1	1[1]	3536	350-12000[2]	2397	2000-7000[3]	1534	150-1000[4]	1066	480-1390[6]	750[8]
E_2	1[1]	53.2	-	36.4	-	25.1	-	17.3	-	12[9]
μ_{12}	0.25	3.16	-	3.13	-	3.10	-	3.05	2.73[7]	2.98[10]
G_{12}	0.4	22.3	-	15.7	31-81[2]	10.7	27-50[5]	7.3	-	5[8]

Note that, "T" stands for theoretical prediction; "R" stands for reference values; "Input" stands for input parameters. The same meaning is available in other tables

Influence of orientation angles

In order to investigate the influence of the orientation angles, we fix θ_W =30^o, λ=1.0, v_f^n =0.20 and we vary θ_F. Three values of θ_F are selected: π/2, π/3 and π/4. The comparisons of the six parameters defined above, for case (1) and case (2), are reported in Figs. 2.9 and 2.10, respectively.

From Fig. 2.9 we can see that the amplitude (here simply called *A*) of each parameter becomes greater as the orientation angle made by warp and fill yarns decreases; moreover, the rapidity of convergence also becomes slower. The cause for this is that the characteristic period is extended as the orientation angle decreases, reducing the rapidity of the homogenization. For Young's moduli $E_x^{(n)}$ and $E_y^{(n)}$, we note that they approach the same value, and are complementary at the same level (Fig. 2.9(a)-(b)). Poisson's ratio $\mu_{xy}^{(n)}$ tends to be 0.5 (Fig. 2.9(c)); however, when *n* and the orientation angle are small, it is beyond the isotropic upper limit of 0.5 and even negative but within the isotropic lower limit of -1. This is due to the large difference between transverse and longitudinal Young's moduli of the collagen molecule. Shear

modulus $G_{xy}^{(n)}$ has a different behavior with respect to the other parameters. For different orientation angles, when n tends to infinity, an order relationship $G_{xy}^{(n)}(\pi/2) > G_{xy}^{(n)}(\pi/3) > G_{xy}^{(n)}(\pi/4)$ holds. Finally, $Q_{16}^{(n)}$ and $Q_{26}^{(n)}$ show that the shear-coupling effect for higher hierarchical level disappears, see Fig. 2.9(e) and (f).

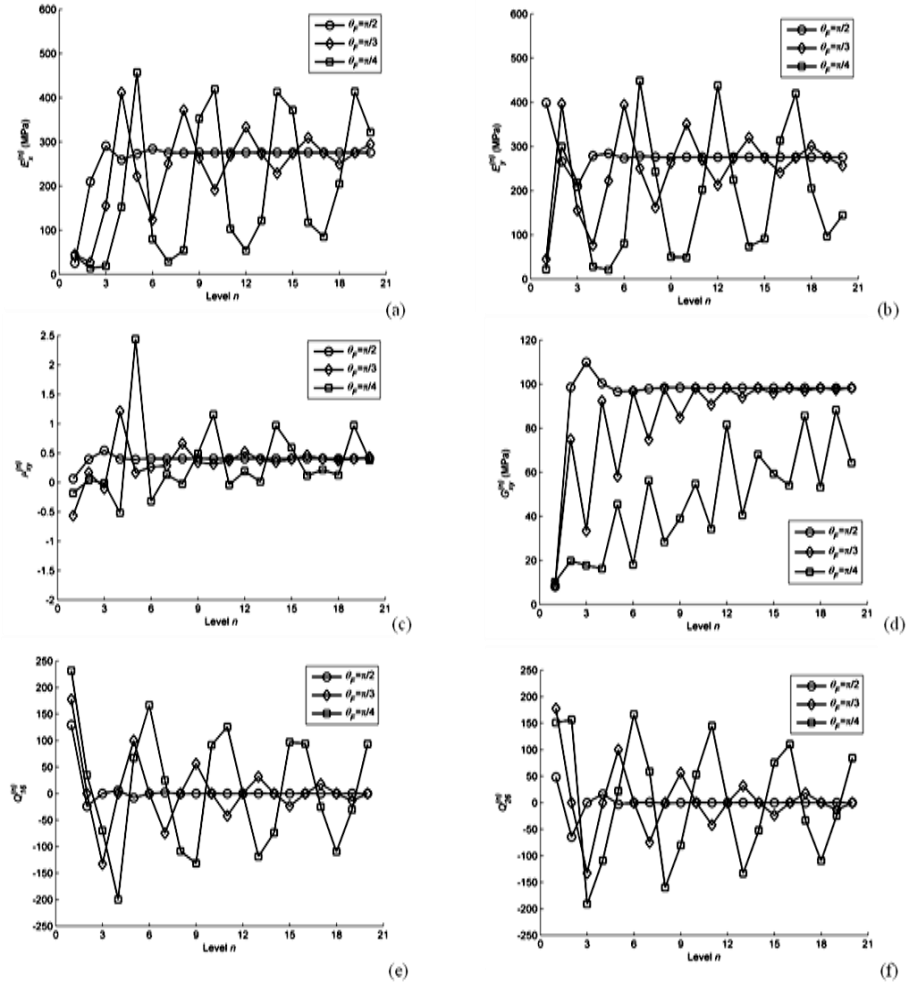

Fig. 2.9 Independent material constants and shear-coupling parameters with different orientation angles, for case (1).

Fig. 2.10 shows that all these six elastic parameters share a characteristic for case (2), namely, the periodicity. Like in case (1), Young's moduli $E_x^{(n)}$ and $E_y^{(n)}$ (Fig. 2.10(a) and (b)) are complementary, but they do not approach a fixed value as n tends

to infinity, and neither the amplitude (A) for each parameter shrinks (or extends) as the orientation angle made by warp and fill yarns decreases (e.g. for $E_x^{(n)}$,we find the relationship $A(\pi/2) \approx A(\pi/4) > A(\pi/3)$).

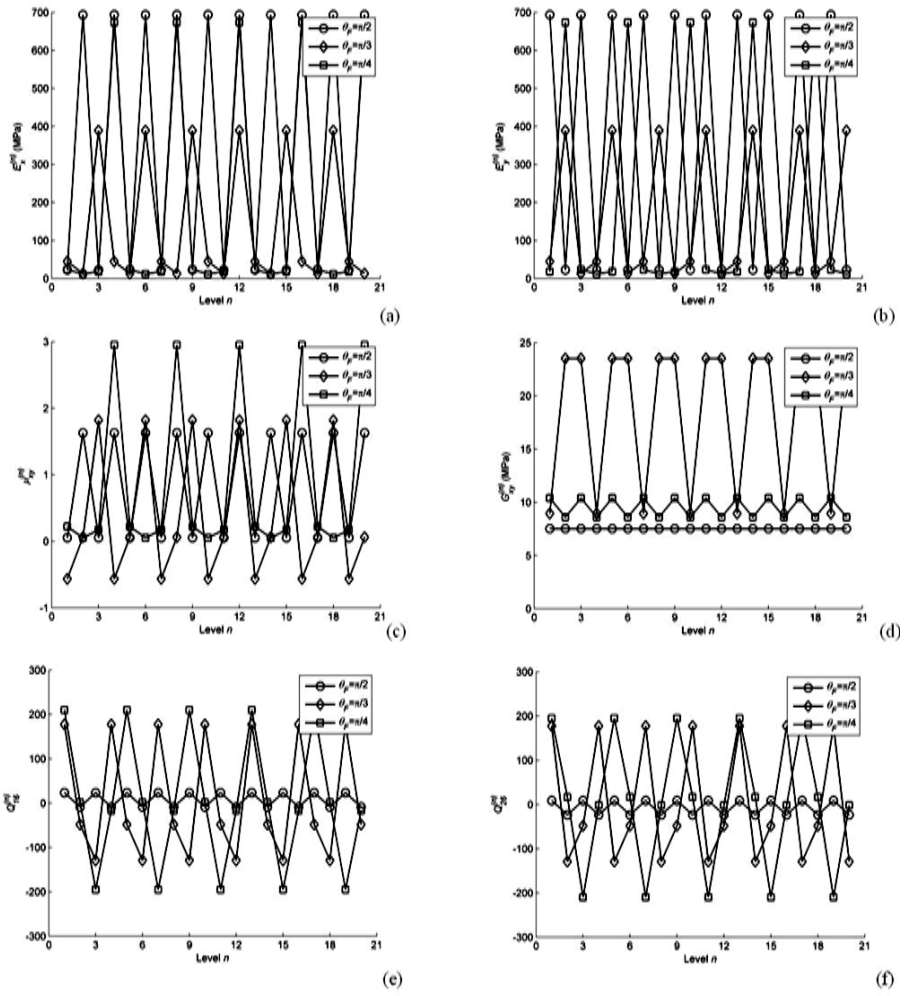

Fig. 2.10 Independent material constants and shear-coupling parameters with different orientation angles for case (2).

Influence of the relative volumetric ratio of warp to fill yarns

In order to investigate the influence of the relative volumetric ratio (λ) of warp to

fill yarns, we fix θ_W =30°, θ_F =60°, v_f^n =0.20 and vary λ. Three values of λ are selected: 10.0, 1.0 and 0.1. The comparisons of the previous six parameters, for case (1) and case (2), are depicted in Fig. 2.11 and Fig. 2.12, respectively.

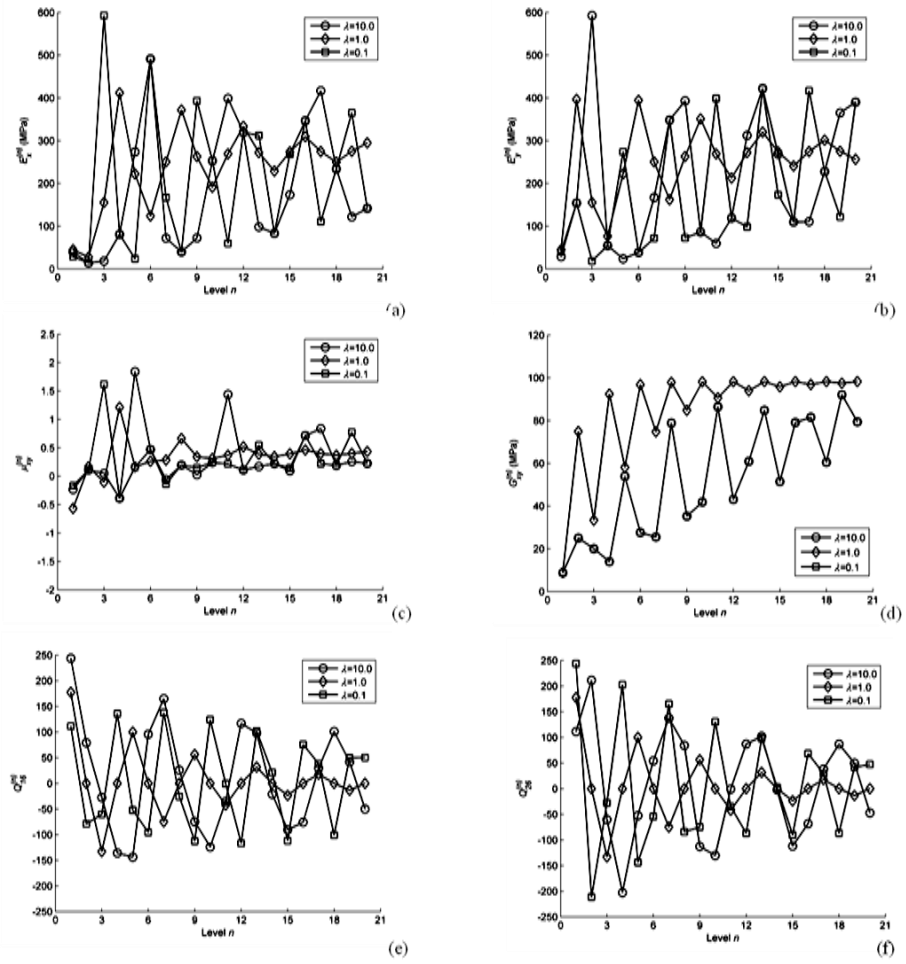

Fig. 2.11 Independent material constants and shear-coupling parameters with different relative volumetric ratios of warp yarns to fill yarns, for case (1).

In this situation, as *n* increases, the six parameters tend to a constant more slowly for λ=10.0 and λ=0.1 than for λ=1.0, and the amplitude (*A*) for λ=1.0 shrinks regularly, while irregularly for λ=10.0 and λ=0.1 (see Fig. 2.11(b) and (d)). Young's moduli $E_x^{(n)}$ and $E_y^{(n)}$ and Poisson's ratio $\mu_{xy}^{(n)}$ converge to the same values of those for case (1)

with varying orientation angle, due to the same constituents. Regarding the shear modulus, we find $G_{xy}^{(n)}(1.0) > G_{xy}^{(n)}(10.0) \equiv G_{xy}^{(n)}(0.1)$. This can be easily understood since λ=10.0 and λ=0.1 are equivalent to exchanging warp with fill yarns. Finally, the shear-coupling effect disappears as n tends to infinity.

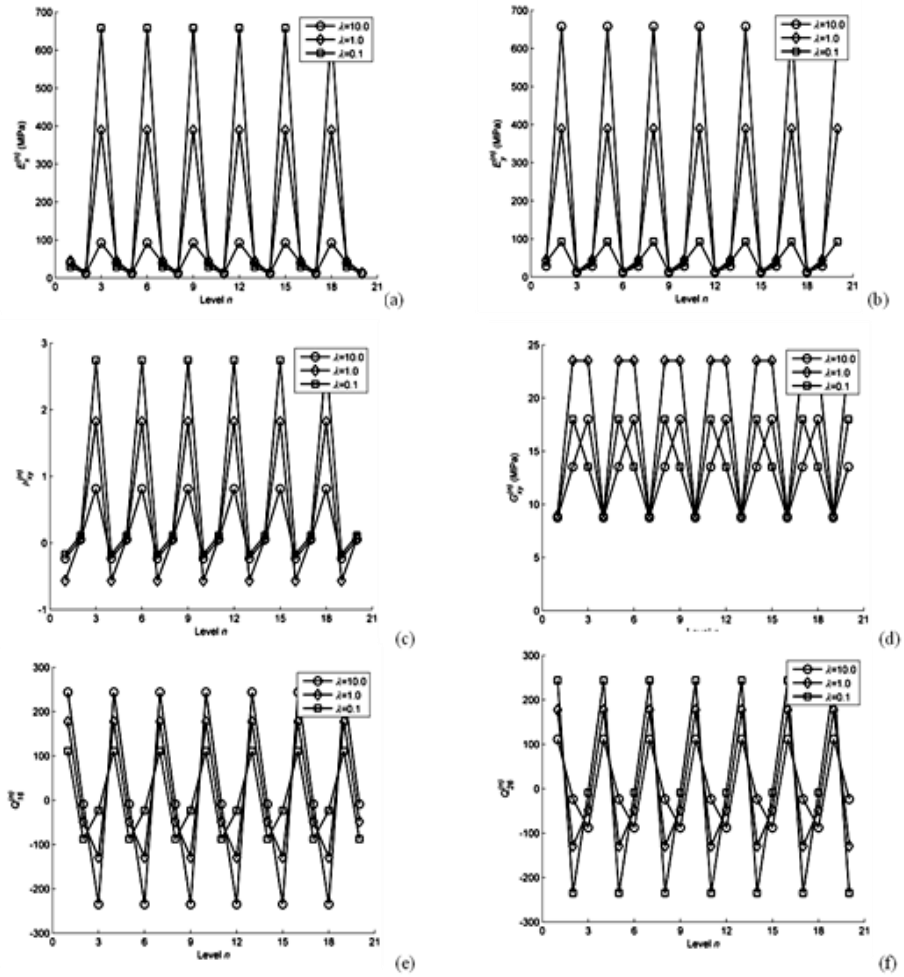

Fig. 2.12 Independent material constants and shear-coupling parameters with different relative volumetric ratios of warp yarns to fill yarns, for case (2).

For case (2), Fig. 2.12 shows that Young's moduli $E_x^{(n)}$ and $E_y^{(n)}$ and shear-coupling parameters $Q_{16}^{(n)}$ and $Q_{26}^{(n)}$ are complementary at the same level (Fig. 2.12(a),(b),(e),(f)) and the amplitudes (A) for these two pairs shrink or extend as the

volumetric ratio of warp to fill yarns decreases, i.e. we find $A(0.1) > A(1.0) > A(10.0)$ for $E_x^{(n)}$ and $A(10.0) > A(1.0) > A(0.1)$) for $Q_{16}^{(n)}$. This also happens for the Poisson's ratio $\mu_{xy}^{(n)}$. As for the shear modulus, when n=3k+1 (k=0, 1, 2...), $G_{xy}^{(3k+1)}(10.0) = G_{xy}^{(3k+1)}(1.0) = G_{xy}^{(3k+1)}(0.1)$; when n=3k+2 and n=3k+3 (k=0, 1, 2...), $G_{xy}^{(3k+2)}(0.1) = G_{xy}^{(3k+3)}(10.0) < G_{xy}^{(3k+2)}(1.0)$ and $G_{xy}^{(3k+2)}(10.0) = G_{xy}^{(3k+3)}(0.1) < G_{xy}^{(3k+3)}(1.0)$.

2.4.5 Comparison between self-similar cases (1) and (2)

In order to select an appropriate structure to simulate a tissue, we compare the six elastic parameters of case (1) with those of case (2) by fixing the orientation angles $\theta_W = 30^\circ$, $\theta_F = 60^\circ$, the volumetric ratio $\lambda = 1$ of warp to fill yarns and the total volumetric fraction of fiber v_f^n =0.20. The results are reported in Fig. 2.13.

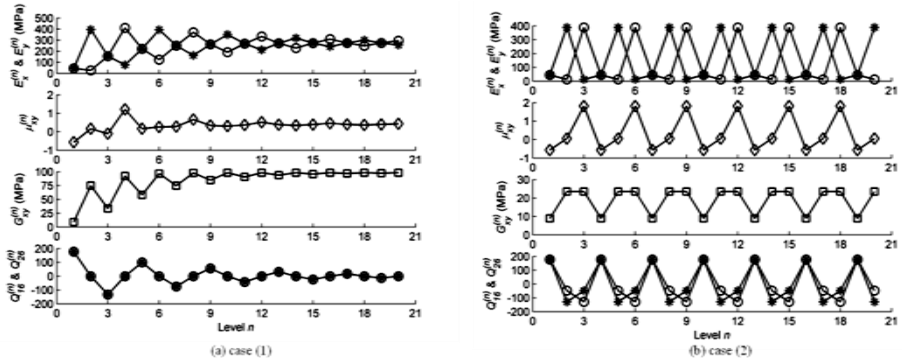

Fig. 2.13 Elements in the elastic matrices for both the two self-similar cases.

Comparing Figs. 2.9-2.12 with Fig. 2.13 suggests the existence of a general regularity. In case (1), each elastic independent constant tends asymptotically to a fixed value. When the level number n is odd, $E_x^{(n)}$ and $E_y^{(n)}$ are equal; instead, when n is even, the gap between the two becomes smaller. In case (2), each constant has the same period π/θ_F (in this case, the period is 3). When n=3k+1 (k=0, 1, 2...), $E_x^{(3k+1)} = E_y^{(3k+1)}$, while, when n=3k+2 and n=3k+3 (k=0, 1, 2...), $E_x^{(3k+2)} = E_y^{(3k+3)}$ and $E_x^{(3k+3)} = E_y^{(3k+2)}$. Similarly, $\mu_{xy}^{(n)}$ and $G_{xy}^{(n)}$ oscillate periodically.

In fact, in case (1), as n approaches infinity, the whole structure becomes closer to a homogenous material. In case (2), this is due to the same arrangement of warp and

fill yarns at each level; thus, the structure at different levels has an orientation periodicity.

2.5 Influence of constituents on overall elasticity of tendons

2.5.1 Volumetric fractions of collagen and matrix

Tendons are constituted mainly of fibers of fibrous type I collagen and are dense, often parallel-fibered, tissues. Generally, tendon consists of about 20% cellular material and about 80% extracellular material; the extracellular material is further subdivided into about 30% solids and 70% water. These extracellular solids are collagen, proteoglycan and a small amount of elastin (Cowin and Doty, 2007).

Here, tendon is treated as a woven hierarchical material only composed by fill yarns, and it considered as a composite materials made by two phases, i.e. collagen and matrix. Proteoglycan and water are treated as the matrix. Mow et al. (1990) give the weight percentage of the constituents in tendons, i.e. 23% for collagen, 7% for proteoglycan and 70% for water. Thus, the volume fractions can be derived from the densities: 1.2 g/cm^3 for collagen (Pidaparti et al., 1996), 1.4 g/cm^3 for proteoglycan (Paulsson et al., 1987) and 1.0 g/cm^3 for water. Accordingly, the volumetric fractions 79% and 21% are calculated for matrix and collagen, respectively.

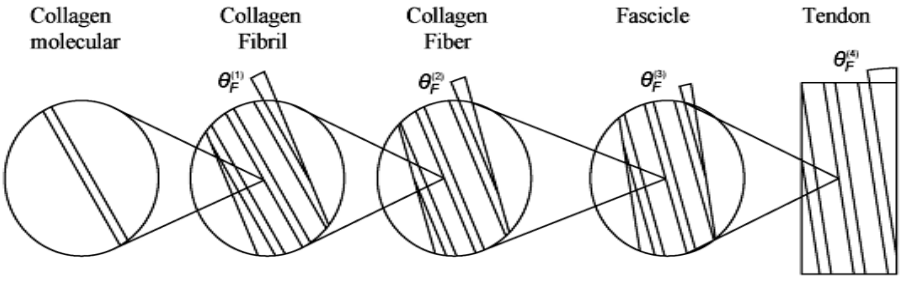

Fig. 2.14 Schematic of the hierarchical model of a tendon.

2.5.2 Influence of different variables

The considered architecture is show in Fig.2.14.

As discussed before, tendons are defined as a parallel-fibered tissue, i.e., the

included angles made by $(m-1)^{\text{th}}$ and m^{th} levels is equal to zero. Under the conditions of $v_f^{(m)} = 0.667$, easily deduced from $v_f = 21\%$ and $\theta_F^{(m)} = 0$, the elastic constants of the collagen molecules are derived from the experimental data of the tendon and matrix. Moreover, the material constants of collagen fibril, collagen fiber and fascicle are also derived by employing Eq. (2.38). These results are reported in Table 2.2.

Table 2.3, Material constants of each level with varying elastic constants of tendon (MPa). (Note: 1=Lavagnino et al., 2008; 2=Yang, 2008; 3=Yang, et al., 2008; 4=Van der Rijt et al., 2006; 5=Kato et al., 1989; 6=Magnusson et al., 2007; 7=Yin and Elliott, 2004; 8=Ito et al., 1998; 9=Lichtwark and Wilson, 2005; 10=Quapp and Weiss, 1998; 11=Lynch et al., 2003; 12=Lemos et al., 2008; 13=Sasaki and Odajima, 1996; 14=Scott and Loeb, 1995)

(0^o)	Matrix	Molecule		Fibril		Fiber		Fascicle		Tendon
	Input	T	R	T	R	T	R	T	R	Input
Varying the longitudinal Young's modulus of tendon										
E_1	1[1]	680-5060	350-12000[2]	463-3429	2000-7000[3]	317-2324	150-1000[4]	217-1577	480-1390[6]	150[8]-1070[9]
E_2	1[1]	53.2-53.4	-	36.4-36.5	-	24.9-25.0	-	17.2-17.3	-	12[10]
μ_{12}	0.25	3.04-3.16	-	3.03-3.14	-	3.02-3.10	-	3.00-3.05	2.73[7]	2.98[11]
G_{12}	0.4	22.3	-	15.2	31-81[2]	10.4	27-50[5]	7.2	-	5[12]
Varying the longitudinal Poisson's ratio of tendon										
E_1	1[1]	3450-3568	350-12000[2]	2346-2416	2000-7000[3]	1599-1636	150-1000[4]	1093-1108	480-1390[6]	750[12]
E_2	1[1]	53.1-53.3	-	36.3-36.4	-	24.9-25.0	-	17.2-17.2	-	12[10]
μ_{12}	0.25	0.43-5.77	-	0.43-5.74	-	0.43-5.70	-	0.43-5.65	2.73[7]	0.42-5.57[11]
G_{12}	0.4	22.3	-	15.2	31-81[2]	10.4	27-50[5]	7.2	-	5[12]
Varying the longitudinal shear modulus of tendon										
E_1	1[1]	3536	350-12000[2]	2397	2000-7000[3]	1626	150-1000[4]	1104	480-1390[6]	750[12]
E_2	1[1]	53.2	-	36.4	-	25.0	-	17.2	-	12[10]
μ_{12}	0.25	3.16	-	3.13	-	3.10	-	3.05	2.73[7]	2.98[11]
G_{12}	0.4	93.7-950.9	-	63.6-643.9	31-81[2]	43.2-436.0	27-50[5]	29.4-295.3	-	20-200[13,14]

By investigating the upper and lower bound of the elastic constants of each level of tendons, the influences of different variables are reported in Table 2.3. These results show that these influences are mainly controlled by the reciprocal theorem, namely $E_1 \mu_{21} = E_2 \mu_{12}$. However, the shear modulus produces no influence on the other constants; the reason is that the orthotropic material has no shear-coupling effect when the inclination angle approach zero.

2.5.3 Influence of collagen orientation

The previous description about the structure of tendons is parallel. However, the anisotropy of the angular distribution of collagen fibrils in a sheep tendon was investigated using 1H double-quantum (DQ) filtered nuclear magnetic resonance (NMR) signals: the angular distribution of collagen fibrils around the symmetric axis of the tendon was measured by the anisotropy of the residual dipolar couplings and described by a Gaussian function with a standard deviation of $12^o \pm 1^o$and with the center of the distribution at $4^o \pm 1^o$ (Fechete et al., 2003).

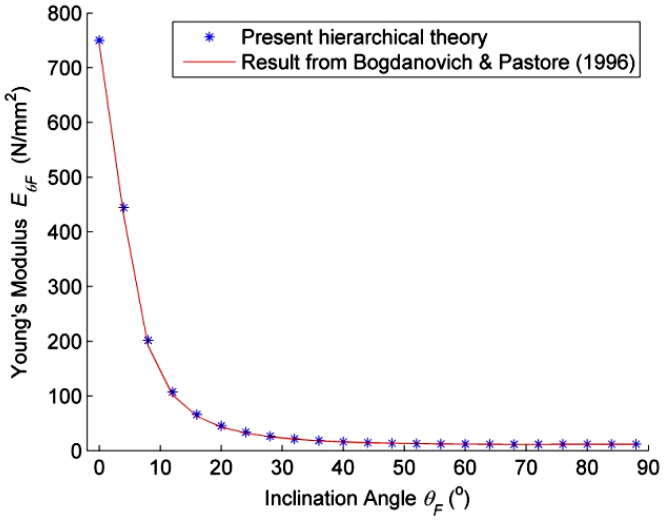

Fig.2.15 Comparison between hierarchical theory and literature.

Accordingly, here, we change $\theta_F^{(m)}$ with 7.5^o incremental from 0^o to 22.5^o. Meanwhile, the included angle made by collagen molecule and tendon is $4\theta_F^{(m)}$, i.e. in the range 0^o-90^o. The predictions are listed in Table 2.4.

The hierarchical prediction of the Young's modulus is plotted in Fig.2.15 and compared with a different approach from the literature (Bogdanovich and Pastore, 1996). Fig.2.15 shows that the result determined by a different theory is slightly lower than that determined by our hierarchical theory.

Table 2.4 Material constants of each level with different orientation angles (MPa).
Note: 1=Lavagnino et al., 2008; the orientation angle is between collagen molecule and tendon.

	Matrix	Molecule	Fibril	Fiber	Fascicle	Tendon
	Input	Input	T	T	T	T
Orientation angle 30°						
E_1	1[1]	3536	682	155	54	24
E_2	1[1]	53.2	36.2	24.6	17.0	12.0
μ_{12}	0.25	3.16	1.29	0.79	0.65	0.57
G_{12}	0.4	22.3	15.8	12.1	9.8	8.4
Orientation angle 60°						
E_1	1[1]	3536	226	50	21	12
E_2	1[1]	53.2	35.9	25.1	20.8	23.8
μ_{12}	0.25	3.16	0.79	0.57	0.44	0.29
G_{12}	0.4	22.3	17.6	17.4	15.5	8.4
Orientation angle 90°						
E_1	1[1]	3536	114	30	17	12
E_2	1[1]	53.2	35.8	30.2	53.8	750
μ_{12}	0.25	3.16	0.65	0.44	0.20	0.05
G_{12}	0.4	22.3	20.8	22.5	9.8	5

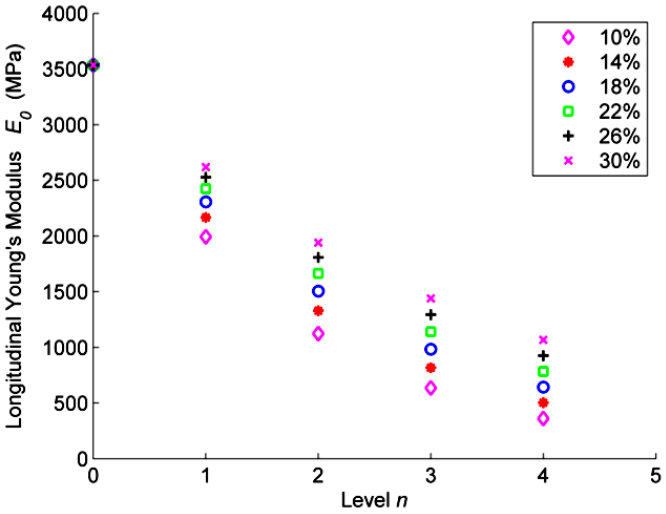

Fig.2.16 Comparison of different volume fractions.

2.5.4 Influence of the total volume of collagen

The volumetric fraction of the collagen molecule is another important parameter influencing the material constants. Here, the elastic constants of the collagen molecule, reported in Table 2.2, are employed to investigate its influence when varying in the range 10-30%, with incremental 4% at each hierarchical level, see Fig. 2.16. The result demonstrates that the elastic properties increase as the total volume of collagen increases.

2.6 Experiments on the Aechmea aquilegia leaf

2.6.1 Experimental procedure

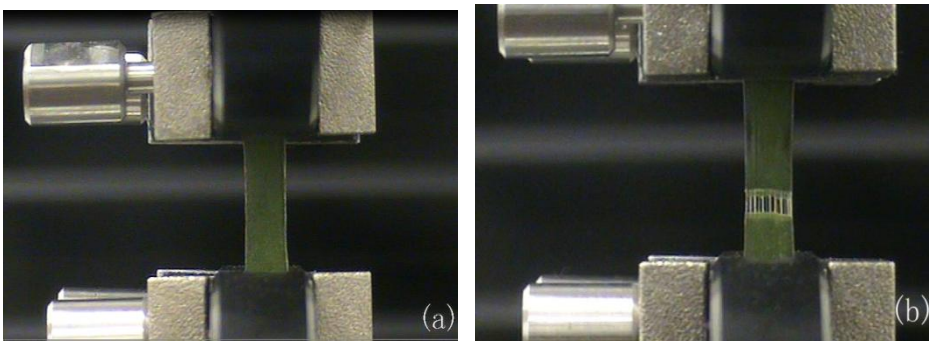

Fig. 2.17 Experimental process: (a) loading before failure; (b) failure with yield of emerging fibers.

In order to investigate the relationship between material constants and fiber orientation, we carried out ad hoc tensile tests employing a MTS micro-tensile machine. A leaf of the Aechmea aquilegia was cut into 30 specimens with dimension 30mm×3mm×0.4mm on 1st Dec 2009; fiber inclination angles vary from 0^{o} to 90^{o} with 10^{o} incremental. The whole process is displacement controlled with a loading speed 1mm/min (Fig. 2.17 (a) and (b)). All specimens were tested in indoor environment on 2nd Dec 2009. 12 days later (i.e. 14th Dec 2009), specimens were examined using SEM (Fig. 2.2).

2.6.2 Experimental results and discussion

Table 2.5 Experimental results on the leaves. (Note: the values in parenthesis represent the standard derivation.)

Angle (^{o})	0	10	20	30	40	50	60	70	80	90
Peak stress	11.3	8.9	6.8	4.8	3.2	3.7	2.0	2.6	2.8	2.1
(MPa)	(0.1)	(0.1)	(1.5)	(0.7)	(0.9)	(0.3)	(0.5)	(0.4)	(03)	(0.6)
Peak Strain	0.17	0.21	0.19	0.18	0.16	0.17	0.12	0.15	0.20	0.12
(mm/mm)	(0.00)	(0.00)	(0.03)	(0.02)	(0.05)	(0.05)	(0.04)	(0.06)	(0.01)	(0.03)
Young's modulus (MPa)	127.0 (3.5)	87.2 (7.2)	62.1 (4.4)	47.8 (4.4)	29.3 (2.2)	31.2 (3.7)	18.5 (1.9)	21.3 (3.0)	16.4 (1.9)	18.7 (0.3)

The results of peak stress (or strength), peak strain and Young's modulus are listed in Table 2.5.

The stress-strain curves are plotted in Fig. 2.18. It suggests that, generally, peak stress (or peak load) and slope of each curve (or elastic modulus) decrease as the orientation (inclination angle) increases, while, strain (elongation) increases as the orientation (inclination angle) increases. Note that for the orientation angle $\theta_F^{(2)} \geq 70^o$, the crack path is not perpendicular to the loading direction but instead parallel to the fibers.

2.6.3 Prediction of the hierarchical theory

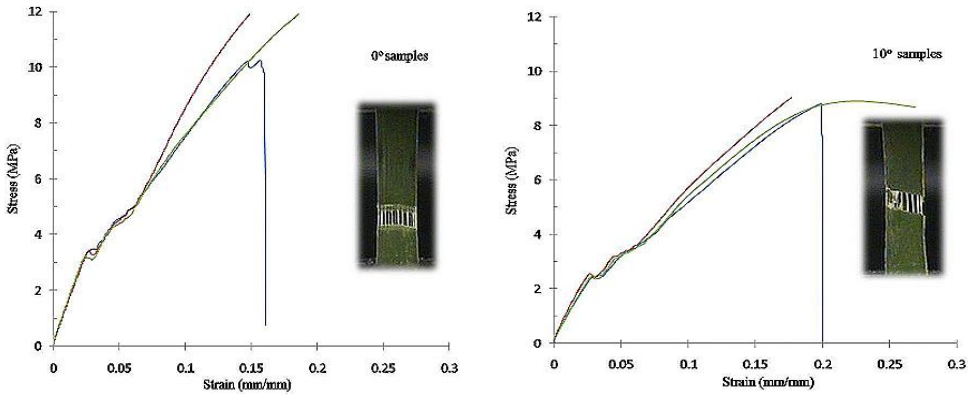

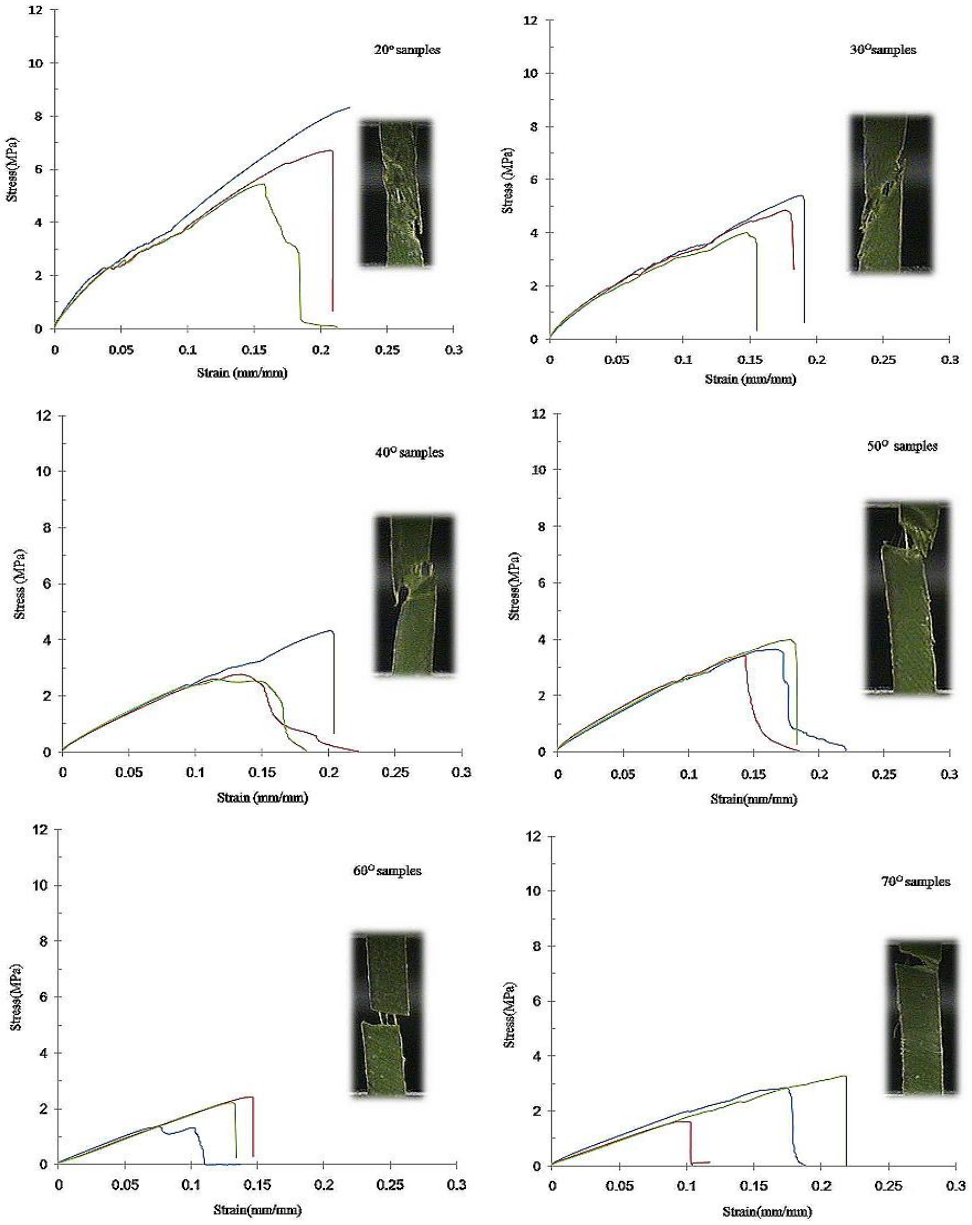
20° samples
30° samples
40° samples
50° samples
60° samples
70° samples
Stress(MPa)
Strain (mm/mm)

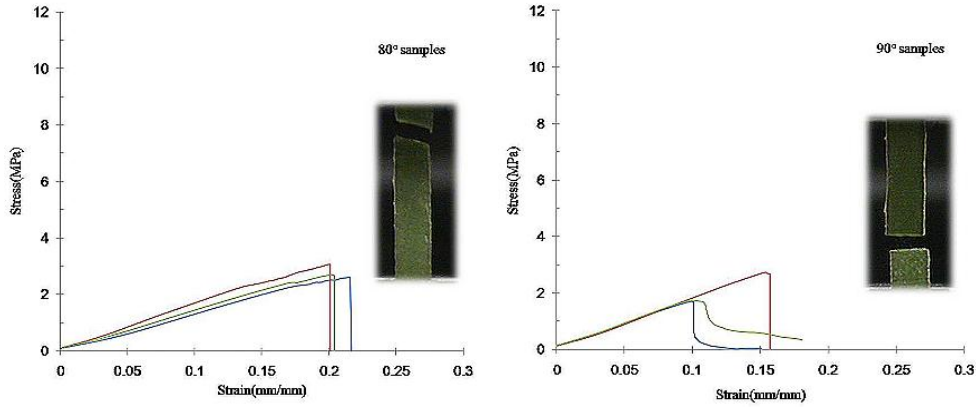

Fig. 2.18 Stress-strain curves and fracture mouths for the different tests.

The analysis is based on the orthotropic material assumption for the leaf specimens. First, the five fitting parameters listed below are obtained by the experimental data of Young's modulus in Table 2.5: $E_1 = 121.8$MPa; $E_2 = 19.3$MPa; $\mu_{12} = 0.26$; $\mu_{21} = 0.04$; $G_{12} = 10.9$MPa .

Due to the direct SEM experimental observations (Fig. 2.2) and the schematic of the crack mouths (Fig. 2.17(b)), a hierarchical model, in which A-D parts correspond to those respectively appearing in Fig. 2.2(a)-(d), is built (Fig. 2.19). The matrix is assumed to be isotropic with E=19.3 MPa and μ=0.25, thus, the shear modulus is 7.72MPa. The volumetric fraction $v_f^{(2)}$ is calculated from SEM observations, as ~26.5%. In addition, $\theta_F^{(1)}$ is assumed to be 0^o and $\theta_F^{(2)}$ depends on the specimens' inclination angle.

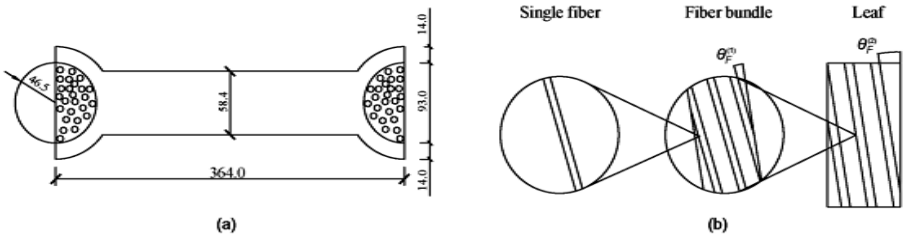

Fig. 2.19 Hierarchical model of the leaf: (a) cross-section; (b) hierarchical fibers.

Inserting values of $v_f^{(m)}$ and $\beta^{(m)}$ into Eq. (2.38), we have:

$$\begin{cases}[Q]^{(1)} = v_f^{(1)} \cdot [T(0)]^{-1}[Q]^{(0)}[T(0)] + (1 - v_f^{(1)})[Q]_M \\ [Q]^{(2)} = 0.265 v_f^{(1)} \cdot \left[T(\beta_f^{(2)})\right]^{-1}[Q]^{(0)}\left[T(\beta_f^{(2)})\right] + (1 - 0.265 v_f^{(1)})[Q]_M \end{cases}$$

where, $[Q]^{(0)}$, $[Q]^{(1)}$, $[Q]^{(2)}$ and $[Q]_M$ are elastic matrices for fiber, fiber bundle, leaf and matrix, respectively.

Table 2.6 Material constants of each hierarchical level (MPa).

	Matrix	Fiber	Fiber bundle	Leaf
(0^o)	Input	T	T	Input
E_1	19.3	449-986	406	121.8
E_2	19.3	10.4-16.0	16.5	19.3
μ_{12}	0.25	0.3-0.43	0.29	0.26
G_{12}	7.72	21.1-37.7	19.7	10.9

Herein, $v_f^{(1)}$ is selected in the range 0.4-0.9, and thus, the volumetric fraction ($v_f^{(1)} v_f^{(2)}$) is deduced in the interval 0.11-0.24. Finally, under the condition of $\beta^{(2)} = 0^o$, the material constants of the leaf and matrix are given in Table 2.6. Considering the material constants of a single fiber with $v_f^{(1)} = 0.9$, the Young's moduli of leaf for different inclination angles are compared with our theory in Fig. 2.20, again showing a relevant agreement.

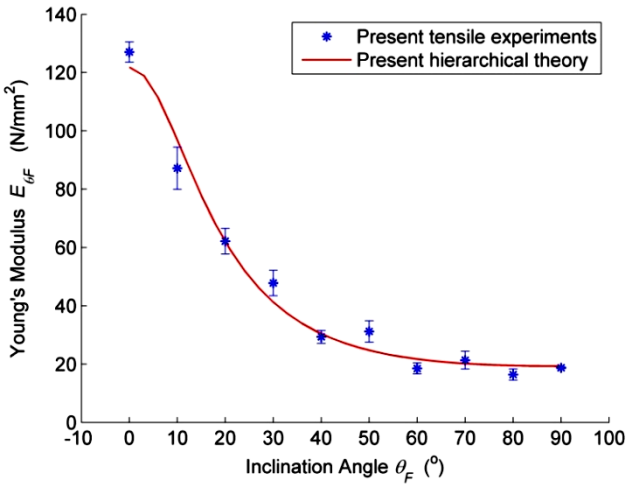

Fig. 2.20 Comparison between theoretical prediction and experimental data.

Chapter 3

Hierarchical Honeycombs: Elasticity

In this chapter, we analytically calculate the in-plane elastic properties (linear-elasticity and elastic buckling) of a new class of bio-inspired nano-honeycomb materials possessing a hierarchical architecture, which is often observed in natural materials. Incorporating the surface effect, peculiar of the nano-scale, modifications of the classical results for macroscopic and nonhierarchical honeycombs are proposed. A parametrical analysis reveals the influences of two key geometrical parameters on the overall elastic properties. We discover optimal values for the studied mechanical properties, e.g. stiffness efficiency (stiffness-to-density ratio) and strength efficiency (strength-to-density ratio), which are indices reflecting the mechanical efficiency of materials. The developed theory allows us to design a new class of materials with tailored elastic properties at each hierarchical level and could be useful for many applications.

3.1 Introduction

Honeycomb-like structure can be often found in Nature, for instance, the armadillo shell (Rhee et al., 2011), the beak of Tucan birds (Seki, et al., 2005), and the widely studied claws of lobsters (Raabe et al., 2005): the structure is low-weight but strong and tough, that is to say, it is more efficient (Karam and Gibson, 1994). In the view of biologists, it is well accepted that the structure of the natural materials is an optimized result by ambient environment in the evolutionary process (e.g. the

armadillo shell can protect internal organs from being attacked by predators). In this respect, nature seems to grant us a best solution to design more efficient materials. Therefore, inspired by nature, honeycomb materials have been extensively investigated for structural, mechanical and material design. In particular, in the field of material science, they are used as a core material in sandwich structures (Foo et al., 2007) for energy absorption (Wang, 2009; Wang et al., 2009); also, honeycomb scaffolds with mechanical stability, biocompatibility and biodegradability are used for tissue regeneration (George et al, 2008).

With such extensive applications, one of the important issues in material science is to characterize and model the in-plane and out-plane mechanical behaviors (Gibson and Ashby, 1982; Warren and Kraynik, 1987; Zhang and Ashby, 1992; Papka and Kyriakides, 1994, 1998a, 1998b) of honeycomb structures. For the in-plane and out-plane deformations, the stress-strain curves (Papka and Kyriakides, 1994, 1998a, 1998b; Gibson and Ashby, 1997) are described by three regimes (the linear elastic, pseudo plastic plateau and pseudo hyper-elastic densification regions). Gibson and Ashby (1997) summarized most of works about the structural and mechanical properties of 2D and 3D cellular solids, and systematically investigated the structure-mechanic relationship. In recent years, a variety of topological honeycombs is being studied for multifunctional applications (Wadley, 2006), e.g. the thermal conductivity properties of a rectangular-hexagonal honeycomb structure (Bezazi et al., 2008).

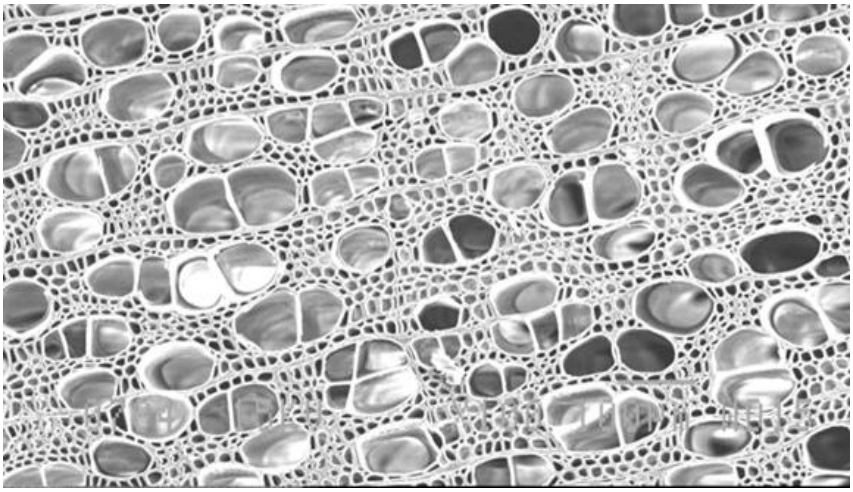

Fig. 3.1 SEM image of pure aspen wood (Cai, 2007). (Permission pending)

On the other hand, as nanoscience and nanotechnology develop, the material design also expands in nano-way. Thus, if structures are nano-sized, the surface effect should be taken into account, due to their high surface-to-volume ratio. As for the surface effect, extensive works (Wang and Feng, 2009; Shankar and King, 2007; Wong et al., 1997) studied its influence on the linear elastic behaviors of nano-wires, since nano-wires hold a promise for nano-device applications, e.g. sensors and actuators. These works show that the surface effect plays a vital role in determining the mechanical behaviors of nano-systems.

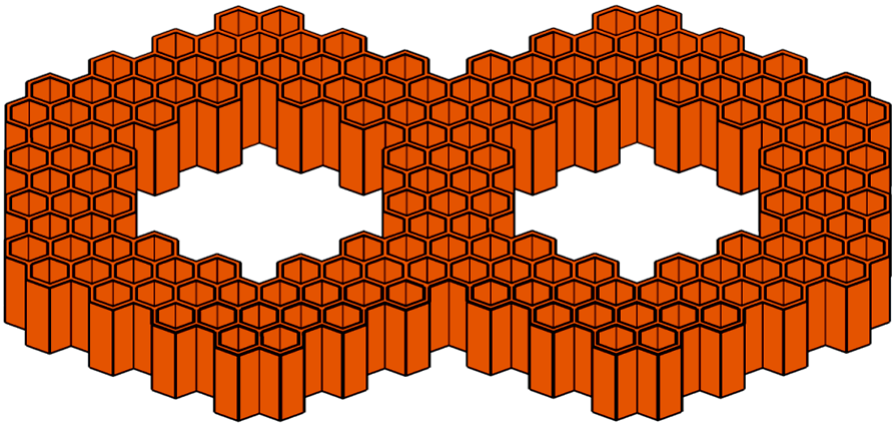

Fig. 3.2 Two-hierarchical-level nano-honeycombs.

In this Chapter, inspired by biological materials (Fig. 3.1) (Cai, 2007), we construct a hierarchical nano-honeycomb structure, using a classical iterative approach (Lakes, 1993; Pugno, 2006; Pugno, 2007; Pugno et al, 2008), and study its in-plane elastic properties (Fig. 3.2), for hierarchical structures at many length scales provide outstanding mechanical behaviors (Currey, 1977; Fratzl and Weinkamer, 2007; Yao and Gao, 2007; Tang et al., 2009). Starting from an orthotropic constituent material and considering the influence of the surface effect, we derived the effective longitudinal Young's modulus and buckling strength at the first level (Wang and Xia, 2010); then, the results of the n-level structure ($n \geq 2$) are obtained thanks to the iterative method. We also find the expressions for the stiffness- or strength-to-density ratios, which reflect materials' efficiency. Finally, we perform a parametric analysis to investigate the influences of the geometrical parameters on the overall elastic behaviors.

3.2 Surface effect

Due to the existence of surfaces in a solid, there is always a competition between bulk and surface. In particular, when the size of the solid comes down into dimensions smaller than 10nm, surface/interface effect (surface stress) becomes an important characteristic in nanostructures, and it determines their mechanical behaviors. A classical expression for the surface stress is derived based on the surface/interface energy (Cammarata, 1994), and it is composed by two parts, i.e. surface free energy and surface free energy gradient with respect to the surface strain:

$$f_{ij} = \gamma\delta_{ij} + \frac{\partial\gamma}{\partial\varepsilon_{ij}} \tag{3.1}$$

where, f_{ij} and ε_{ij} are the surface stress and strain tensors, respectively, γ is the surface free energy, δ_{ij} is the Kronecker delta.

For the elastic theory, according to Gurtin and Murdoch (1975), the surface stress τ is usually expressed as the summation of the surface residual stress and surface elasticity (i.e. the two parts corresponding to the two terms on the right-handed side of Eq. (3.1), respectively),

$$\tau = \tau^0 + S^i\varepsilon^i \tag{3.2}$$

where, τ^0 is the surface residual stress, S^i is the surface stiffness tensor, ε^i is the surface elastic strain.

Here, we only consider the influence of the surface elasticity (one-dimension), i.e. the second term on the right-handed side of Eq. (3.2).

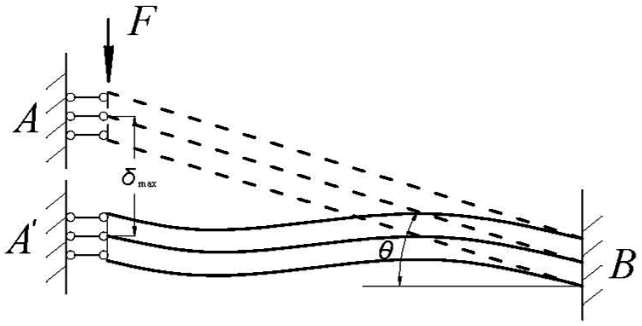

Fig. 3.3 An inclined orthotropic beam with one end guided and the other fixed.

3.3 Elastic constants of hierarchical nano-honeycombs

The linear-elastic deformation mechanism of honeycombs is mainly due to the bending of cell walls, and the standard beam theory is employed here to investigate their elastic constants.

3.3.1 Deflection of an orthotropic beam with surface effect

Assuming the conservation of plane sections, for the elastic line of an orthotropic beam with principal direction 1 coincident with the beam axis (Fig. 3.3); the classical expression for the deflection of the Euler beam is found (Tolf, 1985; Roark and Young, 1975; Gibson and Ashby 1997):

$$\delta_{\max} = \frac{Fl^3}{12E_1 I}\cos^2\theta \tag{3.3}$$

where, $\delta_{\max}$ is the vertical displacement of the guided end of the orthotropic beam, F is the concentrated force acting on the guided end, l is the beam length, $E_1 I$ is the flexural rigidity, θ is the inclined angle between beam and horizontal line.

If the beam is nano-sized, the modification induced by the surface effect should be taken into account, and we find the maximum displacement at one end of the beam as (Wang and Feng, 2009; Wang and Xia, 2010):

$$\delta_{\max} = \frac{Fl^3}{12\left(E_1 I\right)^{eq}}\cos^2\theta \quad \text{if } \tau^0=0 \tag{3.4}$$

with

$$\left(E_1 I\right)^{eq} = \frac{1}{12}E_1 bt^3 + \frac{1}{2}E_s bt^2 + \frac{1}{6}E_s t^3 \tag{3.5}$$

where, $\left(E_1 I\right)^{eq}$ is the equivalent flexural rigidity considering the surface effect; b, t are width and thickness of the beam, respectively; E_s, depending on the crystal orientation (Shenoy, 2005), is the surface Young's modulus, which has the physical dimensions of a surface tension.

We consider a one-level nano-honeycomb made by an orthotropic material (level 0) and introduce a local coordinate system $1^{(0)}2^{(0)}$ related to the global coordinate system $1^{(1)}2^{(1)}$. As shown in Fig. 3.4, the structure has two perpendicular mirror planes,

i.e., the one-level structure remains orthotropic.

The deformation is caused by the bending of beams ①, ② and the compression of beam ③ (Fig. 3.4(b)), that is the beam along which the force is applied, but the compressive deformation is neglected with respect to the bending deflection. Thus, basing on Eqs. (1)-(3) and employing the classical approach (Gibson and Ashby, 1997), we find the elastic constants of the one-level nano-honeycomb.

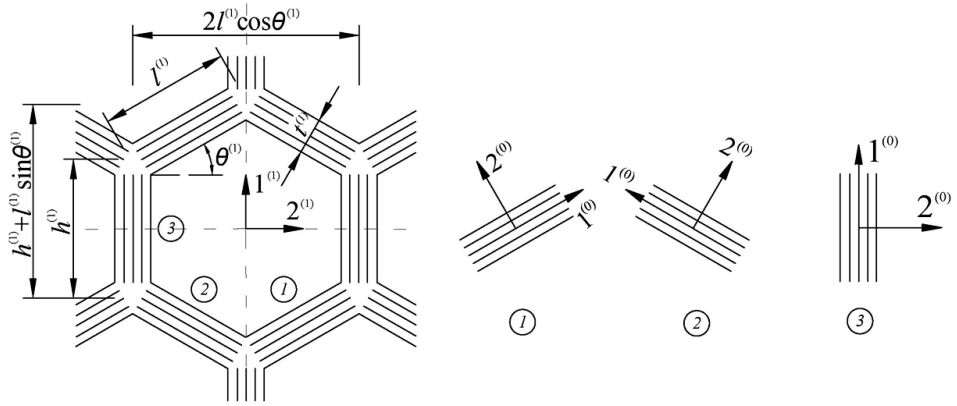

(a) (b)

Fig. 3.4 Schematic of the first-level nano-honeycomb. (a) Unit cell; (b) Three pairs of cell walls.

3.3.2 "Bottom up" method to calculate material constants

One-level structure

For the Young's moduli, we find:

$$\frac{E_1^{(1)}}{E_1^{(0)}}=\left(1+2\frac{E_s^{(0)}}{E_1^{(0)}t^{(1)}}\left(3+\frac{t^{(1)}}{b}\right)\right)\frac{(h^{(1)}/l^{(1)}+\sin\theta^{(1)})}{\cos^3\theta^{(1)}}\left(\frac{t^{(1)}}{l^{(1)}}\right)^3$$
$$\frac{E_2^{(1)}}{E_1^{(0)}}=\left(1+2\frac{E_s^{(0)}}{E_1^{(0)}t^{(1)}}\left(3+\frac{t^{(1)}}{b}\right)\right)\frac{\cos\theta^{(1)}}{(h^{(1)}/l^{(1)}+\sin\theta^{(1)})\sin^2\theta^{(1)}}\left(\frac{t^{(1)}}{l^{(1)}}\right)^3 \tag{3.6}$$

whereas the shear modulus is:

$$\frac{G_{12}^{(1)}}{E_1^{(0)}}=\left(1+2\frac{E_s^{(0)}}{E_1^{(0)}t^{(1)}}\left(3+\frac{t^{(1)}}{b}\right)\right)\frac{(h^{(1)}/l^{(1)}+\sin\theta^{(1)})}{(h^{(1)}/l^{(1)})^2(1+2h^{(1)}/l^{(1)})\cos\theta^{(1)}}\left(\frac{t^{(1)}}{l^{(1)}}\right)^3 \tag{3.7}$$

and the Poisson's ratios are:

$$\mu_{12}^{(1)} = \frac{(h^{(1)}/l^{(1)} + \sin\theta^{(1)})\sin\theta^{(1)}}{\cos^2\theta^{(1)}}$$
$$\mu_{21}^{(1)} = \frac{\cos^2\theta^{(1)}}{(h^{(1)}/l^{(1)} + \sin\theta^{(1)})\sin\theta^{(1)}} \tag{3.8}$$

where $E_1^{(0)}$ and $E_s^{(0)}$ are the bulk and surface Young's moduli in the principal direction $1^{(0)}$ (zero*th* level), respectively; b and $t^{(1)}$ are width and thickness of cross-sections of cell walls, respectively; $l^{(1)}$ and $h^{(1)}$ are lengths of beams ① and ③, respectively; $\theta^{(1)}$ is the included angle made by beam ① and horizontal line (Fig. 3.4).

From Eqs. (3.6)-(3.8), we note that the two Poisson's ratios are the same as those derived by Gibson and Ashby, whereas, the Young's moduli and shear modulus are modified by a factor λ_s:

$$\lambda_s^{(1)} = 1 + 2\frac{E_s^{(0)}}{E_1^{(0)}t^{(1)}}\left(3 + \frac{t^{(1)}}{b}\right) \tag{3.9}$$

if $t_1^{(1)}/b$ much less than unity (i.e. plate), Eq. (3.9) can be expressed as:

$$\lambda_s^{(1)} = 1 + 6\frac{E_s^{(0)}}{E_1^{(0)}t^{(1)}} \tag{3.10}$$

Expression (3.10) coincides with the result from Miller and Shenoy (2000), and it obeys the scaling law $\lambda_s^{(1)} = 1 + \alpha l_{\text{in}}/t^{(1)}$ (Wang et al, 2006) with $l_{\text{in}} = E_s^{(0)}/E_1^{(0)}$ and $\alpha = 6.0$. Note that l_{in} represents an intrinsic material length, under which surface effect plays an important role; α is a dimensionless constant, which depends on the geometry of the structural element and its deformation. Besides, we can see that the surface effect at level zero makes the structure stiffer if $E_s^{(0)} > 0$; otherwise, it makes the structure softer.

Moreover, the geometry of Fig. 3.4 gives the relative density:

$$\frac{\rho^{(1)}}{\rho^{(0)}} = \frac{(h^{(1)}/l^{(1)} + 2)}{2\cos\theta^{(1)}(h^{(1)}/l^{(1)} + \sin\theta^{(1)})}\frac{t^{(1)}}{l^{(1)}} \tag{3.11}$$

where, $\rho^{(1)}$ or $\rho^{(0)}$ is the one-level structure's density or constituent material's density, respectively.

Now, we define the following four functions with respect to $h^{(1)}/l^{(1)}$ and $\theta^{(1)}$:

$$
\begin{aligned}
f_1^{(1)} &= \frac{(h^{(1)}/l^{(1)} + \sin\theta^{(1)})}{\cos^3\theta^{(1)}} \\
f_2^{(1)} &= \frac{\cos\theta^{(1)}}{(h^{(1)}/l^{(1)} + \sin\theta^{(1)})\sin^2\theta^{(1)}} \\
f_3^{(1)} &= \frac{(h^{(1)}/l^{(1)} + \sin\theta^{(1)})}{(h^{(1)}/l^{(1)})^2(1+2h^{(1)}/l^{(1)})\cos\theta^{(1)}} \\
f_4^{(1)} &= \left(\frac{2\cos\theta^{(1)}(h^{(1)}/l^{(1)} + \sin\theta^{(1)})}{(h^{(1)}/l^{(1)} + 2)}\right)^3
\end{aligned}
\tag{3.12}
$$

with these definitions, Eqs. (3.6)-(3.8) are concisely expressed as:

$$
\frac{E_1^{(1)}}{E_1^{(0)}} = \lambda_s^{(1)} f_1^{(1)} f_4^{(1)} \left(\frac{\rho^{(1)}}{\rho^{(0)}}\right)^3 \tag{3.13}
$$

$$
\begin{aligned}
\frac{E_2^{(1)}}{E_1^{(0)}} &= \frac{f_2^{(1)}}{f_1^{(1)}} \cdot \frac{E_1^{(1)}}{E_1^{(0)}} \\
\frac{G_{12}^{(1)}}{E_1^{(0)}} &= \frac{f_3^{(1)}}{f_1^{(1)}} \cdot \frac{E_1^{(1)}}{E_1^{(0)}}
\end{aligned}
\tag{3.14}
$$

$$
\mu_{12}^{(1)} = \left(\frac{f_1^{(1)}}{f_2^{(1)}}\right)^{0.5} = \frac{1}{\mu_{21}^{(1)}} \tag{3.15}
$$

Two-level structure

Compared with the one-level structure, the cell-wall dimensions at the second level of the two-level structure are very large, so that the surface effect could be neglected, i.e. $E_s^{(1)} = 0$. However, in order to extend the theory to the general case, we still consider the surface effect at the second level and find:

$$
\frac{E_1^{(2)}}{E_1^{(0)}} = \left(\lambda_s^{(1)}\lambda_s^{(2)}\right)\left(f_1^{(1)} f_1^{(2)}\right)\left(f_4^{(1)} f_4^{(2)}\right)\left(\frac{\rho^{(2)}}{\rho^{(0)}}\right)^3 \tag{3.16}
$$

$$
\begin{aligned}
\frac{E_2^{(2)}}{E_1^{(0)}} &= \frac{f_2^{(2)}}{f_1^{(2)}} \cdot \frac{E_1^{(2)}}{E_1^{(0)}} \\
\frac{G_{12}^{(2)}}{E_1^{(0)}} &= \frac{f_3^{(2)}}{f_1^{(2)}} \cdot \frac{E_1^{(2)}}{E_1^{(0)}}
\end{aligned}
\tag{3.17}
$$

$$
\mu_{12}^{(2)} = \left(\frac{f_1^{(2)}}{f_2^{(2)}}\right)^{0.5} = \frac{1}{\mu_{21}^{(2)}} \tag{3.18}
$$

where, $f_1^{(2)}$, $f_2^{(2)}$, $f_3^{(2)}$ and $f_4^{(2)}$ can be obtained by replacing the superscript (1) with

(2) in Eq. (3.12).

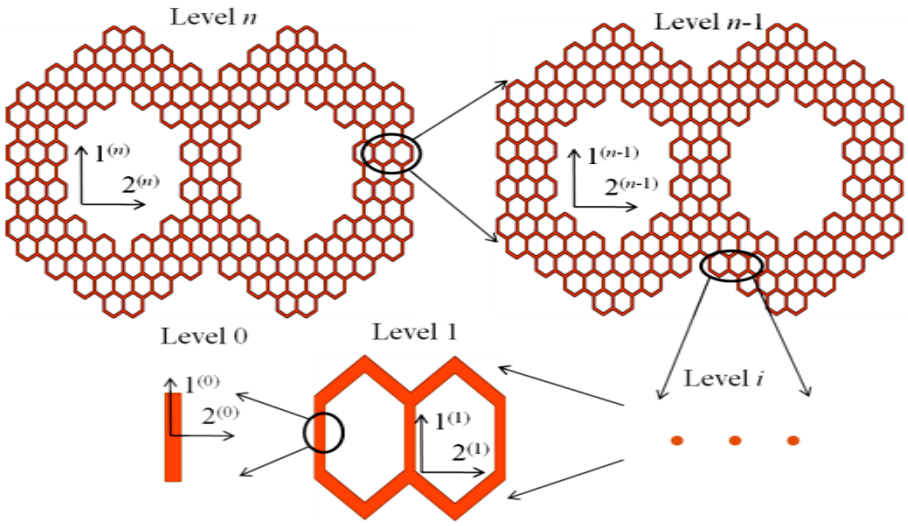

Fig. 3.5 Front view of the n-level nano-honeycomb.

n-level structure

Fig. 3.5 describes an *n*-level nano-honeycomb. The structure at level *n* is constructed based on the structure at level *n*-1 and the dimensionless ratio of the Young's moduli at level *n* and level *n*-1 is obtained by implementing the procedure of the two-level structure and the same for the levels from 3 to *n*-1. Then, considering the surface effect at all levels, we easily find:

$$\frac{E_1^{(n)}}{E_1^{(0)}} = \prod_{i=1}^{n} \lambda_s^{(i)} f_1^{(i)} f_4^{(i)} \cdot \left(\frac{\rho^{(n)}}{\rho^{(0)}} \right)^3 \tag{3.19}$$

$$\begin{aligned} \frac{E_2^{(n)}}{E_1^{(0)}} &= \frac{f_2^{(n)}}{f_1^{(n)}} \cdot \frac{E_1^{(n)}}{E_1^{(0)}} \\ \frac{G_{12}^{(n)}}{E_1^{(0)}} &= \frac{f_3^{(n)}}{f_1^{(n)}} \cdot \frac{E_1^{(n)}}{E_1^{(0)}} \end{aligned} \tag{3.20}$$

$$\mu_{12}^{(n)} = \left(\frac{f_1^{(n)}}{f_2^{(n)}} \right)^{0.5} = \frac{1}{\mu_{21}^{(n)}} \tag{3.21}$$

where, $f_1^{(n)}$, $f_2^{(n)}$, $f_3^{(n)}$ and $f_4^{(n)}$ can be obtained by replacing the superscript (1) with (*n*) in Eq. (3.12).

Note that, the reciprocal theorem holds:

$$E_1^{(n)}\mu_{21}^{(n)} = E_2^{(n)}\mu_{12}^{(n)} \tag{3.22}$$

Eqs. (3.19)-(3.21), show that the transverse Young's modulus and shear modulus can be derived from the longitudinal Young's modulus, and the two Poisson's ratios are only related to the geometry of the *n*-level structure. Therefore, in essential, there are only two independent elastic constants, i.e. the longitudinal Young's modulus and one of the Poisson's ratios.

3.3.3 Stiffness efficiency

Structural efficiency bases on the minimum-weight analysis, and it is used to optimize the structural design and thus, reduce cost. By considering the maximum stress and maximum strain, Budiansky (1999) investigated several types of compressive structures which are hollow tubes with foam and without foam filled. Wegst and Ashby (2004) studied the mechanical efficiency of natural ceramics, natural polymers, natural elastomers, natural cellular materials under tensile and flexural loads and plotted so-called "Ashby map" according to different material indices. Here, considering the mechanical efficiency of honeycomb materials, we study the stiffness-to-density ratio for a light but stiff structure. Ashby (2010) provides us a material index to evaluate the stiffness efficiency for a uniaxial loaded structure, the stiff tie is $P_{s1}=E/\rho$. For the hierarchical honeycomb structures, $E_1^{(n)}/\rho^{(n)}$ can be derived Eqs. (3.19) and (3.20), i.e:

$$\frac{E_1^{(n)}}{\rho^{(n)}} = \frac{E_1^{(0)}}{\rho^{(0)}}\prod_{i=1}^{n}\lambda_s^{(i)} f_1^{(i)} f_4^{(i)} \cdot \left(\frac{\rho^{(n)}}{\rho^{(0)}}\right)^2 \tag{3.23}$$

$$\begin{aligned} \frac{E_2^{(n)}}{\rho^{(n)}} &= \frac{f_2^{(n)}}{f_1^{(n)}} \cdot \frac{E_1^{(n)}}{\rho^{(0)}} \\ \frac{G_{12}^{(n)}}{\rho^{(n)}} &= \frac{f_3^{(n)}}{f_1^{(n)}} \cdot \frac{E_1^{(n)}}{\rho^{(0)}} \end{aligned} \tag{3.24}$$

3.4 Elastic buckling of hierarchical honeycomb materials

Different from the linear elastic behavior of honeycombs, progressive buckling deformation of cell walls is the main energy-absorbing mechanism. Therefore, it is significant to study the buckling behavior and impact effect of the hierarchical honeycomb in the design of energy-absorbing materials.

3.4.1 Buckling load of the orthotropic beam with surface effect

Euler buckling equation is a simple and efficient way to describe the buckling behavior for an isotropic beam or column. For an orthotropic nano-column, due to the standard beam theory (i.e. Euler beam therory) and the surface effect, the buckling load F_{cr} is obtained (Tolf, 1985; Timoshenko and Gere, 1961):

$$F_{cr} = \frac{n^2 \pi^2 \left(E_1 I\right)^{eq}}{l^2} \tag{3.25}$$

where, n is a numerical factor depending on the boundary conditions. Eq. (3.25) is the classical Euler buckling formula with surface effect, in which the Young's modulus of the isotropic material is substituted by the longitudinal one of the orthotropic beam.

3.4.2 "Bottom up" method to calculate buckling loads with surface effect

One-level structure

For the one-level structure (Fig. 3.4), when the external stress s applies on the structure (Fig. 3.1), the equivalent concentrated force acting on beam ③ is:

$$F^{(1)} = 2sb^{(1)}l^{(1)}\cos\theta^{(1)} \tag{3.26}$$

If the beam buckles, the force F should reach the critical load F_{cr}. Substituting Eq. (3.26) into Eq. (3.25), we find:

$$\frac{s_{cr}^{(1)}}{E_1^{(0)}} = \lambda_s^{(1)} \frac{(\pi n^{(1)})^2}{24} \left(\frac{t^{(1)}}{l^{(1)}}\right)^3 \left(\frac{l^{(1)}}{h^{(1)}}\right)^2 \frac{1}{\cos\theta^{(1)}} \tag{3.27}$$

Here, we define a new function with respect to $h^{(1)}/l^{(1)}$ and $\theta^{(1)}$:

$$f_5^{(1)} = \frac{(\pi n^{(1)})^2}{24} \left(\frac{l^{(1)}}{h^{(1)}}\right)^2 \frac{1}{\cos\theta^{(1)}} \tag{3.28}$$

where, $n^{(1)}$ is related to $h^{(1)}/l^{(1)}$.

So, Eq. (3.27) is concisely written as:

$$\frac{s_{cr}^{(1)}}{E_1^{(0)}} = \lambda_s^{(1)} f_4^{(1)} f_5^{(1)} \left(\frac{\rho^{(1)}}{\rho^{(0)}} \right)^3 \tag{3.29}$$

Two-level structure

For the two-level structure, we have two objects in the analysis, the vertical beams at the first and the second level. On one hand, the equivalent concentrated force acting on the beam at the second level is:

$$F^{(2)} = 2sb^{(2)} l^{(2)} \cos\theta^{(2)} \tag{3.30}$$

Like in the linear-elastic analysis (one could neglect the surface effect because of the larger size), we find the buckling load for the beam:

$$\frac{s^{(2)}}{E_1^{(1)}} = \lambda_s^{(2)} f_4^{(2)} f_5^{(2)} \left(\frac{\rho^{(2)}}{\rho^{(1)}} \right)^3 \tag{3.31}$$

$E_1^{(1)}$ is calculated by Eq. (3.13), then we find the final result:

$$\frac{s^{(2)}}{E_1^{(0)}} = \left(\lambda_s^{(1)} \lambda_s^{(2)} \right) \left(f_1^{(1)} f_4^{(1)} \right) \left(f_4^{(2)} f_5^{(2)} \right) \left(\frac{\rho^{(2)}}{\rho^{(0)}} \right)^3 \tag{3.32}$$

On the other hand, based on load transfer and the equivalent concentrated force acting on the beam at the second level, the equivalent concentrated force acting on the beam at the first level should be calculated, which is expressed as:

$$F^{(1)} = 2\left(2s \frac{l^{(2)}}{t^{(2)}} \cos\theta^{(2)} \right) b^{(1)} l^{(1)} \cos\theta^{(1)} \tag{3.33}$$

then, substituting the force into the buckling Eq. (3.25), the buckling stress can be obtained easily, i.e.

$$\frac{s^{(1)}}{E_1^{(0)}} = \lambda_s^{(1)} f_6^{(2)} \left(f_4^{(1)} f_5^{(1)} \right) \left(\frac{\rho^{(1)}}{\rho^{(0)}} \right)^2 \left(\frac{\rho^{(2)}}{\rho^{(0)}} \right) \tag{3.34}$$

with

$$f_6^{(2)} = \frac{(h^{(2)} / l^{(2)} + \sin\theta^{(2)})}{(h^{(2)} / l^{(2)} + 2)} \tag{3.35}$$

Finally, the buckling load is obtained as:

$$s_{cr}^{(2)} = \min(s^{(2)}, s^{(1)}) \tag{3.36}$$

n-level structure

Like the analysis of the two-level structure, finding the concentrated force acting on the beam at level *i* and substituting the force into buckling equation, The

dimensionless buckling load at every level is obtained as:

$$\frac{s^{(i)}}{E_1^{(0)}} = \prod_{j=i+1}^{n} f_6^{(j)} \cdot \prod_{k=1}^{i-1}\left(\lambda_s^{(k)} f_1^{(k)} f_4^{(k)}\right)\cdot\left(f_4^{(i)} f_5^{(i)}\right)\left(\frac{\rho^{(i)}}{\rho^{(0)}}\right)^2\left(\frac{\rho^{(n)}}{\rho^{(0)}}\right) \tag{3.37}$$

so, the buckling load of the *n*-level structure is obtained:

$$s_{cr}^{(n)} = \min(s^{(i)}) \tag{3.38}$$

3.4.3 Strength efficiency

Like stiffness efficiency, the strength efficiency of the hierarchical structure is deduced here. And a strong tie for uniaxial loading structure is expressed as P_{s2}=s/ρ. From Eq. (3.37), the evaluating criterion, i.e. buckling load to density, is obtained as:

$$\frac{s^{(i)}}{\rho^{(n)}} = \prod_{j=i+1}^{n} f_6^{(j)} \cdot \prod_{k=1}^{i-1}\left(\lambda_s^{(k)} f_1^{(k)} f_4^{(k)}\right)\cdot\left(f_4^{(i)} f_5^{(i)}\right)\left(\frac{\rho^{(i)}}{\rho^{(0)}}\right)^2\left(\frac{E_1^{(0)}}{\rho^{(0)}}\right) \tag{3.39}$$

thus, the buckling strength to density is obtained as:

$$\frac{s_{cr}^{(n)}}{\rho^{(n)}} = \frac{\min(s^{(i)})}{\rho^{(n)}} \tag{3.40}$$

3.5 Parametric analysis and discussion

Here, we consider silver (Ag) as the constituent material, for treating a five-level hierarchical nano-honeycomb structure and only consider the surface effect on the first level, because of the much smaller scale compared to that of level 2. The Young's modulus and density of Ag are 78GPa and 10.94g/cm^3, respectively; the surface elastic modulus on the surface A of (001) orientation is $E_s = 1.22\text{N/m}$ (Wang and Feng, 2009); the thickness of the cell walls at the first level is assumed to be $t^{(1)} = 5\text{nm}$.

3.5.1 Linear-elastic analysis

As we discussed in Section 3.3, all the elastic constants depend on the longitudinal Young's modulus, thus, $E_1^{(n)}$ is here analyzed. We consider quasi-self-similar cases, i.e., the relative density $\rho^{(i+1)}/\rho^{(i)} = 0.3$ and when we investigate the influence of $h^{(i)}/l^{(i)} = h/l$ (or $\theta^{(i)} = \theta$), we assume $\theta^{(i)} = 70 - 10i$ (or $h^{(i)}/l^{(i)} = 3.5 - 0.5i$) at each

level. The analytic results of the longitudinal Young's modulus and the stiffness-to-density ratio are reported in Fig. 3.6. It shows that the longitudinal Young's modulus increases as $h^{(i)}/l^{(i)}$ or $\theta^{(i)}$ increase, but decreases as level *i* increases (Figs. 3.6(a) and (b)); in contrast, the stiffness-to-density ratio has a maximum value at level 3 when varying $h^{(i)}/l^{(i)}$; it means the structural stiffness is most efficient at level 3 and almost constant as level *i* increases (Fig, 3.6(c)). Fig. 3.6(d) implies that, if we increase the value of $\theta^{(i)}$, we can also have a maximum and find an optimal structure.

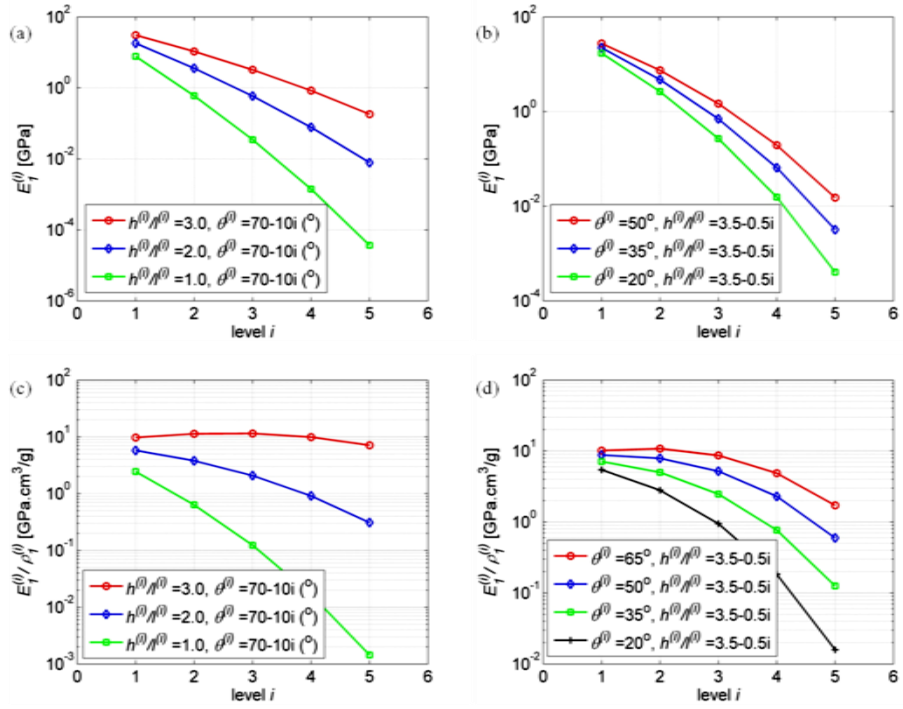

Fig. 3.6 (a) Influence of $h^{(i)}/l^{(i)}$ on longitudinal Young's modulus; (b) Influence of $\theta^{(i)}$ on longitudinal Young's modulus; (c) Influence of $h^{(i)}/l^{(i)}$ on stiffness-to-density ratio; (d) Influence of $\theta^{(i)}$ on stiffness-to-density ratio.

3.5.2 Buckling analysis

In this case, the method is the same as that described above. The analytic results of the buckling strength and strength-to-density ratio are reported in Fig. 3.7. It shows that the variations with respect to $\theta^{(i)}$ or $h^{(i)}/l^{(i)}$ make the strength and strength-to-density

ratio maximal. For both cases, they are optimized when $\theta = 30^{o}$ and $h/l = 1.25 \sim 1.5$; while the control to h/l produce a stronger structure and is more efficient compared to the control to θ.

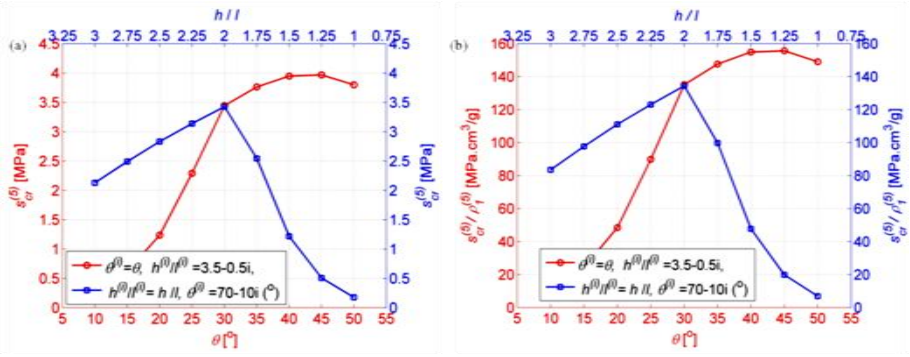

Fig. 3.7 (a) Parametric analysis on buckling strength; (b) Parametric analysis on strength-to-density ratio

3.5.3 Discussion

Fig. 3.6 and Fig. 3.7 indicate that the mechanical behavior can be tuned by changing the geometrical configuration. Increasing $\theta^{(i)}$ or $h^{(i)}/l^{(i)}$, the Young's modulus increases. If $\theta^{(i)}$ (or $h^{(i)}/l^{(i)}$) increases, while $h^{(i)}/l^{(i)}$ (or $\theta^{(i)}$) decreases, then, the two variations of $\theta^{(i)}$ or $h^{(i)}/l^{(i)}$ result in an inverse tendency (i.e.: the former makes the structure stiffer; whereas the latter makes it softer) about the elastic parameters, so, there exist optimal values (Fig. 3.6 (c) and Fig. 3.7). This is interesting for designing optimized and stiffness/strength efficient hierarchical nano-honeycombs. It is worth to say that the honeycomb skeleton is only treated here compared to natural materials, which are usually composites; then, if a matrix is considered, then, an optimal hierarchy with maximum toughness could be obtained (Zhang et al., 2011)

.

Chapter 4

Hierarchical Honeycomb: Elastic Buckling

In this chapter, we study the elastic buckling of a new class of honeycomb materials with hierarchical architecture, which is often observed in nature. Employed the top-down approach, the virtual buckling stresses and corresponding strains for each cell wall at level n-1 are calculated based on those at level n, then, comparing these virtual buckling stresses of all cell walls, the real local buckling stress is deduced; also, the progressive failure of the hierarchical structure is studied. Finally, parametric analyses reveal influences of some key parameters on the local buckling stress and strength efficiency (i.e. strength-to-density ratio); meanwhile the constitutive behaviors and energy-absorption properties with increasing hierarchy n are reported. The results show a possibility to tailor the functionality grade materials with different elastic buckling properties at each hierarchical level, and thus could have interesting applications, e.g. to design multiscale energy-absorption honeycomb materials.

4.1 Introduction

Honeycomb cellular materials are widely discovered in biological materials, such as, the turtle shell (Krauss et al., 2009), the lobster's exoskeleton (Fabritius et al., 2009), and they are very promising for structural, mechanical and material design (Gibson et al., 1982; Warren and Kraynik, 1987; Papka and Kyriakides, 1994, 1998a; Gibson and Ashby, 1997) due to their fascinating material properties (e.g. low weight, high

toughness). For example, in the field of material science, it is used to be a core material in sandwich structures (Foo et al., 2007), which could be used in aerospace engineering (Zakeri and Mazraehshahi, 2010); also, it is used as energy-absorbing material to reduce loading impact and protect an object from crushing (Xue and Hutchinson, 2006).

On one hand, many pioneering works focused on its in-plane and out-plane mechanical behaviors (e.g. elastic buckling) (Papka and Kyriakides, 1998b; Zhang and Ashby, 1992). In particular, Papka and Kyriakides (1994) explained the crushing process of uni-axial compression in detail, and generally, the collapse of the honeycomb is characterized by three regimes: At the initial loading stage, the material has a relatively high stiffness, the deformation is caused by the bending of cell walls and it is linear-elastic and stable; as load increases, honeycombs collapse locally in a progressive but metastable way when a critical stress is reached; finally, the whole structure collapses during densification, and its stiffness increases and deformation is uniform and very stable. The three stages are shown in Fig. 4.1, in which our observations on a natural honeycomb and Scanning Electron Microscopic (SEM) images of the cell-wall constituent materials are reported.

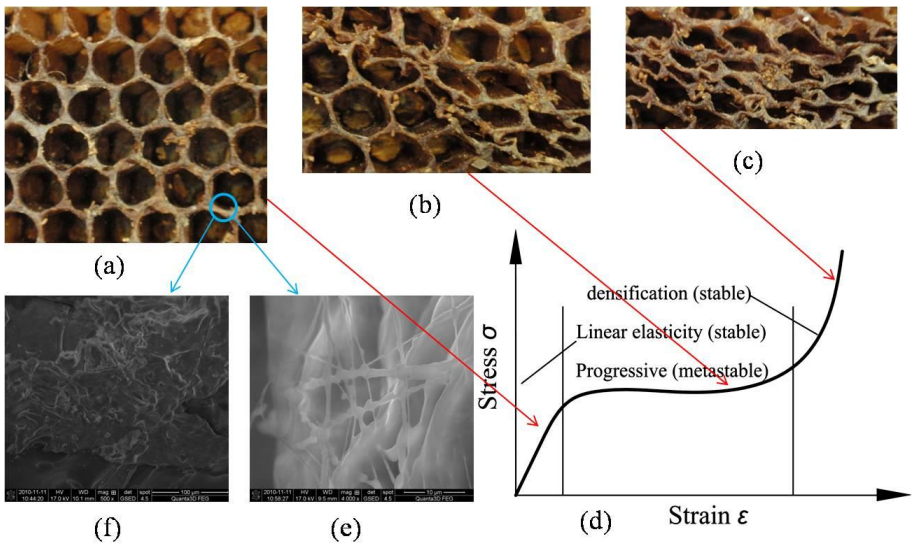

Fig. 4.1 Natural honeycomb crushing process: (a) linear-elastic stable phase; (b) progressive metastable phase; (c) densification very stable phase; (d) schematic of a honeycomb stress-strain curve; (e) silk (inclusion); (f) wax grain (matrix).

On the other hand, Nature creates composite structures in hierarchical way, from nanoscale to macroscale (Launey and Ritchie, 2009); the structures/materials at nanoscale and microscale exhibit highly anisotropy (Ritchie et al., 2009; Yao et al., 2011); in bioshells, they exhibit structural gradient (so-called functionality grade materials), for instance, the exoskeleton of lobsters has three different layers from exterior to interior, with decreasing densities, strength and hardness (Raabe et al., 2009). Honeycomb structure enable these biological materials to exhibit outstanding mechanical properties, e.g. low weight, high stiffness, strength, and toughness (Smith et al., 2009; Munch et al., 2008). For this reason, bio-inspired material is becoming of great interest for both hierarchical science and technology. Recently, Munch et al. (2008) synthesized a tough bio-inspired hybrid material basing on aluminum oxide and polymethyl methacrylate, and the toughness of the product is more than 300 times higher than those of constituent materials. The synthesized structure is lamellar and similar to that of nacre, which has two hierarchical levels. Theoretically, Gao and co-workers (2006) brought a tensile-shear chain model forward to investigate the hierarchical mechanical properties of bone and bone-like materials, basing on the principle of flow tolerance; and they showed the hierarchy of load-bearing biological materials is dominated by the toughness optimization (Zhang et al., 2011).

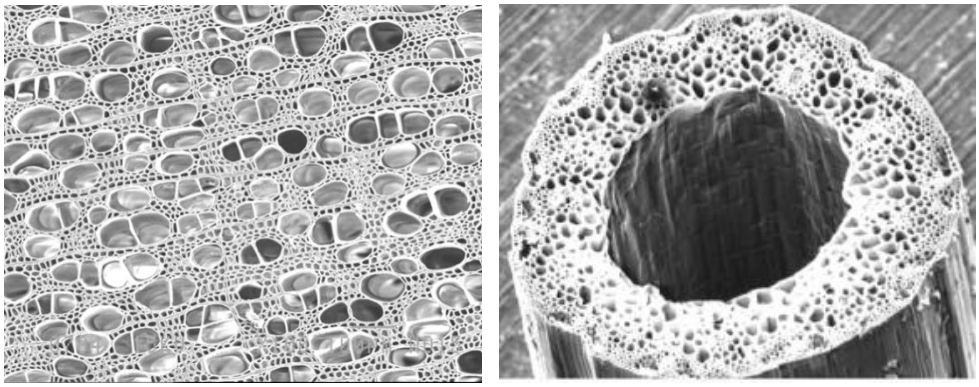

(a) (b)

Fig. 4.2 SEM image of pure aspen wood: (a) aspen wood (Cai, 2007); (b) grassy stem (Gibson, 2005). (Permission pending)

Combining the honeycomb structure with hierarchy, Côté et al. (2009) studied the out-of-plane compressive properties of a hierarchical square honeycomb sandwich core and found that the hierarchical topology increase the mechanical performance; Taylor

et al. (2011) introduced hierarchy into honeycomb structures and considered different super- or sub-structures, then, the elastic properties of the hierarchical structure were studied, interestingly, they found that the negative Poisson's ratio substructure increased its relative density substantially; also, Sen et al. (2011) studied the size-dependent mechanical properties of a nanosized honeycomb silica structure.

In this chapter, inspired by the hierarchical structure of natural materials (Fig. 4.2) (Cai, 2007; Gibson, 2005) and starting from an orthotropic material, a new hierarchical honeycomb material is constructed using a hierarchical approach (Pugno, 2006; Pugno et al., 2008; Chen and Pugno, 2011; Pugno and Carpinteri, 2008), see Fig. 4.3 (Chen et al., 2011). Extending the Euler critical load of isotropic to orthotropic columns by pure bending beam theory, the local buckling stress of the hierarchical honeycomb material is formulated due to the significance in the energy-absorbing mechanism. Besides, we perform a parametric analysis to investigate the influences of relevant parameters on local buckling loads, strength efficiency (i.e. strength-to-density ratio) and virtual progressive failure behavior. The results show that there is a possibility to design energy absorption materials with multiscale geometrical and multi-plateau buckling properties.

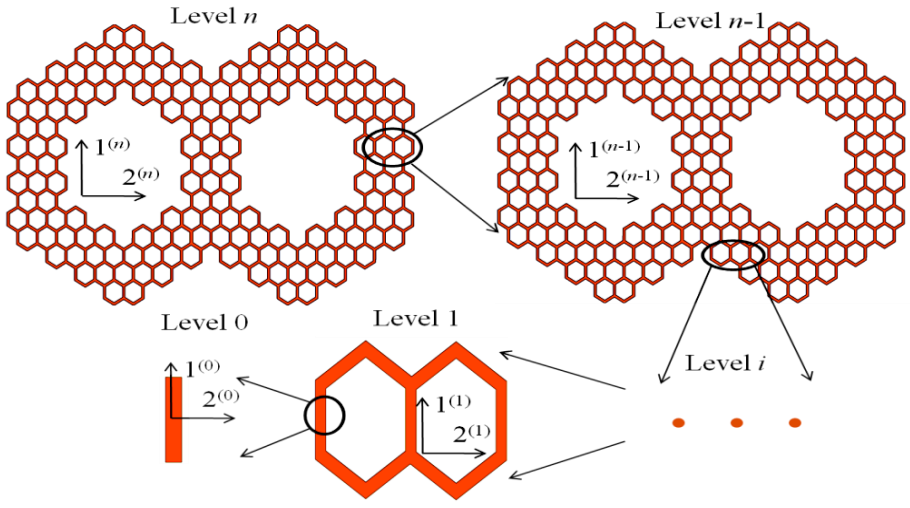

Fig. 4.3 Hierarchical honeycombs.

4.2 Elastic buckling of hierarchical honeycomb

4.2.1 Euler buckling formula for orthotropic beams/columns

Here, cell walls are treated as columns, as done in the classical theory about non-hierarchical honeycomb (Gibson and Ashby, 1997). For an orthotropic column, assuming the conservation of the plane sections and neglecting the shear effect, the buckling load P_{cr} becomes (Timoshenko and Gere, 1961; Tolf, 1985):

$$P_{cr} = \frac{\lambda^2 \pi^2 E_1 I}{l^2} \tag{4.1}$$

where, l is the length of the column, λ is a numerical factor depending on the boundary conditions, E_1 is the Young's modulus in the longitudinal direction of the column and $E_1 I$ is the bending rigidity. Eq. (4.1) is the classical Euler buckling formula, in which the Young's modulus of an isotropic material is substituted by the longitudinal one of the orthotropic column.

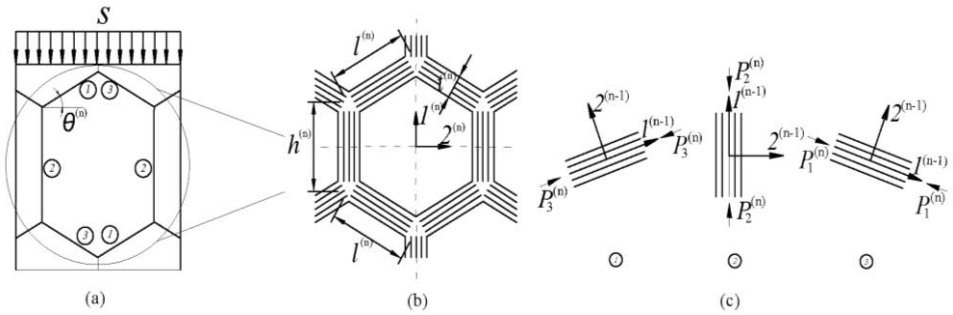

Fig. 4.4 Schematic of n^{th} level hierarchical honeycombs.

4.2.2 "Top down" method to calculate buckling loads

The n^{th} level

We treat the structure in Fig. 4.4a as the n^{th} level structure and each cell wall as the $(n\text{-}1)^{th}$ level structure; the structures at each level are approximated as orthotropic due to the symmetric configuration. In order to determine its buckling load at level n, we

need to calculate the applied loads acting on the six cell walls; then, employing Eq. (4.1), we can find the buckling loads for each column. Actually, three pairs are of our interest, i.e., ①, ②, ③ (Fig. 4.4); moreover, only two of them (pair ①, ②) are treated because of the symmetry. For the sake of the simplicity, the cell walls ① are treated as inclined columns and the buckling loads of the pairs ①, ② are expressed as (Chang, 2005; Gibson et al., 1982):

$$P_1^{(n)} = \frac{P}{2\sin\theta^{(n)}} \qquad P_2^{(n)} = P \tag{4.2}$$

with

$$P = 2sb^{(n)}l^{(n)}\cos\theta^{(n)} \tag{4.3}$$

where, s is the external stress; $b^{(n)}$, $l^{(n)}$ and $\theta^{(n)}$ are, respectively, the depth of the structure, the length of column ①and the angle made by column ① and the horizontal line at level n.

(a) Buckling stress analysis

According to Eqs. (4.2) and (4.3), the axial loads acting on the two beams are expressed as $\overrightarrow{P^{(n)}} = \left(P_1^{(n)}, P_2^{(n)}\right)^T$ with:

$$P_1^{(n)} = sb^{(n)}l^{(n)}\cot\theta^{(n)} \qquad P_2^{(n)} = 2sb^{(n)}l^{(n)}\cos\theta^{(n)} \tag{4.4}$$

Elastic collapse occurs when one of the components in the force vector $\overrightarrow{P^{(n)}}$ reaches the corresponding one in the critical force vector $\overrightarrow{P_{cr}^{(n)}} = \left(P_{cr,1}^{(n)}, P_{cr,2}^{(n)}\right)^T$, Namely:

$$\overrightarrow{P^{(n)}} = \overrightarrow{P_{cr}^{(n)}} \tag{4.5}$$

combining Eqs. (4.1), (4.4) and (4.5), we find the external critical stress vector $\overrightarrow{s_{cr}^{(n)}} = \left(s_{cr,1}^{(n)}, s_{cr,2}^{(n)}\right)^T$:

$$s_{cr,1}^{(n)} = \frac{\pi^2\left(\lambda_1^{(n)}\right)^2 E_1^{(n-1)}}{12}\left(\frac{t^{(n)}}{l^{(n)}}\right)^3\tan\theta^{(n)}$$
$$s_{cr,2}^{(n)} = \frac{\pi^2\left(\lambda_2^{(n)}\right)^2 E_1^{(n-1)}}{24}\left(\frac{t^{(n)}}{h^{(n)}}\right)^2\left(\frac{t^{(n)}}{l^{(n)}}\right)\sec\theta^{(n)} \tag{4.6}$$

where, $h^{(n)}$ is the length of column ②. For $\lambda_1^{(n)}$ and $\lambda_2^{(n)}$, we calculated as below:

the inclined cell wall is treated with a column with one end clamped and the other guided (Gibson and Ashby, 1997). According the reference (Chang, 2005), $\lambda_1^{(n)}$, for the sake of simplicity, is considered as a constant and equal to 8.669, because it has a minor change when θ varies in the range 15°~75°; β=8.669 is conservative, compared with 8.986 when θ=15°. For the vertical cell wall, we use the formula (Gibson and Ashby, 1997) $\lambda_2^{(n)} \tan \lambda_2^{(n)} = 2h^{(n)}/l^{(n)}$ to calculated $\lambda_2^{(n)}$, which only depends on $h^{(n)}/l^{(n)}$.The second expression in Eq. (4.6) is the same as that reported in the reference (Gibson and Ashby, 1997) for non-hierarchical honeycomb.And, the Young's modulus ($E_1^{(n-1)}$) of the cell walls is (Chen et al., 2011):

The second expression in Eq. (4.6) is the same as that reported in reference (Gibson and Ashby, 1997) for non-hierarchical honeycomb. The Young's modulus ($E_1^{(n-1)}$) of the cell walls is (Chen et al., 2011):

$$E_1^{(n-1)} = \prod_{i=1}^{n-1} \left(\xi^{(i)} \left(\frac{t^{(i)}}{l^{(i)}} \right)^3 \right) \cdot E_1^{(0)} \tag{4.7}$$

with

$$\xi^{(i)} = \frac{(h^{(i)}/l^{(i)} + \sin\theta^{(i)})}{\cos^3\theta^{(i)}} \tag{4.8}$$

If we define a new pseudo-vector $\overrightarrow{\omega^{(n)}} = (\omega_1^{(n)}, \omega_2^{(n)})^T$:

$$\begin{aligned} \omega_1^{(n)} &= \cot\theta^{(n)} \\ \omega_2^{(n)} &= 2\cos\theta^{(n)} \end{aligned} \tag{4.9}$$

then, Eq. (4.4) can be rewritten as:

$$\overrightarrow{P^{(n)}} = \left(sA^{(n)} \frac{l^{(n)}}{t^{(n)}} \right) \otimes \overrightarrow{\omega^{(n)}} \tag{4.10}$$

where $\otimes$ is the Kronecker product and $A^{(n)} = b^{(n)}t^{(n)}$ is the cross-sectional area of the cell wall at the n^{th} level.

Correspondingly, Eq. (4.6) is expressed as:

$$
\begin{aligned}
s_{cr,1}^{(n)} &= \frac{\pi^2 \left(\lambda_1^{(n)}\right)^2 E_1^{(n-1)}}{12} \left(\frac{t^{(n)}}{l^{(n)}}\right)^3 \frac{1}{\omega_1^{(n)}} \\
s_{cr,2}^{(n)} &= \frac{\pi^2 \left(\lambda_2^{(n)}\right)^2 E_1^{(n-1)}}{12} \left(\frac{t^{(n)}}{h^{(n)}}\right)^2 \left(\frac{t^{(n)}}{l^{(n)}}\right) \frac{1}{\omega_2^{(n)}}
\end{aligned}
\tag{4.11}
$$

Furthermore, Eq. (4.11) is expressed as:

$$
\overrightarrow{s_{cr}^{(n)}} = \left[K_s^{(n)}\right] \left(\overrightarrow{\omega^{(n)}}\right)^{-1} E_1^{(n-1)} \tag{4.12}
$$

where,

$$
\left[K_s^{(n)}\right] = \frac{\pi^2}{12} \operatorname{diag}\left(\left(\lambda_1^{(n)}\right)^2 \left(\frac{t^{(n)}}{l^{(n)}}\right)^3,\ \left(\lambda_2^{(n)}\right)^2 \left(\frac{t^{(n)}}{h^{(n)}}\right)^2 \left(\frac{t^{(n)}}{l^{(n)}}\right) \right)
$$

$$
\left(\overrightarrow{\omega^{(n)}}\right)^{-1} = \left(\frac{1}{\omega_1^{(n)}}, \frac{1}{\omega_2^{(n)}} \right)^T
$$

Accordingly, the local buckling stress at level *n* is the minimum one in the critical stress vector $\overrightarrow{s_{cr}^{(n)}}$, i.e.

$$
s_{cr}^{(n)} = \min(\overrightarrow{s_{cr}^{(n)}}) \tag{4.13}
$$

(b) Buckling strain analysis

In buckling stress analysis, we dealt with the elastic buckling stress whereas the corresponding buckling strain is derived here. First, we make an assumption: when one of the beams buckles, it collapses immediately and completely (see Fig. 4.5). The displacements $\overrightarrow{\Delta\delta_{cr}^{(n)}} = \left(\Delta\delta_{cr,1}^{(n)}, \Delta\delta_{cr,2}^{(n)}\right)^T$ of pair ①, ② at level *n* are obtained through geometrical analysis in a unit cell:

$$
\begin{aligned}
\Delta\delta_{cr,1}^{(n)} &= l^{(n)} \sin\theta^{(n)} \\
\Delta\delta_{cr,2}^{(n)} &= h^{(n)}
\end{aligned}
\tag{4.14}
$$

and the buckling strains of pair ①, ② are $\overrightarrow{\Delta\varepsilon_{cr}^{(n)}} = \left(\Delta\varepsilon_{cr,1}^{(n)}, \Delta\varepsilon_{cr,2}^{(n)}\right)^T$:

$$
\begin{aligned}
\Delta\varepsilon_{cr,1}^{(n)} &= \frac{\Delta\delta_{cr,1}^{(n)}}{l^{(n)} \sin\theta^{(n)} + h^{(n)}} \\
\Delta\varepsilon_{cr,2}^{(n)} &= \frac{\Delta\delta_{cr,2}^{(n)}}{l^{(n)} \sin\theta^{(n)} + h^{(n)}}
\end{aligned}
\tag{4.15}
$$

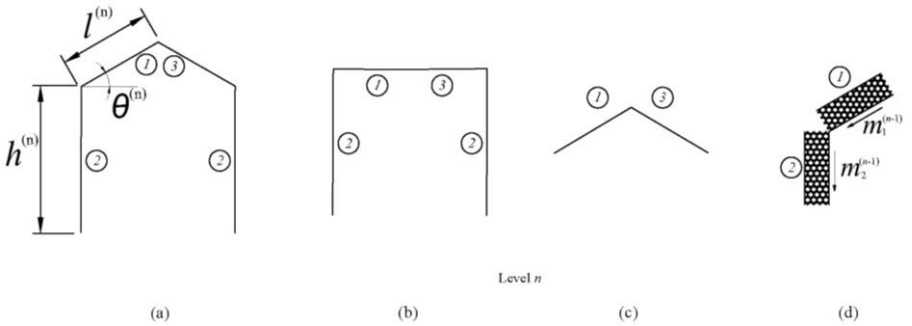

Fig. 4.5 Buckling collapse of n^{th} hierarchical honeycomb: (a) initial configuration; (b) collapse of beams ①, ③; (c) collapse of beams ②; (d) numbers of unit cells in beam ①, ②.

Thus, in general:

$$\overrightarrow{\Delta\varepsilon_{cr}^{(n)}} = \frac{1}{l^{(n)}\sin\theta^{(n)} + h^{(n)}}\overrightarrow{\Delta\delta_{cr}^{(n)}} \tag{4.16}$$

It is worth to say that due to the analogy between hierarchical and fractal in the context of mechanics, for the n^{th} hierarchical honeycombs, here, we would like to discuss corresponding fractal briefly. According to the fractal definition, the thickness and lengths of cell walls are expressed as $t_F = (t^{(n)})^{D_t}$, $l_F = (l^{(n)})^{D_l}$ and $h_F = (h^{(n)})^{D_h}$, respectively, where $t^{(n)}$, $l^{(n)}$ and $h^{(n)}$ are, respectively, real thickness and lengths at level n; D_t, D_l and D_h are fractal dimensions of thickness and lengths. Therefore, the fractal expressiones can be obtained by replacing $t^{(n)}$, $l^{(n)}$ and $h^{(n)}$ with t_F, l_F and h_F respectively from Eq. (4.2) to Eq. (4.16); However, in order to investigate the influence of t/l, we do not discuss the fractal in the following Sections.

The (n-1)th level structure

(a) Buckling stress analysis

Here, the (n-1)th level structure corresponds to the cell walls of the n^{th} level structure treated before, that is to say, each pair cell walls of the n^{th} level contains two pairs cell walls of the (n-1)th level structure. Thus, for the (n-1)th level structure, we have four pairs. Now we use the results of the n^{th} level and find the stresses of thefour

pairs:

$$\overrightarrow{P^{(n-1)}} = \left(sA^{(n-1)} \frac{l^{(n-1)}}{t^{(n-1)}} \right) \otimes \overrightarrow{\omega^{(n)}} \otimes \overrightarrow{\omega^{(n-1)}} \tag{4.17}$$

Following the previous procedure, we find the critical loads for the four pairs of cell wall at the $(n\text{-}1)^{\text{th}}$ level:

$$\overrightarrow{s_{cr}^{(n-1)}} = \left(\overrightarrow{\omega^{(n)}} \right)^{-1} \otimes \left(\left[K^{(n-1)} \right] \left(\overrightarrow{\omega^{(n-1)}} \right)^{-1} \right) E_1^{(n-2)} \tag{4.18}$$

Thus, the local buckling load at the $(n\text{-}1)^{\text{th}}$ level is derived as:

$$s_{cr}^{(n-1)} = \min(\overrightarrow{s_{cr}^{(n-1)}}) \tag{4.19}$$

(b) Buckling strain analysis

Like at level n, the displacements $\overrightarrow{\Delta\delta_{cr}^{(n-1)}}$ of pair ①, ② at level n-1 can be derived as:

$$\begin{aligned} \Delta\delta_{cr,1}^{(n-1)} &= l^{(n-1)} \sin\theta^{(n-1)} \\ \Delta\delta_{cr,2}^{(n-1)} &= h^{(n-1)} \end{aligned} \tag{4.20}$$

If we define:

$$\overrightarrow{m^{(n-1)}} = \left(m_1^{(n)} \sin\theta^{(n)}, m_2^{(n)} \right)^T \tag{4.21}$$

where, $m_1^{(n)}$, $m_2^{(n)}$ are numbers of unit cells at level n-1 along the longitudinal direction of the beams ①, ② at level n (see Fig. 4.6(d)), the buckling strain at level n-1 is expressed as:

$$\overrightarrow{\Delta\varepsilon_{cr}^{(n-1)}} = \frac{1}{l^{(n)} \sin\theta^{(n)} + h^{(n)}} \overrightarrow{m^{(n)}} \otimes \overrightarrow{\Delta\delta_{cr}^{(n-1)}} \tag{4.22}$$

The 1st level structure

(a) Buckling stress analysis

Similarly, the above stress result can be used for the first level structure by extending Eqs. (4.17)-(4.19):

$$\overrightarrow{P^{(1)}} = \left(sA^{(1)} \frac{l^{(1)}}{t^{(1)}} \right) \otimes \overrightarrow{\omega^{(n)}} \otimes \overrightarrow{\omega^{(n-1)}} \cdots \otimes \overrightarrow{\omega^{(1)}} \tag{4.23}$$

The critical loads of each pair at the first level structure are:

$$\overrightarrow{s_{cr}^{(1)}} = \left(\overrightarrow{\omega^{(n)}} \right)^{-1} \otimes \left(\overrightarrow{\omega^{(n-1)}} \right)^{-1} \cdots \otimes \left(\overrightarrow{\omega^{(2)}} \right)^{-1} \otimes \left(\left[K^{(1)} \right] \left(\overrightarrow{\omega^{(1)}} \right)^{-1} \right) E_1^{(0)} \tag{4.24}$$

The local buckling stress at the first level is:

$$s_{cr}^{(1)} = \min(\overrightarrow{s_{cr}^{(1)}}) \tag{4.25}$$

(b) Buckling strain analysis

Extending Eq. (4.22), the buckling strain at level 1 is expressed as:

$$\overrightarrow{\Delta\varepsilon_{cr}^{(1)}} = \frac{1}{l^{(n)} \sin\theta^{(n)} + h^{(n)}} \overrightarrow{m^{(n)}} \otimes \overrightarrow{m^{(n-1)}} \otimes \cdots \otimes \overrightarrow{m^{(2)}} \otimes \overrightarrow{\Delta\delta_{cr}^{(1)}} \tag{4.26}$$

4.2.3 Local buckling load of the whole hierarchical structure

Now, we have the local buckling loads at each level, but we usually need the buckling load for the whole structure, that is:

$$S_{cr}^{(n)} = \min(s_{cr}^{(1)}, s_{cr}^{(2)}, \cdots, s_{cr}^{(n)}) \tag{4.27}$$

4.2.4 Strength efficiency

The strength-to-density ratio is an important index to design and optimize energy-absorbing materials. Budiansky (1999) studied the structural efficiency of several compression structures (e.g. hollow columns and foam-filled sandwich columns) by the maximum stress and strain. Here, in order to evaluate the strength efficiency of the hierarchical honeycombs, we employ a strong tie provided by Ashby (2010). For a uniaxial loading structure, the strong tie is expressed as $P_{s1}=S/\rho$, then, a light but strong structure can be obtained by optimizing the value. Employing the expression of the relative density for non-hierarchical honeycombs (Gibson and Ashby, 1997), we have:

$$\frac{\rho^{(n)}}{\rho^{(n-1)}} = \frac{(h^{(n)} / l^{(n)} + 2)}{2\cos\theta^{(n)} (h^{(n)} / l^{(n)} + \sin\theta^{(n)})} \frac{t^{(n)}}{l^{(n)}} \tag{4.28}$$

thus, the density of the *n*-level hierarchical structure is derived by an iterative process

as:

$$\frac{\rho^{(n)}}{\rho^{(0)}}=\prod_{i=1}^{n}\left(\gamma^{(i)}\frac{t^{(i)}}{l^{(i)}}\right) \tag{4.29}$$

with

$$\gamma^{(i)}=\frac{(h^{(i)}/l^{(i)}+2)}{2\cos\theta^{(i)}(h^{(i)}/l^{(i)}+\sin\theta^{(i)})}$$

Therefore, combining Eqs. (4.27) and (4.29), the strength-to-density is expressed as:

$$\frac{S_{cr}^{(n)}}{\rho^{(n)}}=\frac{\min(s_{cr}^{(1)},s_{cr}^{(2)},\cdots,s_{cr}^{(n)})}{\rho^{(0)}\times\prod_{i=1}^{n}\left(\gamma^{(i)}\frac{t^{(i)}}{l^{(i)}}\right)} \tag{4.30}$$

4.3 Parametric analysis

The influences of the parameters in the vector $\overrightarrow{\chi^{(i)}}=(\theta^{(i)},h^{(i)}/l^{(i)},t^{(i)}/l^{(i)})$ are investigated under the self-similar conditions: $h^{(i)}/l^{(i)}=h/l$, $t^{(i)}/l^{(i)}=t/l$, and thus $t^{(i)}/h^{(i)}=t/h$; the boundary coefficient $\lambda_2^{(i)}$ is a function of $h^{(i)}/l^{(i)}$, as well as $\lambda_2^{(i)}=\lambda_2$. Thus, the self-similar conditions are:

$$\overrightarrow{\chi^{(i)}}=\vec{\chi}=(\theta,h/l,t/l)\quad i=1,\ 2,\ \ldots,n \tag{4.31}$$

In this section, inspired by wood, we treat the example of hierarchical honeycombs. The elastic modulus $E_1^{(0)}=10600\,\text{MPa}$ and density $\rho^{(0)}=1.5\,\text{g/cm}^3$ (Easterling et al., 1982) of wood cell walls are adapted here.

4.3.1 Local buckling stress

Here, the local buckling stress refers to the buckling stress under which the first buck Here, the local buckling stress refers to the buckling stress under which the first column takes place, see Eq. (4.27). Taking a two-level self-similar honeycomb as an example, the parametric analysis results are plotted in Fig. 4.6.

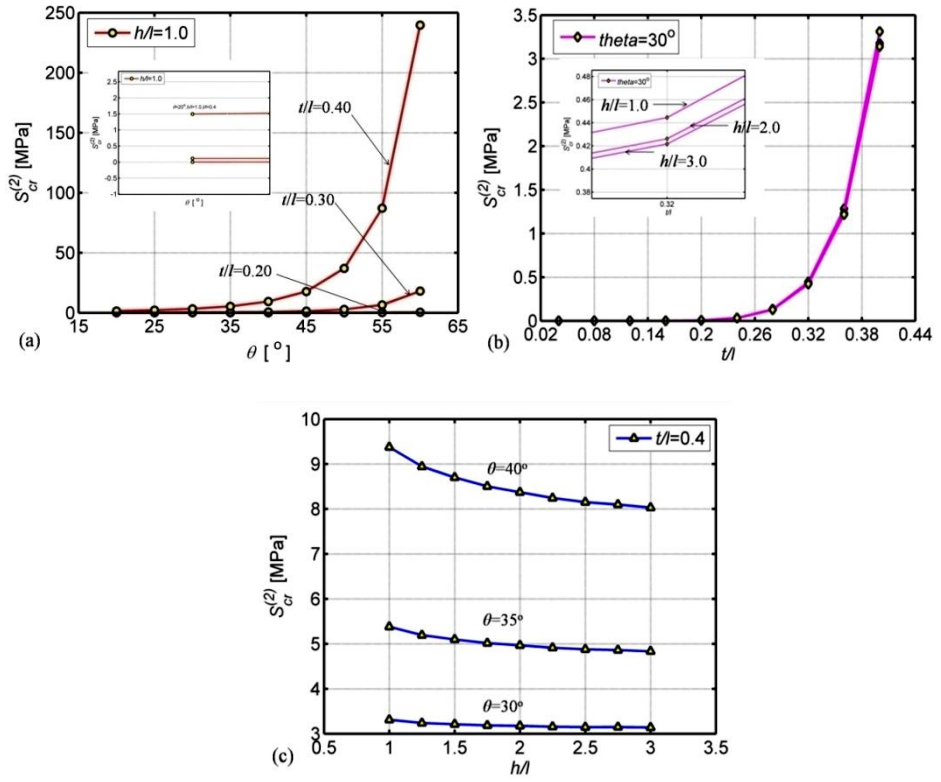

Fig. 4.6 Parametric analysis on the buckling stress $S_{cr}^{(2)}$ of a two-level hierarchical honeycomb. Insets in Fig.4.6a, b are local magnifications, respectively.

Fig. 4.6 shows the influences of two components in the vector $\vec{\chi}$ with the left one fixed. We can see that the buckling stress generally increases when *t/l* and θ increase (Fig.4.6a,c); while it decreases when *h/l* increases (see the inset in Fig.4.6b), and increasing *h/l* produces a weak influence (Fig.4.6c), compared with the other two.. For the mechanical behavior influenced by the three geometric parameters in the vector $\vec{\chi}$, there are three different reasons: increasing *t/l* produces a larger bending rigidity of the inclined columns, thus, Young's modulus is enhanced, furthermore, the buckling strength is improved; likewise, increasing θ with other parameters fixed results in larger Young's modulus (Eqs. (4.7) and (4.8)) and again the structural strength

increases; as for *h/l*, it produces an inverse effect. This is because increasing *h/l* results in a lower buckling stress.

Also, we compare our result with the transverse strength of natural wood, which is defined as the stress at proportional limit corresponding to the first bucking stress in our model. For example, radial compression strength of *Balsa* is about 1500kPa (Easterling et al., 1982), which is corresponding to the value 1497 kPa at $\vec{\chi} = (20^{o}, 1.0, 0.4)$ (see the inset in Fig.4.6a). Besides, more strength properties of some important commercial woods are available in Green et al. (1999), and their transverse compression strength ranges from 1000kPa to 19000kPa, which match our result very well by selecting the corresponding parameters.

4.3.2 Strength efficiency

Based on the density value of wood, the strength to density ratios $S_{cr}^{(2)}/\rho^{(2)}$ of the two-level hierarchical structures influenced by $\theta, h/l$ and t/l are shown in Fig. 4.7.

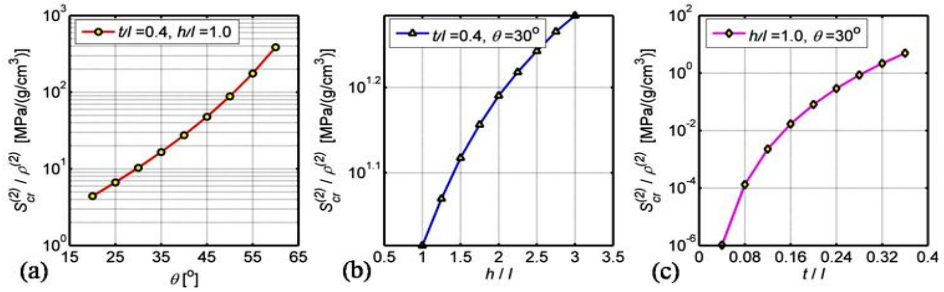

Fig. 4.7 Parametric analysis on the strength-to-density ratio of the two-level hierarchical honeycomb.

It suggests that the strength efficiency increases when one of these geometrical parameters increases. And the increase in θ or t/l is more efficient than that in *h/l*. The former improve the buckling-resisting capacity by approximately two or six orders of magnitude (θ from 20^{o} to 60^{o} and t/l from 0.04 to 0.36), while the latter is in the

same order when h/l varies from 1.0 to 3.0. However, different from Fig.4.6b, Fig.4.7b shows that increasing *h/l* results in higher strength efficiency. This is because the increasing *h/l* provides a lower density, and the influence on density is stronger than that on strength. We can also see that the strength efficiency influenced by the other geometrical parameters (θ or t/l) are similar as those in Fig.4.6a,c, since the strength increment prevails on the density increment.

4.3.3 Progressive buckling collapse

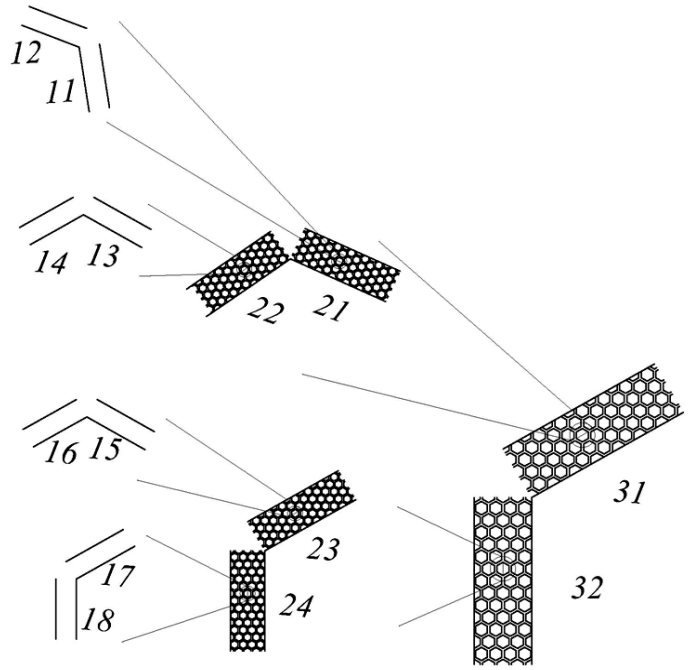

Fig. 4.8 Schematic of a three-level hierarchical honeycomb. The subscripts of each column reflect the location in the hierarchical structure; the first subscript denotes the level and the second its location in the level.

Compared with the first buckling stress, the progressive failure of the hierarchical honeycomb is more complex. Thus, due to the complexity, the calculation is here simplified by neglecting the influences produced by collapsed columns (e.g., a length

modification or a load redistribution in surviving columns) and plotting the stress vector $(\overrightarrow{\sigma_{cr}^{(n)}},\overrightarrow{\sigma_{cr}^{(n-1)}},\cdots,\overrightarrow{\sigma_{cr}^{(1)}},\overrightarrow{\sigma_{cr}^{(0)}})$ in ascending order with corresponding normalized strain $(\sum\Delta\varepsilon=1)$ obtained from the vector $(\overrightarrow{\Delta\varepsilon_{cr}^{(n)}},\overrightarrow{\Delta\varepsilon_{cr}^{(n-1)}},\cdots,\overrightarrow{\Delta\varepsilon_{cr}^{(1)}},\overrightarrow{\Delta\varepsilon_{cr}^{(0)}})$. Note that this simplified assumption is conservative. Here, we investigate a three-level self-similar honeycomband treat 14 (8+4+2) different columns, due to the symmetry, see Fig.4.8.

Note that:

$$h^{(i)}/l^{(i)}=m_2^{(i)}/m_1^{(i)}=h/l \tag{4.32}$$

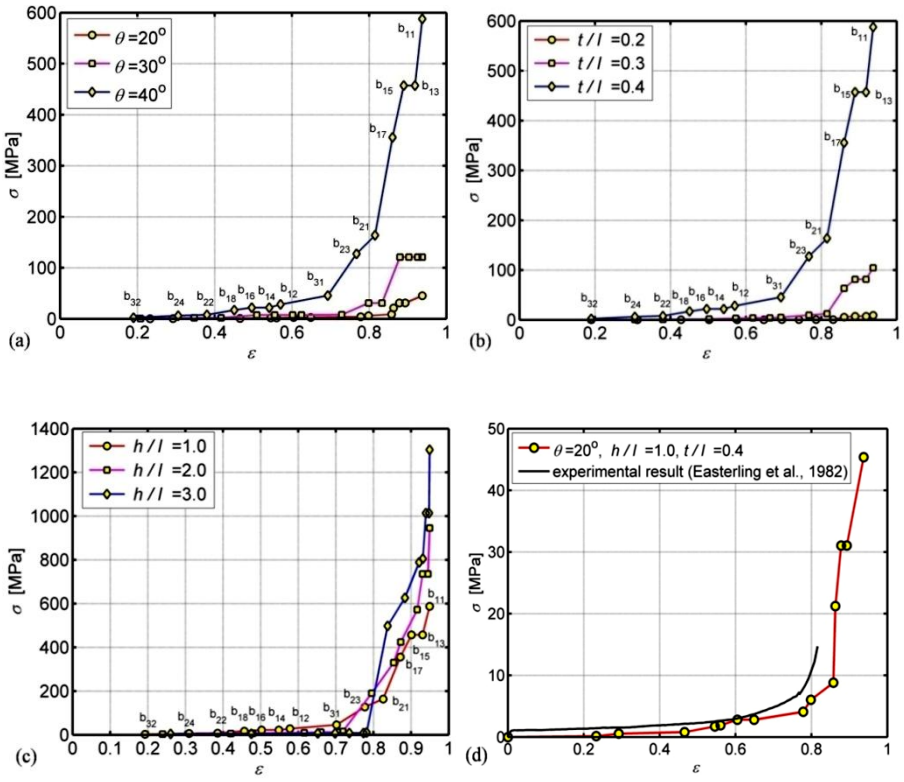

Fig. 4.9 Progressive failure stress-strain relationship of a three-level hierarchical honeycomb: (a) h/l=1.0, t/l=0.1; (b) θ=40°, t/l=0.1; (c) θ=40°, h/l=1.0; (d) comparison between theory and experiment.

4.3.4 Constitutive laws and deformation energy

In addition, employing the same procedure as Section 4.3.3, we investigate the stress/strain curves (Fig.4.10) and energy density (deformation energy per unit volume) or specific energy (deformation energy per unit mass) (Fig.4.11) according to different level *n*, which is from one to three. We find that energy density decreases, since buckling stress strength decreases as level *n* increases; while specific energy increases, since structural density decreases as level *n* increases. This indicates that level *n* increases, the hierarchical structure is more efficient. And for the two-level structure, the structure reaches a balance between energy density and specific energy, this may explain why wood and grass stem have two hierarchical levels in Fig.4.2.

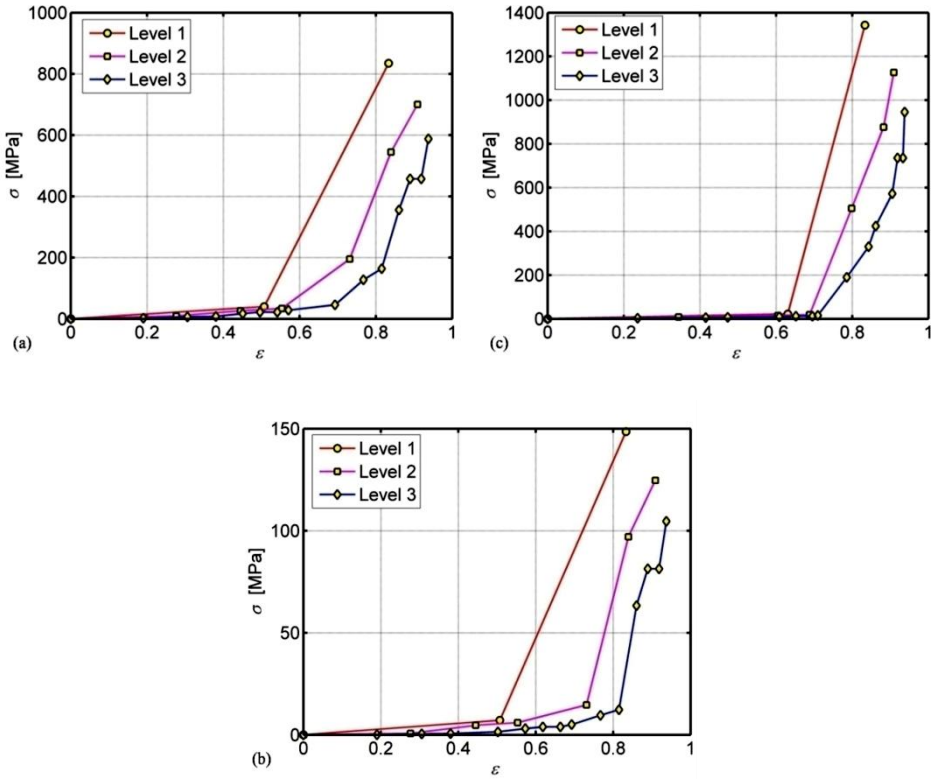

Fig. 4.10 Stress/strain curve *vs* level *n*: (a) h/l=1.0, t/l=0.4, θ=40^o; (b) h/l=1.0, t/l=0.3, θ=40^o; (c) h/l=2.0, t/l=0.4, θ=40^o.

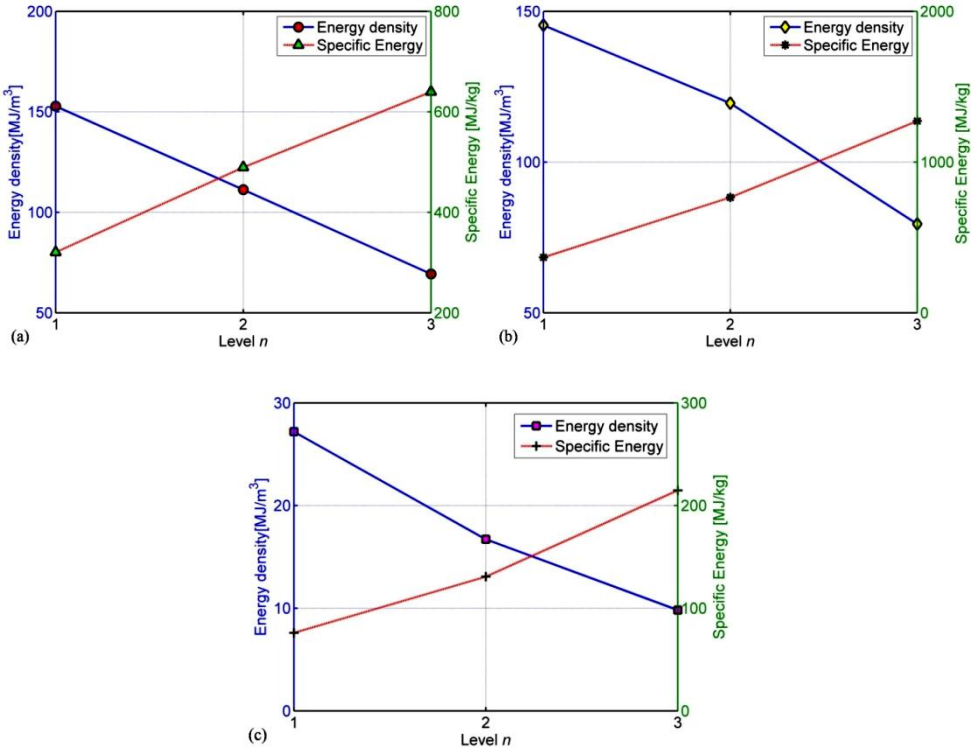

Fig. 11 Energy density & Specific energy *vs* level *n*: (a) h/l=1.0, t/l=0.4, θ=40^o; (b) h/l=1.0, t/l=0.3, θ=40^o; (c) h/l=2.0, t/l=0.4, θ=40^o.

Chapter 5

Hierarchical Honeycomb: Strength and Toughness

In this Chapter, we analytically calculate the in-plane fracture strength and fracture toughness of a defective hierarchical honeycomb. Incorporating the surface effect and quantized fracture mechanics (QFM), the classical formula for honeycomb-strength prediction is modified, then, it is extended to hierarchical architectures by employing an iterative process. The results show that two main geometric parameters and the emergence of cracks produce important influences on the fracture strength and fracture toughness. The modified strength prediction eliminates the singularity of the classical formula. The theory could be helpful to design a new class of real thus defective hierarchical honeycomb materials.

5.1 Introduction

Honeycomb, as a classical material, holds a promising industrial and technological application. In the field of material science, recently numerous technologies developed permit us to manufacture various multifunctional cellular solids. Multifunctional honeycombs can be used for energy absorption, mechanical damping, sound absorption and thermal insulation (Evans et al., 2001; Wadley et al., 2006; Xu et al., 2009). With such extensive applications, one of the important issues in

material science is to characterize and model the in-plane and out-plane mechanical behaviors of honeycomb structures (Gibson and Ashby, 1982; Warren and Kraynik, 1987; Zhang and Ashby, 1992; Papka and Kyriakides, 1994, 1998), in order to design various materials for different applications.

And more, hierarchy, as an important structural property of biological materials, e.g. gecko's feet (Chen et al., 2008), has inspirationally been incorporated into the honeycomb structures. Fan et al. (2008) investigated two-dimensional (2D) hierarchical cellular materials made up of sandwich walls and deduced the formulas on stiffness, buckling strength, plastic collapse strength, brittle failure strength and fracture toughness; whereas Côté et al. (2009) studied the compressive strength of a sandwich panel with a hierarchical square honeycomb core; both show that the hierarchical topology enhances the mechanical behaviors of the hierarchical structures. However, by considering the hexagonal, triangular or square geometries into super and sub-structure cells, Taylor et al. (2011) investigated the mechanical behaviors of hierarchical honeycombs and reported that additional hierarchy could result in reducing behaviors; also, Chen and Pugno (2011a, b, c, d) investigated the self-similar hexagonal honeycomb structure, namely, the super- and sub-structures are both hexagonal, and its mechanical behaviors, including linear-elastic properties and buckling; in particular, the authors consider the structure in nanoscale and surface effect is included.

In this Chapter, we create a hierarchical honeycomb (Lakes, 1993; Pugno, 2006a; Pugno et al., 2008; Gao, 2006; Sen and Buehler, 2010; Chen and Pugno, 2011a, b) starting from the nanoscale, and investigate its in-plane mechanical strength and toughness (see Fig.5.1). Nanostructures have important mechanical properties thanks to their high surface-to-volume ratio (Cammarata, 1994), i.e. surface effect becomes important and a lot of works (Wong et al., 1997; Miller and Shenoy, 2000) have been devoted to the topic; for the nanoporous materials, Ouyang et al. (2008) predicted the Young's modulus of nanoporous materials by employing the relationship between surface energy and Young's modulus, and finally investigated the influences of the porosity on the material Young's modulus. On the other hand, for the toughness, we could not treat the honeycomb as a continuous material anymore employing the classical fracture mechanics; in particular, when the crack length is comparable to the size of the unit cell, the classical prediction about the tensile fracture strength of the conventional honeycomb (Gibson and Ashby, 1997) fails. Here, quantized fracture

mechanics (QFM) developed by Pugno (2004, 2006b,c) permits to overcome this limitation, and thus, a modification on the classical prediction is made.

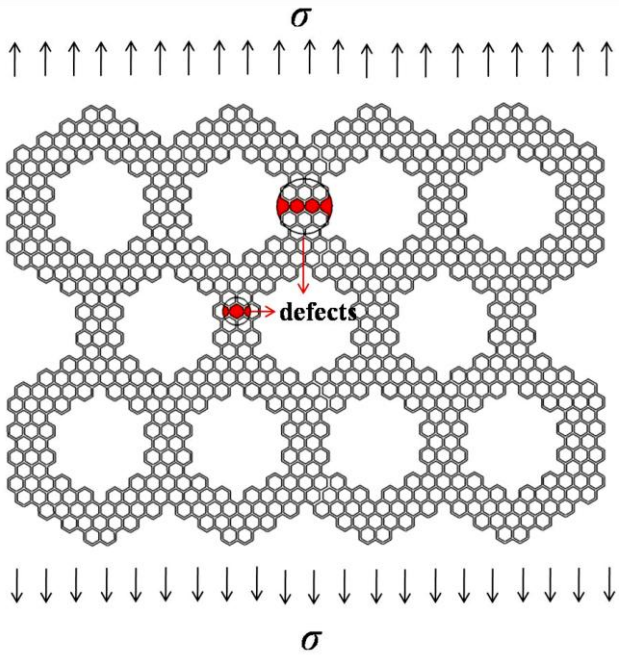

Fig.5.1 Schematic of defective hierarchical honeycomb

This chapter is organized as five parts. Following this section, the second part is the introduction of surface effect theory and QFM, which is used below. In section 5.3, we derive the strength and toughness of the hierarchical honeycomb. Section 5.4 presents an example and discussion about the strength and toughness of a four-level hierarchical structure with the influences of geometric parameters $h^{(i)}/l^{(i)}$ and $\theta^{(i)}$. Finally, conclusions are drawn.

5.2 Surface effect and quantized fracture strength

5.2.1 The surface effect

As the structural size reduces to nanoscale, the surface-to-volume ratio increases and surface effects dominate the mechanical behavior in the competition between

surface materials and bulk materials. A classical theory of surface stresses, basing on energy method, was predicted for the elastic body (Cammarata, 1994; Gurtin and Murdoch, 1975), namely:

$$\tau_{ij} = \tau_{ij}^0 + S_{ij} : \varepsilon_{ij} \tag{5.1}$$

where, τ_{ij} is 2-rank surface stress tensor, τ_{ij}^0 is the surface residual stress tensor, S_{ij} is the surface stiffness matrix, ε_{ij} is surface strain tensor and the symbol $:$ represents the inner product of tensors.

For the one-dimensional case, it can be expressed in a linear form:

$$\tau^s = \tau^0 + E^s \varepsilon \tag{5.2}$$

where, τ^s is surface stress, τ^0 is the surface residual stress, E^s is the surface Young's modulus and ε is surface strain.

5.2.2 The quantized fracture strength

Basing on energy method, QFM was presented and modified the conventional continuum-based fracture mechanics. The crack propagates when (Pugno and Ruoff, 2004):

$$K_I^* = \sqrt{\frac{1}{\Delta A}\int_A^{A+\Delta A} K_I^2 \mathrm{d}A} \tag{5.3}$$

where, K_I^* and K_I are the quantized and conventional stress intensity factor, respectively, A is crack area, ΔA is the fracture quantum and K_{IC} is the critical stress intensity factor of materials.

Defining $\Delta A \equiv at$, then, Eq. (5.1) becomes:

$$K_I^* = \sqrt{\frac{1}{a}\int_c^{c+a} K_I^2 \mathrm{d}c} \tag{5.4}$$

where, c is one half of the crack length and t is the thickness of the plate.

For the Griffith's crack $K_I = \sigma\sqrt{\pi c}$ and thus we find the quantized fracture strength as:

$$\sigma_f = \frac{K_{IC}}{\sqrt{\pi\left(c + \frac{a}{2}\right)}} \tag{5.5}$$

5.3 Strength and toughness of hierarchical honeycomb

5.3.1 The effective strength of constituent materials (level 0)

According to the classical relationship between stress intensity factor and fracture toughness, we have:

$$K_{IC,eff}^{(0)} = \sqrt{G_{IC,eff}^{(0)} E_{eff}^{(0)}} \tag{5.6}$$

where, $K_{IC,eff}^{(0)}$ and $G_{IC,eff}^{(0)}$ are the effective stress intensity factor and strain energy release rate in mode I, and $E_{eff}^{(0)}$ is the effective Young's modulus.

Here, for the effective strain energy release rate $G_{IC,eff}^{(0)}$, we assume:

$$G_{IC,eff}^{(0)} = G_{IC}^{(0)} = 2\gamma^{(0)} \tag{5.7}$$

where, $G_{IC}^{(0)} = 2\gamma^{(0)}$ is the material's surface energy.

For predicting the effective Young's modulus $E_{eff}^{(0)}$, we apply the Miller and Shenoy's approach (Miller and Shenoy, 2000):

$$\lambda_s^{(0)} = \frac{E_{eff}^{(0)}}{E^{(0)}} = 1 + \frac{E_s^{(0)}}{E^{(0)} t^{(1)}} \left(6 + 2\frac{t^{(1)}}{b} \right) \tag{5.8}$$

where, $E^{(0)}$ is the conventional Young's modulus, i.e. without considering the surface effect, $E_s^{(0)}$ is the surface Young's modulus, whereas, $t^{(1)}$ and b are the cross-sectional thickness and width of the cell wall, respectively.

Eq. (5.8) obeys the simple linear scaling law (Wang et al, 2006) $E_{eff}^{(0)} / E^{(0)} = 1 + \alpha^{(0)} l_{\text{in}}^{(0)} / L^{(0)}$, $l_{\text{in}}^{(0)} = E_s^{(0)} / E^{(0)}$ represents a material intrinsic length, under which surface effect plays an important role; $\alpha^{(0)} = 6 + 2t^{(1)}/b$ is a dimensionless constant, which depends on the geometry of the structural elements at the first level and their deformations; $L^{(0)} = t^{(1)}$ is the thickness of the cell wall at the first level. Note that, $\alpha^{(0)}$ is close to 6 if $t^{(1)} \ll b$ (plate) and 8 if $t^{(1)} = b$ (square beam).

Substituting σ_f with an effective material strength $\sigma_{f,eff}^{(0)}$ into Eq. (5.5) and combining Eqs. (5.6)-(5.8), we find it as:

$$\sigma_{f,eff}^{(0)} = \sqrt{\frac{2\gamma^{(0)}E^{(0)}\lambda_s^{(0)}}{\pi(c^{(0)}+\frac{a^{(0)}}{2})}} \tag{5.9}$$

where, $c^{(0)}$ and $a^{(0)}$ are one half of the crack length and the quanta in the constituent material.

The fracture strength can be determined by numerical analyses, e.g. molecular dynamic simulation (Yang et al., 2009), or experiments, e.g. Atomic force microscopy (AFM) (Sundararajan and Bhushan, 2002;Wong et al., 1997). For plastic materials, the critical strain energy release rate can be calculated through J integral and the stress intensity factor as $K_{IC,eff}^{(0)} = \sqrt{J_{IC,eff}^{(0)}E_{eff}^{(0)}}$.

5.3.2 The effective strength and toughness of hierarchical honeycomb

One level (conventional honeycomb)

Here, two types of failures happen in nanohoneycombs. One is the bending collapse of inclined cell walls before crack propagation, and the other is the tensile fracture of vertical cell walls when crack propagates. These two mechanisms are discussed below.

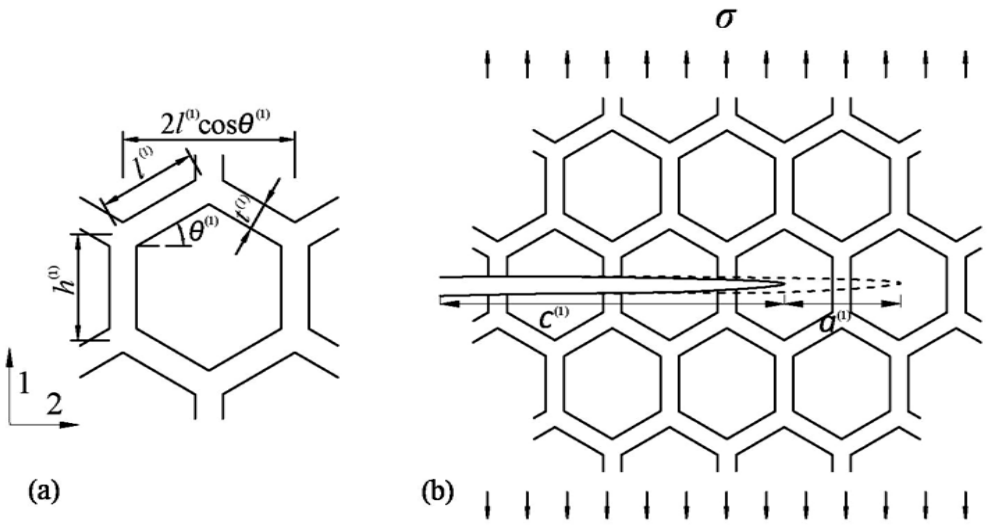

Fig.5.2 Schematic of crack propagation. (a) Geometric size of unit cells, (b) Crack path.

Fracture mechanism 1: For the one-level honeycomb structure (i.e. conventional

honeycomb), the classical theory developed by Gibson and Ashby (1997) can be employed and the tensile strength in 1 direction (Fig.5.2a) is calculated as:

$$\frac{\sigma_{f,1}^{(1)}}{\sigma_{f,eff}^{(0)}} = \frac{1}{3\sqrt{2}\cos^{3/2}\theta^{(1)}}\sqrt{\frac{l^{(1)}}{c^{(1)}}}\left(\frac{t^{(1)}}{l^{(1)}}\right)^2 \tag{5.10}$$

where, $\theta^{(1)}$ is the angle between inclined cell walls and the horizontal line, $l^{(1)}$ and $t^{(1)}$ are the length and thickness of the inclined beams, and $c^{(1)}$ is one half of crack in honeycombs (Fig.5.2b). This expression predicts that the strengths tends to infinity when $c^{(1)}$ approaches zero. In contrast, considering $a^{(1)} = 2l^{(1)}\cos\theta^{(1)}$ (Fig.5.2), QFM implies:

$$K_I^{(1)} = \sigma\sqrt{\pi(c^{(1)} + a^{(1)}/2)} \tag{5.11}$$

where, $K_I^{(1)}$ and σ are the stress intensity factor and external stress acting on the honeycombs, respectively.

Moreover, the stress field of fracture-mode Ⅰ in the vicinity of the crack tip can be described by the classical solution of Williams for the maximum principal stress $\sigma_1^{(1)} = \sigma^{(1)}(r,\varphi)$ (Willams, 1957; Becker et al., 2002):

$$\sigma^{(1)}(r,\varphi) = \frac{K_I^{(1)}}{\sqrt{2\pi r}} f_I^{(1)}(\varphi) \tag{5.12}$$

with

$$f_I^{(1)}(\varphi) = \cos(\frac{\varphi}{2})\left(1+\sin(\frac{\varphi}{2})\right)$$

where, r is the distance from the crack tip, φ is the angle with respect to the crack axis, $f_I^{(1)}(\varphi)$ is a dimensionless function which is independent from the crack geometry and loading condition.

Considering $\varphi = 0$, we find:

$$\sigma(r) = \sigma\sqrt{\frac{c^{(1)} + a^{(1)}/2}{2r}} \tag{5.13}$$

Then, the equivalent force acting on the unit cell in the 1 direction is $P = 2\sigma(a^{(1)})l^{(1)}b\cos\theta^{(1)}$, and the moments acting on both ends of the inclined cell walls are $M = Pl^{(1)}\cos\theta^{(1)}/2$ (Gibson and Ashby, 1997). For the ideal brittle and fully plastic materials, the maximum moment equals:

$$M_{\max}=\begin{cases}\dfrac{1}{6}\sigma_{f.eff}^{(0)}b(t^{(1)})^2 & \text{Ideal brittle materials}\\ \dfrac{1}{4}\sigma_{f.eff}^{(0)}b(t^{(1)})^2 & \text{Fully plastic materials}\end{cases} \tag{5.14}$$

Thus, the honeycomb collapses when $M=M_{\max}$, and we find:

$$\sigma_{f,1}^{(1)}=\frac{\sigma_{f.eff}^{(0)}}{\kappa\cos^2\theta^{(1)}}\sqrt{\frac{1}{2c^{(1)}/a^{(1)}+1}}\left(\frac{t^{(1)}}{l^{(1)}}\right)^2 \tag{5.15}$$

where, $\sigma_{f,1}^{(1)}$ is the tensile fracture strength of the one-level honeycomb due to fracture mechanism 1 along the 1 direction, and κ is a coefficient, $\kappa=2$ if cell walls collapse in fully plastic way or $\kappa=3$ if cell walls collapse in ideally brittle way. Note that Eq. (5.15) reduces to the results of non-crack honeycomb (Gibson and Ashby, 1997) with the crack length $2c^{(1)}=0$ (assuming that the tensile and compressive strength are same) and that the collapse of honeycomb is due to the bending of inclined cell beams.

If $2c^{(1)}=m^{(1)}a^{(1)}$, namely, the crack length is denotes by the number of crack unit cell, then, Eq. (5.15) becomes:

$$\sigma_{f,1}^{(1)}=\frac{1}{\kappa}\cdot\frac{1}{\cos^2\theta^{(1)}\sqrt{m^{(1)}+1}}\left(\frac{t^{(1)}}{l^{(1)}}\right)^2\cdot\sigma_{f.eff}^{(0)} \tag{5.16}$$

where, $m^{(1)}$ is the number of crack cell walls (e.g. $m^{(1)}=6$ in Fig.5.2b).

Thus, the critical stress intensity factor $K_{IC,1}^{(1)}$ can be calculated by Eq. (5.16):

$$K_{IC,1}^{(1)}=\sigma_f^{(1)}\sqrt{\pi(c^{(1)}+a^{(1)}/2)}=\frac{1}{\kappa}\cdot\frac{1}{\cos^2\theta^{(1)}}\left(\frac{t^{(1)}}{l^{(1)}}\right)^2\cdot\sigma_{f.eff}^{(0)}\sqrt{\frac{\pi a^{(1)}}{2}} \tag{5.17}$$

Again, the results is the same as that of Gibson and Ashby for regular hexagonal honeycomb, when $\kappa=3$.

Fracture mechanism 2: In this case, tensile fracture of vertical cell wall happens ($r=a^{(1)}/2$) before the bending collapse of inclined cell walls. Based on Eq. (5.13) and the maximum stress theory, the fracture of the vertical cell wall happens when $\sigma(a^{(1)}/2)=\sigma_{f.eff}^{(0)}$, i.e.:

$$\sigma_{f,2}^{(1)}=\sigma_{f.eff}^{(0)}\sqrt{\frac{a^{(1)}}{c^{(1)}+a^{(1)}/2}} \tag{5.18}$$

and the corresponding critical stress intensity factor $K_{IC,2}^{(1)}$ is calculated as:

$$K_{IC,2}^{(1)} = \sigma_{f,2}^{(1)}\sqrt{\pi(c^{(1)} + a^{(1)}/2)} = \sigma_{f.eff}^{(0)}\sqrt{2\pi l^{(1)}\cos\theta^{(1)}} \tag{5.19}$$

Comparing Eqs. (5.16) and (5.18), thus, we find the fracture strength $\sigma_f^{(1)}$ of the nano-honeycombs, which is expressed as:

$$\sigma_f^{(1)} = \min(\sigma_{f,1}^{(1)}, \sigma_{f,2}^{(1)}) \tag{5.20}$$

and the transition from fracture mechanism 1 to mechanism 2 takes place for:

$$\frac{t^{(1)}}{l^{(1)}} \approx 2\cos\theta^{(1)} \tag{5.21}$$

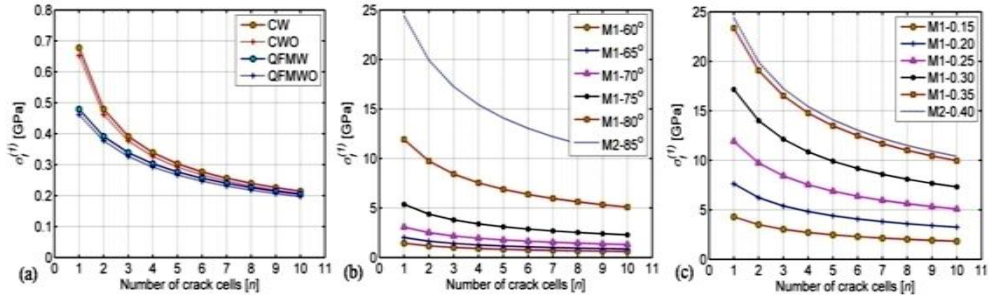

Fig.5.3 (a) Comparison between the classical (C) and QFM theories. 'W' or 'WO' denote predictions with or without surface effect; (b) Influence of $\theta^{(1)}$ on fracture strength of defective nanohoneycombs with $t^{(1)}/l^{(1)}$=0.25; (c) Influence of $t^{(1)}/l^{(1)}$ on fracture strength of defective nanohoneycombs with$\theta^{(1)}$=80°. Note that 'M1' and 'M2'denotes the fracture mode1 and fracture mode 2, respectively.

As an example, we here study the fracture strength $\sigma_f^{(1)}$ of a nano-honeycomb. The single-crystal silicon is considered as the constituent material ($\kappa = 3$), and for the considered (110) surface the Young's modulus is $E^{(0)} = 169$ GPa, whereas the surface elasticity is $E_s^{(0)} = -1$ N/m (Sadeghian et al., 2010) and the surface energy is $\gamma^{(0)} = 1.51$ J/m^2 (Jaccodine, 1963). The thickness of the cell walls is $t^{(1)} = 10\text{nm} << b$, $t^{(1)}/l^{(1)} = 0.25$ and $\theta^{(1)} = 30^\circ$; the cell wall is considered crack-free, i.e. $c^{(0)} = 0$ nm and $a^{(0)} = 0.5431$ nm (Sundararajan and Bhushan, 2002). Then, according to Eq. (5.9), we calculated the effective fracture strength $\sigma_{f,eff}^{(0)} = 24.4$ GPa.

The comparison between the classical result and the QFM one (fracture mode 1) is

reported in Fig.5.3a. As the crack number increases, these two predictions tend to the same value, and this explains why the result is close to those of continuum mechanics for $c^{(1)}/l^{(1)}>7$ (Gibson and Ashby, 2010). Besides, the competition between mode 1 and mode 2 of failure is plotted in Fig.5.3b, c *vs* $\theta^{(1)}$ or $t^{(1)}/l^{(1)}$. It shows that failure mode 2 happens only when the inclined angle $\theta^{(1)}$ and $t^{(1)}/l^{(1)}$ are very large (e.g. $\theta^{(1)}$=85^{o} in Fig.5.3a, $t^{(1)}/l^{(1)}$=0.4 in Fig.5.3b). In other words, the failure usually is due to fracture mechanism 1.

Therefore, the fracture mechanism 1 is based to study the fracture strength and fracture toughness, thus, the critical strain energy release rate $G_{IC,1}^{(1)}=G_{IC,eff}^{(1)}$ is easily derived according to Eq. (5.17):

$$G_{IC}^{(1)}=\frac{\left(K_{IC}^{(1)}\right)^2}{E^{(1)}}=\frac{1}{\kappa^2}\cdot\frac{1}{\cos\theta^{(1)}\left(h^{(1)}/l^{(1)}+\sin\theta^{(1)}\right)}\left(\frac{t^{(1)}}{l^{(1)}}\right)\cdot\frac{a^{(1)}}{\left(2c^{(0)}+a^{(0)}\right)}G_{IC,eff}^{(0)} \tag{5.22}$$

with

$$E^{(1)}=\frac{h^{(1)}/l^{(1)}+\sin\theta^{(1)}}{\cos^3\theta^{(1)}}\left(\frac{t^{(1)}}{l^{(1)}}\right)^3E_{eff}^{(0)}$$

where, $E^{(1)}$ is the Young's modulus of the honeycomb along the loading direction.

Two-level hierarchical honeycomb

For the two-level hierarchical structure, we treat the first level as the constituent material. Then, the iterative process can be employed through Eq. (5.16) if $2c^{(2)}=m^{(2)}a^{(2)}=2m^{(2)}l^{(2)}\cos\theta^{(2)}$:

$$\sigma_f^{(2)}=\frac{1}{\kappa}\cdot\frac{1}{\cos^2\theta^{(2)}\sqrt{m^{(2)}+1}}\left(\frac{t^{(2)}}{l^{(2)}}\right)^2\cdot\sigma_{f.eff}^{(1)} \tag{5.23}$$

with the effective tensile strength of the first level:

$$\sigma_{f,eff}^{(1)}=\sqrt{\frac{G_{IC,eff}^{(1)}E^{(1)}\lambda_s^{(1)}}{\pi\left(c^{(1)}+\frac{a^{(1)}}{2}\right)}}$$

where, $\sigma_f^{(2)}$ is the tensile fracture strength of the second level, $m^{(2)}$ is the number of crack cell walls at the second level, $\theta^{(2)}$ is the angle made by inclined cell walls at the second level and the horizontal line (Fig.5.2), $t^{(2)}$ and $l^{(2)}$ are the thickness and length of the inclined cell walls, respectively, $\lambda_s^{(1)}$ can be calculated through Eq. (5.8)

by substituting the corresponding superscripts .

Accordingly, the stress intensity factor $K_{IC}^{(2)}$ at the second level can be derived:

$$K_{IC}^{(2)} = \frac{1}{\kappa} \cdot \frac{1}{\cos^2 \theta^{(2)}} \left(\frac{t^{(2)}}{l^{(2)}} \right)^2 \cdot \sigma_{f,eff}^{(1)} \sqrt{\frac{\pi a^{(2)}}{2}} \tag{5.24}$$

Similarly, we find the critical strain energy release rate $G_{IC}^{(2)} = G_{IC,eff}^{(2)}$ at the second level:

$$G_{IC}^{(2)} = \frac{1}{\kappa^2} \cdot \frac{1}{\cos\theta^{(2)} (h^{(2)} / l^{(2)} + \sin\theta^{(2)})} \left(\frac{t^{(2)}}{l^{(2)}} \right) \cdot \frac{a^{(2)}}{(m^{(1)}+1) a^{(1)}} G_{IC,eff}^{(1)} \tag{5.25}$$

with (Chen et al., 2011a)

$$E^{(2)} = \frac{h^{(2)} / l^{(2)} + \sin\theta^{(2)}}{\cos^3 \theta^{(2)}} \cdot \left(\frac{t^{(2)}}{l^{(2)}} \right)^3 E_{eff}^{(1)}$$

where, $E^{(2)}$ is the Young's modulus of the two-level structure in the loading direction.

n^{th}-level hierarchical honeycomb

Employing the same procedure, for the *n*-level hierarchical honeycomb, the result of the strength can be expressed as ($2c^{(n)} = m^{(n)} a^{(n)} = 2m^{(n)} l^{(n)} \cos\theta^{(n)}$):

$$\sigma_f^{(n)} = \frac{1}{\kappa} \cdot \frac{1}{\cos^2 \theta^{(n)} \sqrt{m^{(n)}+1}} \left(\frac{t^{(n)}}{l^{(n)}} \right)^2 \cdot \sigma_{f,eff}^{(n-1)} \tag{5.26}$$

with the effective tensile strength of the (*n*-1) level given by:

$$\sigma_{f,eff}^{(n-1)} = \sqrt{\frac{G_{IC}^{(n-1)} E^{(n-1)} \lambda_s^{(n-1)}}{\pi (c^{(n-1)} + \frac{a^{(n-1)}}{2})}}$$

The critical strain energy release rate $G_{IC}^{(n)} = G_{IC,eff}^{(n)}$:

$$G_{IC}^{(n)} = \frac{1}{\kappa^2} \cdot \frac{1}{\cos\theta^{(n)} (h^{(n)} / l^{(n)} + \sin\theta^{(n)})} \left(\frac{t^{(n)}}{l^{(n)}} \right) \cdot \frac{a^{(n)}}{(m^{(n-1)}+1) a^{(n-1)}} G_{IC,eff}^{(n-1)} \tag{5.27}$$

with (Chen et al., 2011a)

$$E^{(n)} = \frac{h^{(n)} / l^{(n)} + \sin\theta^{(n)}}{\cos^3 \theta^{(n)}} \cdot \left(\frac{t^{(n)}}{l^{(n)}} \right)^3 E_{eff}^{(n-1)}$$

where, $E^{(n)}$ is the Young's modulus of the *n*-level structure along the loading direction.

5.3.3 Relative-density ratio

As we know, $t^{(n)}/l^{(n)}$ can be expressed as a function of the honeycomb's geometry and relative density as (Gibson and Ashby, 1997; Chen et al., 2011a):

$$\frac{t^{(n)}}{l^{(n)}}=\frac{2\cos\theta^{(n)}(h^{(n)}/l^{(n)}+\sin\theta^{(n)})}{(h^{(n)}/l^{(n)}+2)}\frac{\rho^{(n)}}{\rho^{(n-1)}} \tag{5.28}$$

thus, the formulas of strength and fracture energy, i.e., Eqs. (5.26) and (5.27), are expressed as:

$$\sigma_f^{(n)}=\frac{4}{\kappa}\cdot\frac{(h^{(n)}/l^{(n)}+\sin\theta^{(n)})^2}{(h^{(n)}/l^{(n)}+2)^2\sqrt{m^{(n)}+1}}\left(\frac{\rho^{(n)}}{\rho^{(n-1)}}\right)^2\cdot\sigma_{f,eff}^{(n-1)} \tag{5.29}$$

$$G_{IC}^{(n)}=\frac{2}{\kappa^2}\cdot\frac{1}{(h^{(n)}/l^{(n)}+2)}\left(\frac{\rho^{(n)}}{\rho^{(n-1)}}\right)\cdot\frac{a^{(n)}}{(m^{(n-1)}+1)a^{(n-1)}}G_{IC,eff}^{(n-1)} \tag{5.30}$$

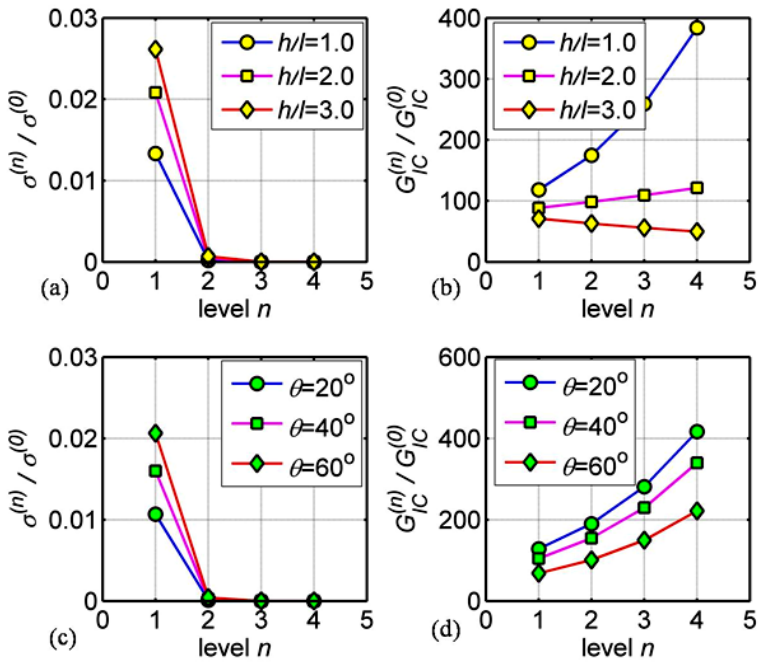

Fig.5.4 (a) Influence of $h^{(i)}/l^{(i)}=h/l$ on strength with $\theta^{(i)}=30^{o}$; (b) Influence of $h^{(i)}/l^{(i)}=h/l$ on toughness with $\theta^{(i)}=30^{o}$; (c) Influence of $\theta^{(i)}=\theta$ on strength with $h^{(i)}/l^{(i)}=1.0$; (d) Influence of $\theta^{(i)}=\theta$ on toughness with $h^{(i)}/l^{(i)}=1.0$.

5.4 Example and discussion

In this section, we continue the aforementioned example on single-crystal silicon but investigate the fracture strength $\sigma_f^{(n)}$ and the critical strain energy release rate $G_{IC}^{(n)}$ of a four-level self-similar hierarchical honeycomb with $a^{(i)} = 2l^{(i)}\cos\theta^{(i)}$, $l^{(i)}/l^{(i-1)} = 100$, $l^{(1)} = 25\,\text{nm}$ and $\rho^{(i)}/\rho^{(i-1)} = 0.2$. Because of the size of the second level is much larger than that of the first level, the surface effect is neglected when level $n \geq 2$. For perfect hierarchical honeycombs (i.e., $m^{(i)} = 0$), the influences of two key geometric parameters on their fracture strength and fracture toughness are reported in Fig.5.4

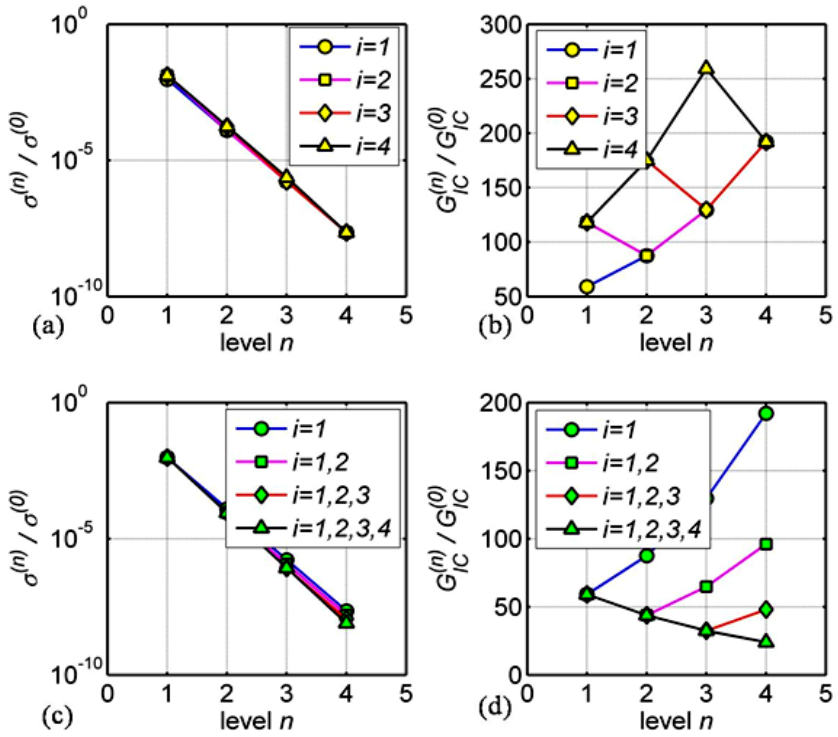

Fig.5.5 (a) Influence of a single defect on strength at one hierarchical level; (b) Influence of a single defect on toughness at one hierarchical level; (c) Influence of multi-defects on strength at different hierarchical levels; (d) Influence of multi-defects on toughness at different hierarchical levels.

For the defective hierarchical honeycomb (i.e., $m^{(i)} > 0$), an investigation on the influences of a single crack at different hierarchical levels (e.g. $m^{(i)} = 1$, i=1 or 2 or 3 or 4) is performed. Also, the influences of multi-cracks are studied (e.g. $m^{(i)} = 1$, $i = 1,2$ or $i = 1,2,3$ or $i = 1,2,3,4$). The results are depicted in Fig.5.5.

From the results concerning perfect hierarchical honeycomb (Fig.5.4), we note that the magnitude of the strength at level (i+1) is about 96% that at level i; besides, the strength and toughness obey the classical exclusive relationship, namely, if strength increases, toughness decreases; otherwise, strength decrease, toughness increase (Launey and Ritchie, 2009; Ritchie, 2011). The reason is that the greater $h^{(i)}/l^{(i)}$ or $\theta^{(i)}$, the greater the moment acting on both the ends of the inclined beams, then, a larger external stress is required, so the strength increases; for toughness, this implies the less deformation and absorbed energy.

As for the results of the defective hierarchical honeycomb (Fig.5.5), we note that both the cases can reduce the strength and toughness influencing the mechanical properties at higher hierarchical levels. The existence of defects causes the jump of materials mechanical properties. This is very interesting, because new functionally grade materials could be developed with this method. In all, as the hierarchical level n increases, materials strength decreases, but with proper design, the materials toughness can be improved.

Chapter 6

Hierarchical Foam: Elasticity and Strength

In this chapter, we study the mechanics of new three-dimensional hierarchical open-cell foam, and, in particular, its Young's modulus and plastic strength. We incorporate the effects of the surface elasticity and surface residual stress in the linear elastic and plastic analyses. The results show that, as the cross-sectional dimension decreases, the influences of the surface effect on the Yong's modulus and plastic strength increase, and the surface effect makes structure stiffer and stronger; similarly, as level n increases, these quantities approach to those of the classical theory as lower bounds.

6.1 Introduction

The structure of materials plays an important role in determining their mechanical properties. In particular biological materials, *e.g.* bone and wood (Fratzl and Weinkamer, 2007), display sophisticated hierarchical structures with different length scales and they have attractive mechanical performances, *e.g.* their toughness (Launey and Ritchie, 2009; Smith et al., 1999). These outstanding properties of all hierarchical structures at different length scales are generating enormous interest. In this regard, the toughening mechanisms in nacre have been extensively studied (Evans et al., 2001) and recently, two theoretical models (Gao, 2006; Zhang et al., 2011; Keten et al., 2010) were brought forward to investigate the mechanical properties of bone-like materials and spider silk. Up to now, engineers and scientists created only a few hierarchical structures. For example, the Eiffel Tower is considered as a three levels structure

(Lakes, 1993); Geim et al. (2003) developed arrays of microfabricated polyimide hairs to mimicking the adhesive and self-cleaning properties of gecko's feet; Munch et al. (2008) synthesized a tough bio-inspired hybrid material basing on aluminum oxide and polymethyl methacrylate, and the final toughness of the product, whose synthesized structure is lamellar as that of nacre, is more than 300 higher than that of the constituent materials.

Foam structures (*e.g.* sponge bone, animal quill and plant stems), on one hand, are often found in Nature, and they provide animals and plants with low weight, high strength etc.; biomimicking of the foam structures may offer the potential to increase the mechanical efficiency of engineering materials (Karam and Gibson, 1994). On the other hand, varieties of artificial open cell foam are studied widely, and recently, Biener et al. (2006) combined nanoindentation, column microcompression and molecular dynamics simulations to study the mechanical behavior of nanoporous Au, and they found nanoporous Au can be as strong as bulk Au, despite possessing high porosity; Wang and Xia (2010) investigated the mechanical properties of hierarchical nano-porous solids, and found that the Young's modulus of the nanostructure is intrinsically size-dependent when considering the surface effect. The surface effect, due to the high surface-to-volume ratio (Cammarata, 1994), plays an important role in determining the mechanical properties of nano-systems. Extensive works (Wang and Feng, 2009; Shankar and King, 2007; Wong et al., 1997; Zhang et al., 2010) studied its influence on linear elastic and plastic properties; in some cases, the surface effect stiffens materials; while in others soften (Zhou and Huang, 2004). In particular, considering the surface energy of nanostructured materials with negative radius of curvature, including nanocavities, nanotubes and shell-core nanostructures, Ouyang et al. (2009) reviewed the status and recent progress on their thermodynamic behavior (e.g. nonlinear shrinkage)

Inspired by biological materials, we build three-dimensional hierarchical foam (Fig. 6.1) (Wang and Xia, 2010; Gibson and Ashby, 1997; Pugno, 2006; Pugno and Carpinteri, 2008; Pugno et al., 2008; Bosia et al., 2010; Chen and Pugno, 2011), and incorporating surface effect at each hierarchical level, we study its linear-elastic and plastic behaviors. Here, we include the effect of surface elasticity in the linear elastic analysis and the effect of the surface residual stress in the plastic analysis, respectively. Finally, considering a three-level hierarchy, we analyze the mechanical properties at each hierarchical level.

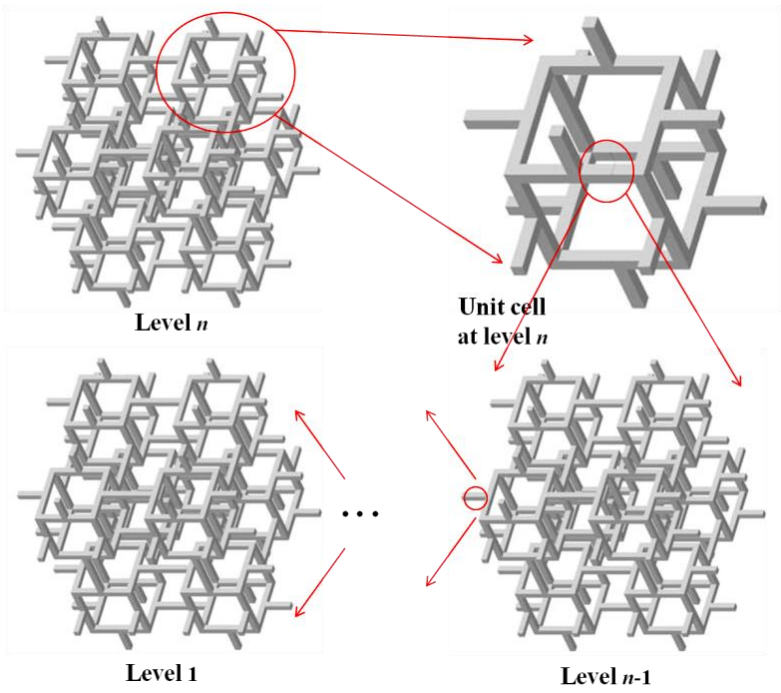

Fig. 6.1 Schematic of hierarchical foam.

This chapter consists of six parts. Section 6.1 is the introduction. Section 6.2 invokes the surface effect. Section 6.3 is the linear-elastic analysis; the Young's modulus is derived, based on an effective bending stiffness, a longitudinal stiffness and an iterative procedure. Section 6.4 presents the plastic analysis and the plastic strength is calculated, basing on an effective yield stress and the iterative procedure. Section 6.5 gives an example of application and employs the self-similar assumption as simplified from Sections 6.3 and 6.4 to analyze the three-level-hierarchical foam. Finally, conclusions are made.

6.2 Surface effect

Surfaces of solids, possessing atoms with fewer neighbor atoms, display an excess energy than the bulk; surface effect is an important property of solid surfaces (Shenoy, 2005), especially in nano-structures. Surface effect consists of two types: the surface

residual stress and surface elasticity. Surface effect was first defined by Gibbs (1961) and, according to Cammarata (1994), the classical surface stress $\sigma_{\alpha\beta}^{s}$ is expressed as:

$$\sigma_{\alpha\beta}^{s} = \gamma\delta_{\alpha\beta} + \frac{\partial\gamma}{\partial\varepsilon_{\alpha\beta}^{s}} \tag{6.1}$$

where, γ is the surface energy, $\delta_{\alpha\beta}$ is the Kronecker delta, $\sigma_{\alpha\beta}^{s}$ and $\varepsilon_{\alpha\beta}^{s}$ are the surface stress and strain tensors, respectively. The expression suggests that the surface energy of nanostructures plays an important role in determining the surface stress. Regarding the relationship between Young's modulus and surface energy, Ouyang et al. (2007), basing on the thermodynamics and continuum medium mechanics, studied the correlation between Young's modulus and surface energy; they focused on carbon nanotubes, explaining the anomalous behavior of the Young's modulus.

In particular, for the one-dimensional linear elastic case, Eq. (6.1) becomes (Wang and Feng, 2009):

$$\sigma_{s} = \tau + E_{s}\varepsilon \tag{6.2}$$

where, τ is the surface residual stress and $E_{s} = E^{*}t$ is the surface Young's modulus. E^{*} is the Young's modulus of the surface layer and t is the thickness.

6.3 Young's modulus

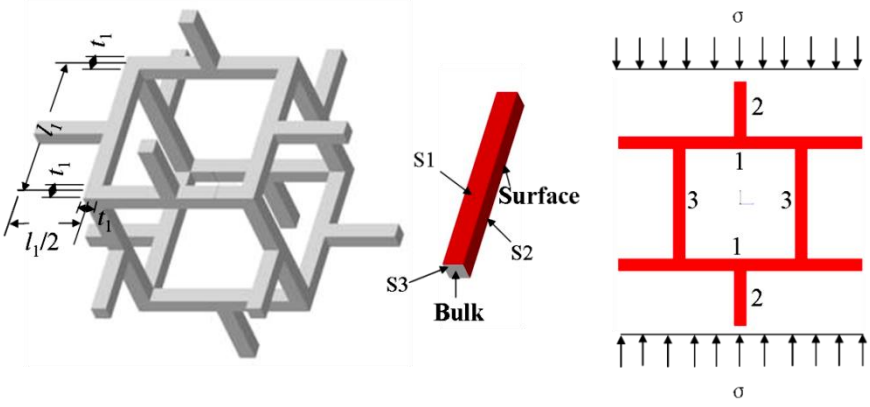

(a) (b) (c)

Fig. 6.2 Unit cell at the first level. (a) unit cell; (b) representative of ribs; (c) external stress acting on the unit cell.

The 1st level

For the first level, the hierarchical foam (Fig. 6.2), is conventional (Gibson and Ashby, 1997) but we here consider the effect of surface elasticity. Under the external stress σ (Fig. 6.2(c)), the linear-elastic deformation displays three components: the first part is caused by the bending of beam 1, and the second and third ones are the axial deformations of beam 2 and beam 3, respectively. Assuming the clamped-clamped boundary condition of beam 1 and small deformations, the displacement due to bending is:

$$\Delta' = 2\times\frac{F/2\cdot l_1^3}{192(EI)_1^e} \tag{6.3}$$

where, $F=4\sigma l_1^2$, Δ' is the mid-point displacement of the beam 1, F and σ are respectively the equivalent concentrated force and the external stress acting on the unit cell, l_1 is the rib length, $(EI)_1^e$ is effective bending rigidity including the surface elasticity and it is expressed as:

$$(EI)_1^e = \frac{E_0 t_1^4}{12}+\frac{2E_0^s t_1^3}{3} \tag{6.4}$$

where, E_0 and E_0^s are the bulk and surface Young's moduli, respectively, and t_1 is the side length of the square cross-section of the ribs at the first level. Note that, Eq. (6.3) is based on the Euler beam theory; if t_1/l_1 is not small enough, then, the shear effect have to be employed, *i.e.*, the Timoshenko beam theory.

Alternatively, from Eq. (6.4), the dimensionless Young's modulus E_0^e/E_0 can be derived as:

$$\frac{E_0^e}{E_0}=1+8\frac{E_0^s}{E_0 t_1} \tag{6.5}$$

Expression (6.5) coincides with the result by (Miller and Shenoy, 2000), and it obeys the scaling law $E_0^e/E_0=1+\alpha l_{\text{in}}/t_1$ (Wang et al., 2006) with $l_{\text{in}}=E_0^s/E_0$ and $\alpha=8.0$. Note that l_{in} is an intrinsic material length, reflecting a condition under which surface effect plays an important role compared to bulk; α is a dimensionless constant, which depends on the geometry of structural elements (*e.g.* bar, plate, etc.) and their deformations (*e.g.* bending, tension, etc.).

The axial displacements of the second and third components are easily derived:

$$\Delta'' = 2\times\frac{F/2\cdot l_1/2}{(EA)_1^e}$$
$$\Delta''' = \frac{F/4\cdot l_1}{(EA)_1^e} \tag{6.6}$$

where, Δ'' and Δ''' are the displacements of beam 2 and 3, respectively, $(EA)_1^e$ is the effective longitudinal stiffness considering the surface elasticity and it is expressed as $(EA)_1^e = E_0 t_1^2 + 4E_0^s t_1$. Like Eq. (6.4), the expression of $(EA)_1^e$ is rearranged as a dimensionless quantity: $E_0^e/E_0 = 1+4E_0^s/(E_0 t_1)$.

Therefore, the total displacement is obtained by summing Eqs. (6.3) and (6.6), *i.e.*, $\Delta_1 = \Delta' + \Delta'' + \Delta'''$. At the same time, considering $F = 4\sigma l_1^2$, we obtain:

$$\Delta_1 = \frac{\sigma l_1^5}{48(EI)_1^e} + \frac{3\sigma l_1^3}{(EA)_1^e} \tag{6.7}$$

thus, the strain ε_1 of the unit cell at the first level can be found:

$$\varepsilon_1 = \frac{\Delta_1}{2l_1} = \frac{\sigma l_1^4}{8(E_0 t_1^4 + 8E_0^s t_1^3)} + \frac{3\sigma l_1^2}{2(E_0 t_1^2 + 4E_0^s t_1)} \tag{6.8}$$

Furthermore, the Young's modulus of the first level is calculated by $E_1 = \sigma/\varepsilon_1$ and normalized by the Young's modulus (E_0) of solid materials, we have:

$$\frac{E_1}{E_0} = \frac{8(t_1/l_1)^4 (t_1 + 4\frac{E_0^s}{E_0})(t_1 + 8\frac{E_0^s}{E_0})}{t_1 (t_1 + 4\frac{E_0^s}{E_0}) + 12(t_1/l_1)^2 t_1 (t_1 + 8\frac{E_0^s}{E_0})} \tag{6.9}$$

The geometry in Fig. 6.2 gives a relative density:

$$\frac{\rho_1}{\rho_0} = \frac{9}{4}\left(\frac{t_1}{l_1}\right)^2 \tag{6.10}$$

Accordingly, the normalized Young's modulus E_1/E_0 is expressed through the relative density as:

$$\frac{E_1}{E_0} = \frac{128(\rho_1/\rho_0)^2 (t_1 + 4\frac{E_0^s}{E_0})(t_1 + 8\frac{E_0^s}{E_0})}{81t_1 (t_1 + 4\frac{E_0^s}{E_0}) + 432(\rho_1/\rho_0) t_1 (t_1 + 8\frac{E_0^s}{E_0})} \tag{6.11}$$

If the rib size t_1 is large enough, then, the surface effect could be neglected ($E_0^s = 0$), and:

$$\frac{E_1}{E_0} = \frac{128(\rho_1/\rho_0)^2}{81 + 432(\rho_1/\rho_0)} \tag{6.12}$$

The expression (6.12) obeys $E_1/E_0 = (\rho_1/\rho_0)^2 / [1 + \alpha(\rho_1/\rho_0)]$, which is a numerical result by curve fitting for three dimensional open cell foams basing on Voronoi models (Gan et al., 2005). Therefore, with the effect of the surface elasticity, the normalized Young's modulus is expressed as the classical power law with respect to the relative density:

$$\frac{E_1}{E_0} = C_1 \left(\frac{\rho_1}{\rho_0} \right)^2 \tag{6.13}$$

with

$$C_1 = \frac{128(t_1 + 4\frac{E_0^s}{E_0})(t_1 + 8\frac{E_0^s}{E_0})}{\left[81t_1(t_1 + 4\frac{E_0^s}{E_0}) + 432(\rho_1/\rho_0)t_1(t_1 + 8\frac{E_0^s}{E_0}) \right]}$$

In addition to the above structural analysis, Ouyang et al. (2008) predicted the Young's modulus of nanoporous materials by employing the relationship between surface energy and Young's modulus, and finally investigated the influences of the porosity on the material Young's modulus.

The 2nd level

For the second level, if the structure has a considerable large size compared with that of the first level and we could neglect the effect of the surface elasticity. However, in general, Eq. (6.13) is employed as an iterative procedure and the normalized Young's modulus of the second level is calculated:

$$\frac{E_2}{E_0} = C_1 C_2 \cdot \left(\frac{\rho_2}{\rho_0} \right)^2 \tag{6.14}$$

where C_2 is calculated by replacements of the corresponding parameters of the second hierarchical level in the expression of C_1.

The nth level

Likewise, the normalized Young's modulus of the n^{th} level can be obtained:

$$\frac{E_n}{E_0} = \prod_{i=1}^{n} C_i \cdot \left(\frac{\rho_n}{\rho_0}\right)^2 \tag{6.15}$$

where, C_i are obtained through replacements of the corresponding parameters of level i in the expression of C_1.

6.4 Plastic Strength

As discussed in the Introduction, hierarchical natural materials or structures exhibit high toughness, and this is because the crack path becomes longer along the different hierarchical levels; meanwhile, the hierarchical structures can inhibit the crack propagation at each level. In our case, we are not considering the presence of a matrix, thus we investigate the plastic strength of the hierarchical foam as main mechanism for energy dissipation. Here, Here, we assume that ribs collapse in a fully plastic way, and the portion below the neutral axis is totally tensile yielded whereas that above the neutral axis is totally compressive yielded.

6.4.1 Effective yield strength

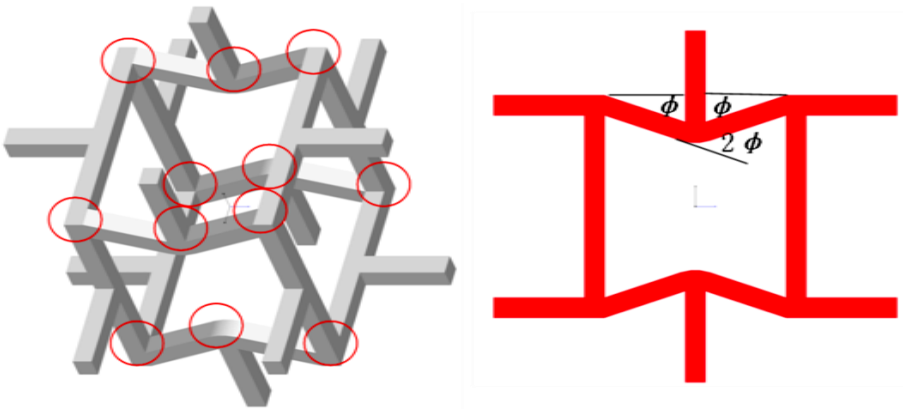

(a) (b)

Fig. 6.3 A unit-cell collapse at the first level. (a) 12 plastic hinges; (b) rotation angles of the plastic hinges.

Like the elastic analysis, we only consider the influence of the surface residual stress on the plastic strength of the first level. Based on the von Mises yield condition,

the effective initial yield strength in axial tension or on compression is expressed as (Yang et al., 2009; Gioia and Dai, 2006):

$$\sigma_e = \frac{\tau' + \tau''}{t_1} \pm \sqrt{\sigma_0^2 - \frac{3}{t_1^2}\left(\tau' - \tau''\right)^2} \tag{6.16}$$

where, τ' and τ'' are surface residual stresses acting on surfaces 1 and 2 (Fig. 6.2 (b)), σ_0 is the yield strength of bulk materials enhanced by any pertinent size effects instead of the surface effect caused by the surface effect, $\pm$ stands for tension $(+)$ or compression $(-)$ of the ribs, respectively.

The 1st level

For the external stress, an upper bound on the plastic collapse stress could be calculated equating the work of the external force F to the plastic work of 12 plastic hinges (Fig. 6.3), *i.e.*:

$$Fl_1\phi = 16M_p\phi \tag{6.17}$$

where, M_p is the plastic moment due to the yield (compression and tension) of all the cross-sectional area, ϕ is the rotating angle of the rib after that plastic hinges emerge.

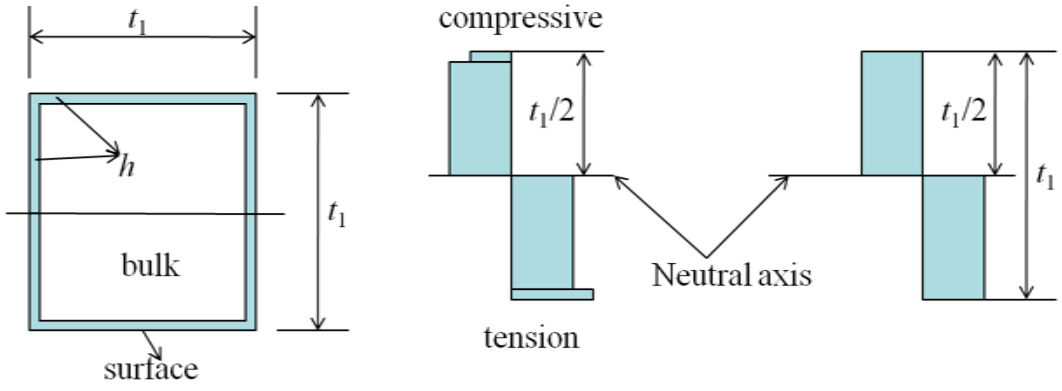

Fig. 6.4 Stress distribution along the cross-section of ribs. (a) surface effect on cross-sectional area; (b) stress distribution with surface effect; (c) stress distribution without surface effect.

Considering the surface residual stress, the cross-sectional stress distribution is shown in Fig. 6.4. Besides, we define the surface thickness (Zheng et al., 2010): $h = nd$, where n is the number of atomic layers which displace a significant surface

residual stress and can be determined by experiments or numerical analysis, and d is the characteristic size of atoms. Here the thickness is considered the same in all hierarchical levels. If h is much smaller than t_1, the neutral axis could still be considered in the middle of the cross-section (Fig. 6.4(b) and (c)). Then, M_p is calculated as:

$$M_p = \left(\frac{1}{4}(1-2\frac{h}{t_1})^3 + \sqrt{1-3(\frac{\tau'-\tau''}{\sigma_0 t_1})} \cdot \frac{h}{t_1}\left(1+\frac{1}{2}(1-2\frac{h}{t_1})^2 \right) \right) \sigma_0 t_1^3 \tag{6.18}$$

substituting M_p and F into Eq. (6.17), we have:

$$\frac{\sigma_1}{\sigma_0} = \left((1-2\frac{h}{t_1})^3 + 2\sqrt{1-3(\frac{\tau'-\tau''}{\sigma_0 t_1})} \cdot \frac{h}{t_1}\left(2+(1-2\frac{h}{t_1})^2 \right) \right) \cdot \left(\frac{t_1}{l_1} \right)^3 \tag{6.19}$$

Eq. (6.19) is different from the Hall-Petch relationship, which is used to calculate the ligament yield strength of nanoporous Au foams influenced by size effect (Hodge et al., 2007). On the other hand, a lower bound is obtained by equating the plastic moment M_p to the maximum bending moment $M_{\max}$ along the beam, *i.e.*:

$$M_p = M_{\max} \tag{6.20}$$

where, $M_{\max} = \frac{1}{16} F l_1$ is the maximum moment along the beam. Employing M_p (Eq. (6.18)), we find:

$$\frac{\sigma_1}{\sigma_0} = \left((1-2\frac{h}{t_1})^3 + 2\sqrt{1-3(\frac{\tau'-\tau''}{\sigma_0 t_1})} \cdot \frac{h}{t_1}\left(2+(1-2\frac{h}{t_1})^2 \right) \right) \cdot \left(\frac{t_1}{l_1} \right)^3 \tag{6.21}$$

Eqs. (6.19) and (6.21) are the same, showing that the result represents the real value. The normalized strength of the first level is expressed by the relative density as:

$$\frac{\sigma_1}{\sigma_0} = C_1' \left(\frac{\rho_1}{\rho_0} \right)^{3/2} \tag{6.22}$$

with

$$C_1^{'}=0.3\left((1-2\frac{h}{t_1})^3+2\sqrt{1-3(\frac{\tau'-\tau''}{\sigma_0 t_1})}\cdot\frac{h}{t_1}\left(2+(1-2\frac{h}{t_1})^2\right)\right)$$

If the influence of the surface residual stress is negligible, the stress distribution will be like that reported in Fig. 6.4(c) and the yield stress will be σ_0. Repeating the procedure or letting $\tau'=\tau''=0$ and $h=0$, we have:

$$\frac{\sigma_1}{\sigma_0}=0.3\left(\frac{\rho_1}{\rho_0}\right)^{3/2} \tag{6.23}$$

This is a classical power law. Note that, the coefficient 0.3 was obtained by experimental fitting (Gibson and Ashby, 1997); here, our derivation provides a theoretical proof.

The 2nd level

Like in the linear elastic analysis, Eq. (6.23) is employed and, iteratively, we find the yield strength of the second level:

$$\frac{\sigma_2}{\sigma_0}=C_1^{'}C_2^{'}\left(\frac{\rho_2}{\rho_0}\right)^{3/2} \tag{6.24}$$

where, $C_2^{'}$ is calculated by replacements of the corresponding parameters of level 2 in the expression of $C_1^{'}$.

The *n*th level

Based on the results of the first and second level structures, the plastic strength of the n^{th} level can be easily derived:

$$\frac{\sigma_n}{\sigma_0}=\prod_{i=1}^{n}C_i^{'}\cdot\left(\frac{\rho_n}{\rho_0}\right)^{3/2} \tag{6.25}$$

where, $C_i^{'}$ are obtained through replacements of the corresponding parameters of level i in the expression of $C_1^{'}$.

6.4.2 Analytic results

In this section, because for the levels greater than or equal to 2, the sizes of their structures are much larger than that of the first level, so, the surface effect can be

neglected and we only consider the influence of the surface effect on the first level.

Firstly, for the Young's modulus, we compare our predictions with the result by Wang and Xia (2010) considering the first level of a conventional foam composed by the same material Au having $E_0 = 78\,\text{GPa}$, $E_s = 6.6\,\text{N/m}$ and $\rho_1 / \rho_0 = 0.2$ (Wang and Xia, 2010; Kiely and Houston, 1997). The comparison is depicted in Fig. 6.5. It shows that the Young's modulus of our structure is 20% higher than calculated by Wang and Xia (2010) because of the different nanostructure (the macro-mechanical properties of materials depend on their micro-structures). However, the influence of the surface effect is comparable, although the influence of the surface effect on the present structure is a little higher than that on the reference.

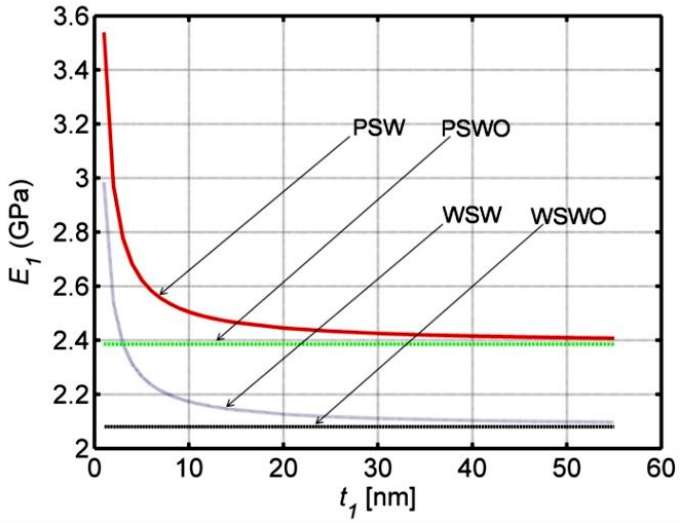

Fig. 6.5 Comparison of Young's moduli between different nano-structures. Note, "PSW" or "PSWO" denote present structure with or without surface effect; "WSW" or "WSWO" denote Wang's structure with or without surface effect.

Also, we investigate a three-level-hierarchical structure with the same Au elastic constants stated above, while surface residual stresses $\tau' = \tau'' = 1.4\,\text{N/m}$ (Shenoy, 2005) on the (001) surface and yield strength $\sigma_0 = 1450\,\text{MPa}$ (Lee et al., 2007) are adopted. Also, for the plastic strength, we use $n = 3$, and $d_{\text{Au}} = 0.288\,\text{nm}$ and a ratio $t_i / l_i = 1/5$; the hierarchical structure is self-similar. Accordingly, the relative density is $\rho_{i+1} / \rho_i = 0.09$ (Eq. (6.10)).

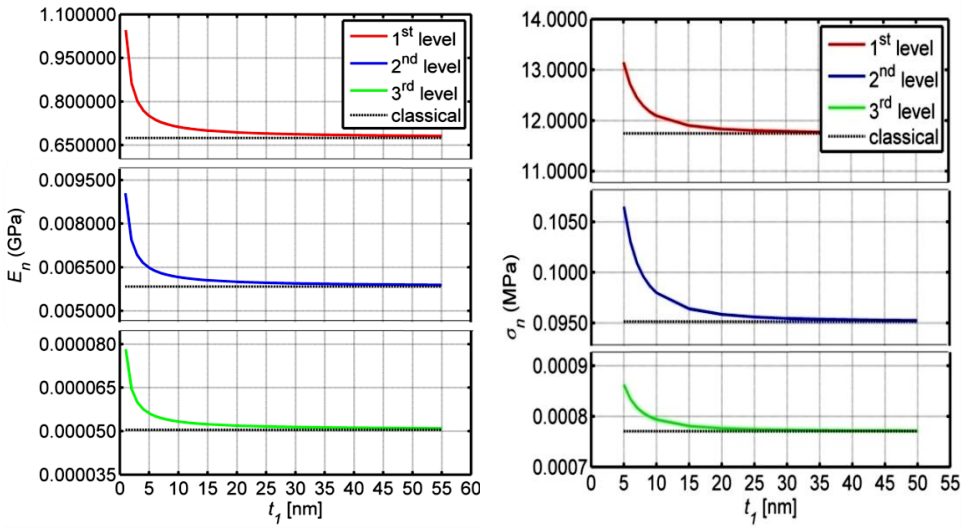

(a) (b)

Fig. 6.6 Influence of the cross-sectional size t_1. (a) Young's modulus vs t_1; (b) Plastic strength vs t_1. Note: 1st (or 2nd, 3rd) level denote the results of the three-hierarchical structure with consideration of surface effect; 'classical' denotes the result calculated from classical theory without consideration surface effect.

The analytic calculations of the Young's modulus and plastic strength are reported in Figs. 6.6. It shows that the smaller t_1, the greater the influence on the Young's modulus and strength and that as t_1 increases, the predictions considering the surface effect approach those of the classical theory. Besides, our predictions including the surface effect are always higher than the classical ones; namely, the material becomes stiffer in the presence of surface effect.

Chapter 7

Conclusions and Outlook

Inspired by the hierarchical structure of natural materials, this thesis formulates three multi-scale hierarchical models, from 2-D hierarchical woven tissue to 2-D hierarchical honeycomb and further to 3-D hierarchical foam, and develops corresponding theories. More specifically, the linear-elastic behavior of 2-D hierarchical woven tissues, the linear elastic, elastic buckling and fracture behavior of the 2-D hierarchical honeycomb, and the linear elastic behavior and strength of the 3-D hierarchical foam are investigated.

Chapter 1 mainly introduces the research background and our motivation. In this section, we analyze several natural hierarchical structures, from nano- to macro-scale, and biomechanical mechanisms governing the mechanical properties of the natural materials. In particular, we stress how cellular structure in natural materials has a high mechanical efficiency which is influenced by its surrounding environment.

Chapter 2 develops a new theory to describe the elastic anisotropy of hierarchical tissues. The method outlined in this chapter shows the possibility of better understanding the elastic properties of biological materials or designing bio-inspired hierarchical tissues with desired elastic properties. Also, the results show the possibility of designing a new class of hierarchical 2-D scaffolds by tailoring elastic anisotropy, better matching the anisotropy of the biological tissues and thus maximizing the regeneration at each hierarchical level. Experimental results on tendons and leaves show a relevant agreement with the predictions of the proposed hierarchical theory.

Chapter 3 calculates the in-plane elastic properties (linear-elastic and buckling properties) of hierarchical nano-honeycombs. The surface effect modifies the classical results of non-hierarchical honeycomb (or conventional honeycomb), which is considered to be the first level (or a one-level structure). Then, employing an iterative

procedure, we obtain the stiffness (or stiffness-to-density ratio) and strength (or strength-to-density ratio) of the *n*th level. Parametric analysis reveals the influences of two key geometrical parameters on the stiffness (or stiffness-to-density ratio) and strength (or srength-to-density ratio), and shows that the elastic properties can be optimized by combining these parameters; furthermore, efficient structures can be obtained.

Chapter 4 derives the buckling stresses and strains of hierarchical honeycomb materials. Parametric analysis is performed for a two-level or three-level hierarchical honeycomb material, respectively. The former is employed to investigate the geometrical influence on the local buckling stress and mechanical efficiency of the structure, in general, these improve when increasing the parameter values except in the case of *h/l*, whose increase results in a lower local buckling stress. The transverse compression strength of natural wood agrees well with our results. The latter is considered to investigate the influence of geometry on the progressive collapse. Finally, the study on the stress/strain law and deformation energy shows that the increasing number of hierarchical levels *n* induces a lower energy density but higher specific energy. The results indicate that the mechanical behaviors of the hierarchical structure can be tuned at each hierarchical level and thus is attractive for designing new materials.

Chapter 5 investigates the fracture strength and fracture toughness of a defective hierarchical honeycomb. Incorporating surface effects and Quantized Fracture Mmechanics (Pugno, 2002; Pugno and Ruoff, 2004), classical fracture strength and fracture toughness are modified. The modification to fracture strength eliminates the singularity when a crack vanishes. The two mechanical properties are studied for perfect and defective hierarchical honeycombs. We discover that the variations of the two mechanical parameters are exclusive when level *N* changes by varying two geometric parameters ($h^{(i)}/l^{(i)}$ and $\theta^{(i)}$) and the crack reduces the fracture strength and toughness. The theory allows us to calculate the fracture strength of the conventional honeycomb materials with defects and design energy-absorption materials with high fracture toughness.

Chapter 6 derives the Young's modulus and plastic strength of a 3-D hierarchical foam, considering surface effects. Based on structural analysis, the Young's modulus is derived considering the effect of surface elasticity and the plastic strength is calculated considering the effect of surface residual stress. We find that the two mechanical

parameters are size-dependent. Both the Young's modulus and the plastic strength increase as the cross-sectional size t_1 of ribs at the first level decreases. This explains the important role of surface effects when considering nanostructures. Thus, the present theory could be used to design some cellular nano-materials for different applications.

However, we must point out that the thesis is only dealing with the structural skeleton compared with natural composite materials, and there is still a distance between models and real bio-inspired materials. Of course, the bio-inspired materials should be based on natural mechanisms, occurring in natural materials. In this regard, although scientific communities have been making progress in revealing some natural mechanisms, progress is still at an early stage and more sophisticated models and methods should be proposed. From the point of view of mechanics, we suggest that future work should take into account the following aspects:

- Hierarchical structure. Usually, the structure at each hierarchical level of natural materials is not self-similar, and therefore, new numerical and theoretical models should try to consider the real structure by combining variety of methods or iterative theories (e.g. molecular dynamics simulations at the nanoscale and continuum mechanics at the macroscale).
- Size effects.
- Anisotropy. Material/structure at each hierarchical level is anisotropic, a fact which is often neglected in models.
- Interaction between different hierarchical levels. The load transfer from macroscale to nanoscale is very important. This is because the load acting on each hierarchical level determines its failure behavior. Thus, the behavior of a single level usually influences the overall performance.

All in all, there is still a long way to go to understand the natural construction principles of natural materials, and interdisciplinary collaboration becomes essential to accelerate process. We strongly believe that the field of bio-mimetic materials is extremely promising and that it will possibly bring us to a material revolution.

Bibliography

Ackbarow, T., Chen, X., Keten, S., Buehler, M.J., 2007. Hierarchies, multiple energy barriers, and robustness govern the fracture mechanics of α-helical and β-sheet protein domains. Proc. Natl. Acad. Sci. 104, 16410-16415.

Agnarsson, I., Dhinojwala, A., Sahni, V., Blackledge, T.A., 2009. Spider silk as a novel high performance biomimetic muscle driven by humidity, J. Exp. Biol. 212, 1990-1994.

Arib, R.M.N., Sapuan, S.M., Ahmad, M.M.H.M., Paridah, M.T., Khairul Zaman, H.M.D., 2006. Mechanical properties of pineapple leaf fibre reinforced polypropylene composites. Mater. Des. 27, 391-396.

Ashby, M.F., 2010. Materials selection in mechanical design, 4th ed. Butterworth-Heinemann, Burlington, USA.

Autumn, K., Liang, Y.A., Tonia Hsieh, S., Zesch, W., Chan, W.P., Kenny, T. W., Fearing, R., Full, R.J., 2000. Adhesive force of a single gecko foot-hair. Nature 405, 681-684.

Autumn, K., Peattie, A.M., 2002. Mechanisms of adhesion in geckos. Inter. Comp. Biol. 42, 1081-1090.

Autumn, K., Sitti, M., Liang, Y.A., Peattie, A.M., Hansen, W.R., Sponberg, S., Kenny, T.W., Fearing, R., Israelachvili, J.N., Full, R.J., 2002. Evidence for van der Waals adhesion in gecko setae. Proc. Natl. Acad. Sci. 99, 12252-12256.

Autumn, K., Dittmore, A., Santos, D., Spenko, M., Cutkosky, M., 2006. Frictional adhesion: a new angle on gecko attachment. J. Exp. Biol. 209, 3569-3579.

Autumn, K., Hsieh, S.T., Dudek, D.M., Chen, J., Chitaphan, C., Full, R.J., 2006. Dynamics of geckos running vertically. J. Exp. Biol. 209, 260-272.

Baer, E., Hiltner, A., Morgan, R., 1992. Biological and synthetic hierarchical composites. Phys. Today 45, 60-67.

Balani, K., Patel, R.R., Keshri, A.K., Lahiri, D., Agarwal, A., 2011. Multi-scale hierarchy of Chelydra serpentina: microstructure and mechanical properties of turtle shell. J. Mech. Behav. Biomed. Mater. 4, 1440-1451.

Barthelat, F., Tang, H., Zavattieri, P.D., Li, C.-M., Espinosa, H.D., 2007. On the mechanics of mother-of-pearl: A key feature in the material hierarchical structure. J. Mech. Phys. Solids 55, 306-337.

Becker, N., Oroudjev, E., Mutz, S., Cleveland, J.P., Hansma, P.K., Hayashi, C.Y., Makarov, D.E., Hansma, H.G., 2003. Molecular nanosprings in spider capture-silk threads. Nat. Mater. 2, 278-283.

Becker, T.L., Cannon, R.M., Ritchie, R.O., 2002. Statistical fracture modeling: crack path and fracture criteria with application to homogeneous and functionally graded materials. Eng. Fract. Mech. 69, 1521-1555.

Bejan, A., 2000. Shape and structure, from Engineering to Nature. Cambridge University press, Cambridge, UK.

Bejan, A., 2001. The tree of convective heat stream: Its thermal insulation function and the predicted 3/4-power relation between body heat loss and body size. Int. J. Heat Mass Tran. 44, 699-704.

Bejan, A., 2005. The constructal law of organization in nature: Tree-shaped flows and body size. J. Exp. Biol. 208, 1677-1686.

Bertoldi, K., Bigoni, D., Drugan, W.J., 2008. Nacre: An orthotropic and bimodular elastic material. Compos. Sci. Technol. 68, 1363-1375.

Bezazi, A., Remillat, C., Innocenti, P., Scarpa, F., 2008. In-plane mechanical and thermal conductivity properties of a rectangular-hexagonal honeycomb structures. Compos. Struct. 84, 248-255.

Bhushan, B., Jung, Y.C., 2011. Natural and biomimetic artificial surfaces for superhydrophobicity, self-cleaning, low adhesion, and drag reduction. Prog. Mater. Sci. 56, 1-108.

Biener, J., Hodge, A.M., Hayes, J.R., Volkert, C.A., Zepeda-Ruiz, L.A., Hamza, A.V., Abraham, F.F., 2006. Size effects on the mechanical behavior of nanoporous Au. Nano

Lett. 6, 2379-2382.

Bogdanovich, A., Pastore, C., 1996. Mechanics of textile and laminated composites, 1st ed. Chapman & Hall, London. UK.

Bosia, F., Pugno, N., Buehler, M.J., 2010. Hierarchical simulations for the design of super-tough nanofibres inspired by spider silk. Phys. Rev. E 82, 056103.

Boutry, C., Blackledge, T.A., 2010. Evolution of supercontraction in spider silk: structure–function relationship from tarantulas to orb-weavers. J. Exp. Biol. 213, 3505-3514.

Bozec, L., Horton, M., 2005. Topography and mechanical properties of single molecules of type I collagen using atomic force microscopy. Biophys. J. 88, 4223-4231.

Budiansky, B., 1999. On the minimum weights of compression structures. Int. J. Solids Structures 36, 3677-3708.

Buehler, M.J., Yao, H., Gao, H., Ji, B., 2006. Cracking and adhesion at small scales: atomistic and continuum studies of flaw tolerant nanostructures. Modelling Simul. Mater. Sci. Eng. 14, 799-816.

Buehler, M.J., 2006. Nature designs tough collagen: Explaining the nanostructure of collagen fibrils. Proc. Natl. Acad. Sci. 103, 12285-12290.

Buehler, M.J., Wong, S.Y., 2007. Entropic elasticity controls nanomechanics of single tropocollagen molecules. Biophys. J. 93, 37-43.

Buehler., M.J., Keten, S., Ackbarow, T., 2008. Theoretical and computational hierarchical nano-mechanics of protein materials: Deformation and fracture. Prog. Mater. Sci. 53, 1101-1241.

Buehler, M.J., Ackbarow, T., 2008. Nanomechanical strength mechanisms of hierarchical biological materials and tissues. Comput Methods Biomech Biomed Engin. 11, 595-607.

Buehler, M.J., Yung, Y., 2009. Deformation and failure of protein materials in extreme conditions and disease. Nat. Mater. 8, 175-188.

Buehler, M.J., 2010a. Turning weakness to strength. Nano Today 5, 379-383.

Buehler, M.J., 2010b. Strength in numbers. Nat. Nanotechnology 5, 172-174.

Cai, X., 2007. Wood modifications for valued-added applications using nanotechnology-based approaches. PhD. Thesis, Université Laval, Canada.

Cammarata, R.C., 1994. Surface and interface stress effect in thin films. Prog. Surf. Sci. 46, 1-38.

Cetinkaya, M., Xiao, S., Markert, B., Stacklies, W., Gräter, F., 2011. Silk Fiber Mechanics from Multiscale Force Distribution Analysis. Biophys. J. 100, 1298-1305.

Chang, C.H., 2005. Buckling of inclined columns. Lecture notes in applied and computational mechanics 22, 93-111.

Chen, B., Wu, P.D., Gao, H., 2008. Hierarchical modelling of attachment and detachment mechanisms of gecko toe adhesion. Proc. Roy. Soc. A 464, 1639-1652.

Chen, I.H., Kiang, J.M., Correa, V., Lopez, M.I., Chen, P.Y., McKittrick, J., Meyers, M.A., 2011. Armadillo armor: Mechanical testing and micro-structural evaluation. J. Mech. Behav. Biomed. Mater. 4, 713-22

Chen, P.Y., Lin, A.Y., McKittrick, J., Meyers, M.A., 2008. Structure and mechanical properties of crab exoskeletons. Acta Biomater. 4, 587-596.

Chen, P.Y., Lin, A.Y., Lin, Y.S., Seki, Y., Stokes, A.G., Peyras, J., Olevsky, E.A., Meyers, M.A., McKittrick, J., 2008. Structure and mechanical properties of selected biological materials. J. Mech. Behav. Biomed. Mater. 1, 208-226.

Chen, Q., Pugno, N., 2011a. A parametrical analysis on the elastic anisotropy of woven hierarchical tissues. Adv. Eng. Mater. 13, B377-B394.

Chen, Q., Pugno, N.M., 2011b. Modeling the elastic anisotropy of woven hierarchical tissues. Compos. Part B 42, 2030-2037.

Cheng, Y.T., Rodak, D.E., Wong, C.A., Hayden, C.A., 2006. Effects of micro- and nano-structures on the self-cleaning behaviour of lotus leaves. Nanotechnology 17, 1359-1362.

Christensen, R.M. 1979. Mechanics of composite materials. Wiley-interscience, New York, USA.

Clegg, W.J., Kendall, K., Alford, N.M., Button, T.W., Birchall, J.D., 1990. A simple way to make tough ceramics. Nature 347, 455-457.

Colgin, M. A., Lewis, R., 1998. Spider minor ampullate silk proteins contain new repetitive sequences and highly conserved non-silk-like 'spacer regions'. Protein Sci. 7, 667-672.

Côté, F., Russel, B.P., Deshpande, V.S., Fleck, N.A., 2009. The through-thickness compressive strength of a composite sandwich panel with a hierarchical square honeycomb sandwich core. J. Appl. Mech. 76, 061004.

Cox, B.N., Marshall, D.B., 1994. Concepts for bridged cracks in fracture and fatigue. Acta Metall. Mater. 42, 341-363.

Cox, M.A.J., Driessen, N.J.B., Boerboom, R.A., Bouten, C.V.C., Baaijens, F.P.T., 2008. Mechanical characterization of anisotropic planar biological soft tissues using finite indentation: Experimental feasibility. J. Biomech. 41, 422-429.

Cowin, S.C., Doty, S.B., 2007. Tissue mechanics. Springer, New York, USA.

Curry, J.D., 1977. Mechanical properties of mother of pearl in tension. Proc. R. Soc. Lond. B 196, 443-463.

Curry, J.D., 2010. Mechanical properties and adaptations of some less familiar bony tissues. J. Mech. Behav. Biomed. Mater. 3, 357-372.

Delsanto, P.P., Condat, C.A., Pugno, N., Gliozzi, A., Griffa, M., 2008. A multilevel approach to cancer growth modeling. J. Theor. Biol. 250, 16-24.

Delsanto, P.P., Gliozzi, A., Bruno, C., Pugno, N., Carpinteri, A., 2009. Scaling laws and fractality in the framework of a Phenomenological Approach. Chaos Soliton Fract. 41, 2782-2786.

Devi, L.U., Bhagawan, S.S., Thomas, S., 1998. Mechanical properties of pineapple leaf fiber- reinforced polyester composites. J. Appl. Polym. Sci. 64, 1739-1748.

Du, N., Liu, X., Narayanan, J., Li, L., Lek Min Lim, M., Li, D., 2006. Design of

superior spider silk: From nanostructure to mechanical properties. Biophys. J. 91, 4528-4535.

Du, N., Yang, Z., Liu, X, Li, Y., Xu, H., 2011. Structural origin of the strain-hardening of spider silk. Adv. Funct. Mater. 21, 772-778.

Dugdale D.S., 1960. Yielding of steel sheets containing slits. J. Mech. Phys. Solids, 8, 100-104.

Easterling, K.E., Harrysson, R., Gibson, L.J., Ashby, M.F., 1982. On the mechanics of Basla and other wood, Proc. Roy. Soc. Lond A 383, 31-41.

Emile, O., Le Floch, A., Vollrath, F., 2006. Shape memory in spider draglines. Nature 440, 621.

Espinosa, H.D., Juster, A.L., Latourte, F.J., Loh, O.Y., Gregoire, D., Zavattieri, P.D., 2011. Tablet-level origin of toughening in abalone shells and translation to synthetic composite materials. Nat. Commun., doi: 10.1038/ncomms1172.

Estrin, Y., Dyskin, A.V., Pasternak, E., 2010. Topological interlocking as a material design concept. Mater. Sci. Eng. C 31, 1189-1194.

Euler, M., 2008. Hooke's law and material science projects exploring energy and entropy springs. Phys. Ed. 43,57-61.

Evans, A.G., Suo, Z., Wang, R.Z., Aksay, I.A., He, M.Y., and Hutchinson, J.W., 2001. Model for the robust mechanical behavior of nacre. J. Mater. Res. 16, 2475-2484.

Evans, L.S., Kahn-Jetter, Z., Marks, C., Harmoney, K.R., 2007. Mechanical properties and anatomical components of stems of 42 grass species. J. Torrey. Bot. Soc. 134, 458-467.

Fabritius, H., Sachs, C., Romano, P., Raabe, D., 2009. Influence of structural principles on the mechanics of a biological fiber-Based composite material with hierarchical organization: The exoskeleton of the lobster *Homarus americanus*. Adv. Mater. 21, 391-400.

Fechete, R., Demco, D.E., Blumich, B., Eliav, U., Navon, G., 2003. Anisotropy of collagen fiber orientation in sheep tendon by ^{1}H double-quantum-filtered NMR signals.

J. Magn. Reson. 162,166-175.

Foelix, R., 1996. Biology of Spiders. Oxford University Press, Oxford.

Foo, C.C., Chai, G.B., Seah, L.K., 2007. Mechanical properties of Nomex material and Nomex honeycomb structure. Compos. Struct. 80, 588-594.

Fraztl, P., Weinkamer, R., 2007. Nature's hierarchical materials. Prog. Mater. Sci. 52, 1263-1334.

Fratzl, P., 2007. Biomimetic materials research: What can we really from nature's structural materials? J. R. Soc. Interface 4, 637-642.

Fu, T., Zhao, J., Xu, K., 2007. The designable elastic modulus of 3-D fabric reinforced bio-composites. Mater. Lett. 61, 330-333.

Gan, Y.X., Chen, C., Shen, Y.P., 2005. Three dimensional modeling of the mechanical property of elastomeric open cell foams. Int. J. Solids Structures 42, 6628-6642.

Gao, H., Ji, B., Buehler, M.J., Yao, H., 2004. Flaw tolerant bulk and surface nanostructures of biological systems. Mech. Chem. Biosyst. 1, 37-52.

Gao, H., Yao, H., 2004. Shape insensitive optimal adhesion of nanoscale fibrillar structures. Proc. Natl. Acad. Sci. 101, 7851-7856.

Gao, H., Ji, B., Jäger, I.L., Arzt, E., Fratzl, P., 2006. Materials become insensitive to flaws at nanoscale: Lessons from nature. Proc. Natl. Acad. Sci. 100, 5597-5600.

Gao, H., 2006. Application of fracture mechanics concepts to hierarchical biomechanics of bone and bone-like materials. Int. J. Fracture 138, 101-137.

Geim, A.K., Dubonos, S.V., Grigorieva, I.V., Novoselov, K.S., Zhukov, A.A, Shapoval, S.Y.U., 2003. Microfabricated adhesive mimicking gecko foot-hair, Nat. Mater. 2, 461-463.

George, J., Bhagawan, S.S., Prabhakaran, N., Thomas, S., 1995. Short pineapple-leaf-fiber- reinforced low-density polyethylene composites. J. Appl. Polym. Sci. 57, 843-854.

George, J., Onodera, J., Miyata, T., 2008. Biodegradable honeycomb collagen scaffold

for dermal tissue engineering. J. Biomed. Mater. Res. A 87, 1103-1111.

Gibbs, J.W., 1961. The scientific papers of J. Willard Gibbs, Thermodynamics, Vol. 1: Thermodynimcs. Dover, New York, USA.

Gibson, L.J., Ashby, M.F., Schajer, G.S., Robertson, C.J., 1982. The mechanics of two-dimensional cellular materials. Proc. R. Soc. Lond. A 382, 25-42.

Gibson, L.J., Ashby, M.F., 1997. Cellular solids: structure and properties, 2nd ed. Cambridge University Press, Cambridge, UK.

Gibson, L.J., 2005. Biomechanics of cellular solids. J. Biomech. 38, 377-399.

Gibson, R.F., 1994. Principles of composite material mechanics, 1st ed. McGraw-Hill, New York, USA.

Giesa, T., Arslan, M., Pugno, M., Buehler, M.J., 2011. Nanoconfinement of spider silk fibrils begets superior strength, extensibility, and toughness. Nano Lett. doi:10.1021/nl203108t.

Gilbert, S.F., Loredo, G.A., Brukman, A., Burke, A.C., 2001. Morphogenesis of the turtle shell: The development of a novel structure in tetrapod evolution. Evo. Dev. 3, 47-58.

Gioia, G., Dai, X., 2006. Surface stress and reversing size effect in the initial yielding of ultrathin films. J. Appl. Mech. 73, 254-258.

Godline, J.M., Guerette, P.A. Ortlepp, C.S., Savage, K.N., 1999. The mechanical design of spider silks: From fibroin sequence to mechanical function. J. Exp. Biol. 202, 3295-3303.

Green, D.W., Winandy, J.E., Kretschmann, D.E., 1999. Mechanical properties of wood. In: Wood Handbook: Wood as an Engineering Material. U.S. Dapartment of Agriculture Forest Service, Forest Products Laboratory, Madison, WI, chap. 4.

Guiot, C., Pugno, N., Delsanato, P.P., 2006. An elastomechanical model for tumor invasion. Appl. Phys. Lett. 89, 233901.

Guiot, C., Pugno, N., Delsanato, P.P., Deisboeck, T.S., 2007. Physical aspects of cancer invasion., Phys. Biol. 5, 1-6.

Gurtin, M.E., Murdoch, A.I., 1975. A continuum theory of elastic material surface. Arch. Rat. Mech. Anal. 57, 291-323.

Hansma,W.R., Autumn, K., 2006. Evidence for self-cleaning in gecko setae. Proc. Natl. Acad. Sci. 102, 385-389.

Hayashi, C.Y., Lewis, R., 1998. Evidence from flagelliform silk cDNA for the structural basis of elasticity and modular nature of spider silks. J. Mol. Biol. 275, 773-784.

Hodge, A.M., Biener J., Hayes, J.R., Bythrow, P.M., Volkert C.A., Hamza, A.V., 2007. Scaling equation for yield strength of nanoporous open-cell foams. Acta Mater. 55, 1343-1349.

Hofstetter, K, Gamstedt, E.K., 2008. Hierarchical modelling of microstructural effects on mechanical properties of wood: A review. Holzforschung 63, 130-138.

Hollister, S.J., 2005. Porous scaffold design for tissue engineering. Nat. Mater. 4, 518-524.

Huber, G., Mantz, H., Spolenak, R., Mecke, K., Jacobs, K., Gorb, S.N., Arzt, E., 2005. Evidence for capillarity contributions to gecko adhesion from single spatula nanomechanical measurements. Proc. Natl. Acad. Sci. 102, 16293-16296.

Huemmerich, D., Scheibel, T., Vollrath, F., Cohen, S., Gat, U., Ittah, S., 2004. Novel assembly properties of recombinant spider dragline silk proteins. Curr. Biol. 14, 2070-2074.

Ito, M., Kawakami, Y., Ichinose, Y., Fukashiro, S., Fukunaga, T., 1998. Nonisometric behavior of fascicles during isometric contractions of a human muscle. J. Appl. Physiol. 85, 1230-1235.

Jaccodine, R.J., 1963. Surface energy of germanium and silicon. J. Electrochem. Soc. 110, 524-527.

Jackson, A.P., Vincent, J.F.V., Turner, R.M., 1988. The mechanical design of nacre. Proc. R. Soc. Lond. B 234, 415-440.

Jackson, A.P., Vincent, J.F.V., 1989. A physical model of nacre. Compos. Sci. Eng. 36,

255-266.

Jäger, I., Fratzl, P., 2000. Mineralized collagen fibrils: A mechanical model with staggered arrangemen of mineral particles. Biophys. J. 79, 1737-1746.

Ji, B., Gao, H.J., 2004. Mechanical properties of nanostructures of biological material. J. Mech. Phys. Solids 52, 1963-1990

Ji, B., 2008. A study of the interface strength between protein and mineral in biological materials. J. Biomech. 41, 259-266.

Kamat, S., Su, X., Ballarini, R., Heuer, A.H., 2000. Structural basis for the fracture toughness of the shell of the conch *Strombus gigas*. Nature 405, 1036-1040.

Kamat, S., Kessler, H., Ballarini, R., Nassirou, M., Heuer, A.H., 2004. Fracture mechanisms of the *Strombus gigas* conch shell: II-micromechanics analyses of multiple cracking and large-scale crack bridging. Acta Mater. 52, 2395-2406.

Kaplan, D.L., 1998. Mollusc shell structures: Novel design strategies for synthetic materials. Curr. Opin. Solid State Mater. Sci. 3, 232-236.

Karam, G.N., Gibson, L.J., 1995a. Elastic buckling of cylindrical shells with elastic cores-I. Analysis. Int. J. Solids Strucutres 32, 1259-1283.

Karam, G.N., Gibson, L.J., 1995b. Elastic buckling of cylindrical shells with elastic cores-Ⅱ. Experiments. Int. J. Solids Strucutres 32, 1284-1306.

Kato, Y.P., Christiansen, D.L., Hahn, R.A., Shieh, S.J., Goldstein, J.D., Silver, F.H., 1989. Mechanical properties of collagen fibers: A comparison of reconstituted and rat tail tendon fibers. Biomater. 10, 38-41.

Kelly, S.P., Sensenig, A., Lorentz, K.A., Blackledge, T.A., 2011. Damping capacity is evolutionarily conserved in the radial silk of orb-weaving spiders. Zoology 114 , 233-238.

Keten, S., Xu, Z., Ihle, B., Buehler, M.J., 2010. Nanoconfinement controls stiffness, strength and mechanical toughness of β-sheet crystals in silk. Nat. Mater. 9, 359-367.

Kiely, J.D., Houston, J.E., 1998. Nanomechanical properties of Au(111), (001), and (110) surfaces, Phys. Rev. B 57, 12588-12594.

Krauss, S., Monsonego-Ornan, E., Zelzer, E., Fratzl, P., Shahar, R., 2009. Mechanical function of a complex three-dimensional suture joining the bony elements in the shell of the red-eared slider turtle. Adv. Mater. 21, 407-412.

Kuraku, S., Usuda, R., Kuratani, S., 2005. Comprehensive survey of carapacial ridge-specific genes in turtle implies co-option of some regulatory genes in carapace evolution. Evo. Dev. 7, 3-17.

Lakes, R., 1993. Materials with structural hierarchy. Nature 361, 511-515.

Launey, M.E., Ritchie, R.O., 2009. On the fracture toughness of advanced materials. Adv. Mater. 21, 2103-2110.

Lavagnino, M., Arnoczky, S.P., Kepich, E., Caballero, O., Haut, R.C., 2008. A finite element model predicts the mechanotransduction response of tendon cells to cyclic tensile loading. Biomech. Model. Mechan. 7, 405-416.

Lee, S.K., Byun, J.H., Hong, S.H., 2003. Effect of fiber geometry on the elastic constants of the plain woven fabric reinforced aluminum matrix composites. Mater. Sci. Eng. 347, 346-358.

Lee, D., Wei, X., Chen, X., Zhao, M., Jun S.C., Hone J., Herbert, E.G., Oliver W.C., Kysarj, W., 2007. Microfabrication and mechanical properties of nanoporous gold at the nanoscale. Scripta Mater. 56, 437-440.

Lemos, R.R., Epstein, M., Herzog, W., 2008. Modeling of skeletal muscle: The influence of tendon and aponeuroses compliance on the force–length relationship. Med. Biol. Eng. Comput. 46, 23-32.

Lepore, E., Antoniolli, F., Buono, M., Brianza, S., Carpinteri, A., Pugno, N., 2008. Preliminary experiments on adhesion of in vivo geckos. J. Nanomater. 194, 524-528.

Li, X., Chang, W.C., Chao, Y.J., Wang, R., Chang, M., 2004. Nanoscale structural and mechanical characterization of a natural nanocomposite material: The shell of red abalone. Nano Lett. 4, 613-617.

Li, X., 2007. Nanoscale structural and mechanical characterization of natural nanocomposites: Seashells. J. Miner. Met. Mater. Soc. 59, 71-74.

Lichtwark, G.A., Wilson, A.M., 2005. In vivo mechanical properties of the human Achilles tendon during one-legged hopping. J. Exp. Biol. 208, 4715-4725.

Lin, A.Y.M., Meyers, M.A., Vecchio, K.S., 2006. Mechanical properties and structure of *Strombus Giga*, *Tridacna Gigas*, and *Haliotis Rufescens* seashells: A comparative study. Mater. Sci. Eng. C 26, 1380-1389.

Lin, A.Y.M., Meyers, M.A., 2009. Interfacial shear strength in abalone nacre. J. Mech. Behav. Biomed. Mater. 2, 607-612.

Liu, C., Xia, Z., Czernuszka, J.T., 2007. Design and development of three- dimensional scaffolds for tissue engineering. Chem. Eng. Res. Des. 85, 1051-1064.

Liu, Y., Shao, Z., Vollrath, F., 2005. Relationships between supercontraction andmechanical properties of spider silk. Nat. Mater. 4, 901-905.

Lynch, H.A., Johannessen, W., Wu, J.P., Jawa, A., Elliott, D.M., 2003. Effect of fiber orientation and strain rate on the nonlinear uniaxial tensile material properties of tendon. J. Biomech. Eng. 125, 726-731.

Ma, P.X., 2004. Scaffolds for tissue fabrication. Mater. Today 7, 30-40.

Magnusson, S.P., Hansen, M., Langberg, H., Miller, B., Haraldsson, B., Westh, E.K., Koskinen, S., Aagaard, P., Kjaer, M., 2007. The adaptability of tendon to loading differs in men and women. Int. J. Exp. Pathol. 88, 237-240.

Mita, K., Ichimura, S., James, T., 1994. Highly repetitive structure and its organization of the silk fibroin gene. J. Mol. Evol. 38, 583-592.

Mcbride, T.M., Chen, J.L., 1997. Unit-cell geometry in plain weave fabrics during shear deformation. Compos. Sci. Technol. 57, 345-351.

Meyers, M.A., Chen, P.Y., Lin, A.Y.M., Seki, Y., 2008. Biological materials: Structure and mechanical properties. Prog. Mater. Sci. 53, 1-206.

Meyers, M.A., Lin, A.Y.M., Chen, P.Y., Muyco, J., 2008. Mechanical strength of abalone nacre: Role of the soft organic layer. J. Mech. Behav. Biomed. Mater. 1, 76-85.

Miller, R.E., Shenoy, V.B., 2000. Size-dependent elastic properties of nanosized

structural elements. Nanotechnology 11, 139-147.

Mishra, S., Mohanty, A.K., Drzal, L.T., Misra, M., Hinrichsen, G., 2004. A review on pineapple leaf fibers, sisal fibers and their biocomposites. Macromol. Mater. Eng. 289, 955-974.

Misra, A., Huang, S., 2011. Effect of loading induced anisotropy on the shear behavior of rough interfaces. Tribo. Int. 44, 627-634.

Moon, R.J., 2008. Nanomaterials in the forest products industry. McGraw-Hill Yearbook of Science and Technology, 225-228.

Moutos, F.T., Freed, L.E., Guilaka, F., 2007. A bio-mimetic three-dimensional woven composite scaffold for functional tissue engineering of cartilage. Nat. Mater. 6, 162-167.

Mow, V.C., Radcliffe, A., Woo, SL-Y., 1990. Biomechanics of diarthroidal joints, 1st ed. Springer, New York, USA.

Munch, E., Launey, M.E., Alsem, D.H., Saiz, E., Tomsia, A.P., Ritchie, R.O., 2008. Tough, bio-inspired hybrid materials. Science 322, 1516-1520.

Niklas, K.J., 1997a. Relative resistance of hollow, septate internodes to twisting and bending. Ann. Botany 80, 275-287.

Niklas, K.J., 1997b. The structural efficiency of orthotropic stalks, stems and tubes. Ann. Botany 80, 437-448.

Niklas, K.J., 1998. Modes of mechanical failure of hollow, septate stems. Ann. Botany 81, 11-21.

Nikolov, S., Petrov, M., Lymperakis, L., Friák, M., Sachs, S., Fabritius, H., Raabe, D., Neugebauer, J., 2010. Revealing the design principles of high-performance biological composites using Ab initio and multiscale simulations: The example of lobster vuticle. Adv. Mater. 22, 519-526.

Nova, A., Keten, S., Pugno, N., Redaelli, A., Buehler, M.J., 2010. Molecular and nanostructural mechanisms of deformation, strength and toughness of spider silk fibrils. Nano lett. 10, 2626-2634.

Ouyang G., Wang C.X., Yang G.W., 2009. Surface energy of nanostructural materials with negative curvature and related size effects. Chem. Rev. 109, 4221-4247.

Ouyang G., Li X. L., Tan X., Yang G.W., 2007. Anomalous Young's modulus of a nanotube. Phys. Rev. B 76, 193406.

Ouyang G., Yang G.W., Sun C.Q., Zhu W.G., 2008. Nanoporous structures: smaller is stronger. Small 4, 1359-1362.

Pantano, A., Pugno, N., Gorb, S., 2011. Numerical simulations demonstrate that the double tapering of the spatualae of lizards and insects maximize both attachment resistance and stability. Int. J. Fract. DOI 10.1007/s10704-011-9596-8

Papka, S.D., Kyriakides, S., 1994. In-plane compressive response and crushing of honeycombs. J. Mech. Phys. Solids 42, 1499-1532.

Papka, S.D., Kyriakides, S., 1998a. In-plane crushing of a polycarbonate honeycomb. Int. J. Solids Structures 35, 239-267.

Papka, S.D., Kyriakides, S., 1998b. Experiments and full-scale numerical simulations of in-plane crushing of a honeycomb. Acta Mater. 46, 2765-2776.

Paulsson, M., Yurchenco, P.D., Ruben, G.C., Engel, J., Timpl, R., 1987. Structure of low density heparan sulfate proteoglycan isolated from a mouse tumor basement membrane. J. Mol. Biol. 197, 297-313.

Pérez-Rigueiro, P., Elices, M., Plaza, G., Real, J.I., Guinea, G.V., 2005. The effect of spinning forces on spider silk properties. J. Exp. Biol. 208, 2633-2639.

Persson, B.N.J., 2003. On the mechanism of adhesion in biological systems. J. Chem. Phys. 118, 7614-7621.

Persson, B.N.J., Gorb, S., 2003. The effect of surface roughness on the adhesion of elastic plates with application to biological systems. J. Chem. Phys. 119, 11437-11444.

Pidaparti, R.M.V., Chandran, A., Takano, Y., Turner. C.H., 1996. Bone mineral lies mainly outside collagen fibrils: Prediction of a composite model for osteonal bone. J. Biomech. 29, 909-916.

Porter, D., Vollrath, F., Shao, Z., 2005. Predicting the mechanical properties of spider

silk as a model nanostructured polymer. Eur. Phys. J. E 16, 199-206.

Pugno, N.M., 2002. A quantized Griffith's criterion, Fracture Nanomechanics, Meeting of the Italian Group of Fracture, September 25-26, Vigevano, Italy.

Pugno, N.M., Ruoff, R., 2004. Quantized fracture mechanics. Phil. Mag. 84, 2829-2845.

Pugno, N.M., 2006. Mimicking nacre with super-nanotubes for producing optimized super-composites. Nanotechnology 17, 5480-5484.

Pugno, N.M., 2007. Young's modulus reduction of defective nanotubes. Appl. Phys. Lett. 90, 043106.

Pugno, N., 2008. Spiderman gloves. Nano Today, 3, 35-41.

Pugno, N., Carpinteri, A., 2008. Design of micro-nanoscale bio-inspired hierarchical materials. Phil. Mag. Lett. 88, 397-405.

Pugno, N., Carpinteri, A., Delsanto. P.P., Bosia, F., Gliozzi, A., 2008. Phenomenological approach to mechanical damage growth analysis. Phys. Rev. E 78, 046103-1/5.

Pugno, N., Bosia, F., Carpinteri, A., 2008. Multiscale stochastic simulations for tensile testing of nanotube-based macroscopic cables. Small 4, 1044-1052.

Pugno, N., Lepore, E., 2008a. Living tokay geckos display adhesion times following the Weibull Statistics. J. Adhesion 89, 949-962.

Pugno, N., Lepore, E., 2008b. Observation of optimal gecko's adhesion on nanorough surfaces. Biosys. 94, 218-222.

Pugno, N., 2010. Graded cross-links for stronger nanomaterials. Mater. Today 13, 40-43.

Prowse, M.S., Wilkinson, M., Puthoff, J.B., Mayer, G., Autumn, K., 2011. Effects of humidity on the mechanical properties of gecko setae. Acta Mater. 7, 733-738.

Qin, Z., Kreplak, L., Buehler, M.J., 2009. Hierarchical structure controls nanomechanical properties of vimentin intermediate filaments. PLoS ONE 4, e7294.

Qin, Z., Buehler, M.J., 2011. Flaw tolerance of nuclear intermediate filament lamina under extreme mechanical deformation. ACS Nano 5, 3034-3042.

Qing, H., Mishnaevsky, L., 2009. 3D hierarchical computational model of wood as a cellular material with fibril reinforced, heterogeneous multiple layers. Mech. Mater. 41, 1034-1049.

Quapp, K.M., Weiss, J.A., 1998. Material characterization of human medial collateral ligament. Biomech. Eng. 120, 757-763.

Raabe, D., Sachs, C., Romano, P., 2005. The crustacean exoskeleton as an example of a structurally and mechanically graded biological nanocomposite material. Acta Mater. 53, 4281-4292.

Raabe, D., Romano, P., Sachs, C., Al-Sawalmih, A., Brokmeier, H.-G., Yi, S.-B., Servos, G., Hartwig, H.G., 2005. Discovery of a honeycomb structure in the twisted plywood patterns of fibrous biological nanocomposite tissue. J. Crystal Growth 283, 1-7.

Raabe, D., Romano, P., Sachs, C., Fabritius, H., Al-Sawalmih, A., Yi, S.-B., Servos, G., Hartwig, H.G., 2006. Microstructure and crystallographic texture of the chitin–protein network in the biological composite material of the exoskeleton of the lobster *Homarus americanus*. Mater. Sci. Eng. A 421, 143-153.

Raabe, D., Al-Sawalmih, A., Yi, S.B., Fabritius, H., 2007. Preferred crystallographic texture of a-chitin as a microscopic and macroscopic design principle of the exoskeleton of the lobster *Homarus americanus*. Acta Biomater. 3, 882-895.

Rhee, H., Horstemeyer, M.F., Hwang, Y., Lim, H., El Kadiri, H., Trim, W., 2009. A study on the structure and mechanical behavior of the *Terrapene carolina* carapace: A pathway to design bio-inspired synthetic composites. Mater. Sci. Eng. C 29, 2333-2339.

Rhee, H., Horstemeyer, M.F., Ramsay, A., 2011. A study on the structure and mechanical behavior of the *Dasypus novemcinctus* shell. Mater. Sci. Eng. C 31, 363-369.

Rieppel, O., 2009. How did the turtle get its shell? Science 325, 154-155.

Rim, J.E., Zavattieri, P., Juster, A., Espinosa, H.D., 2011. Dimensional analysis and parametric studies for designing artificial nacre. J. Mech. Behav. Biomed. Mater. 4, 190-211.

Ritchie, R.O., 1988. Mechanisms of fatigue crack propagation in metals, ceramics and composites: Role of crack tip shielding. Mater. Sci. Eng. A 103, 15-28.

Ritchie, R.O., Buehler, M.J., Hansma, P., 2009. Plascity and toughness in bone. Phys. Today 62, 41-47.

Roark, R.J., Young, W.C., 1975. Formulas for stress and strain, 5th ed. McGraw-Hill Book Co. Inc., New York, USA.

Romano, P., Fabritius, H., Raabe, D., 2007. The exoskeleton of the lobster *Homarus americanus* as an example of a smart anisotropic biological material. Acta Biomater. 3, 301-309.

Rousseau, M., Lopez, E., Couté, A., Mascarel, G., Smith, D.C., Naslain, R., Bourrat, X., 2005. Sheet nacre growth mechanism: A Voronoi model. J. Struct. Biol. 149, 149-157.

Rousseau, M., Meibom, A., Gèze, M., Bourrat, X., Angellier, M., Lopez, E., 2009. Dynamics of sheet nacre formation in bivalves. J. Struct. Biol. 165, 190-195.

Sachs, C., Fabritius, H., Raabe, D., 2006. Experimental investigation of the elastic-plastic deformation of mineralized lobster cuticle by digital image correlation. J. Struct. Biol. 155, 409-425.

Sachs, C., Fabritius, H., Raabe, D., 2006. Hardness and elastic properties of dehydrated cuticle from the lobster *Homarus americanus* obtained by nanoindentation. J. Mater. Res. 21, 1987-1995.

Sachs, C., Fabritius, H., Raabe, D., 2008. Influence of microstructure on deformation anisotropy of mineralized cuticle from the lobster *Homarus americanus*. J. Struct. Biol. 161, 120-132.

Sadeghian, H., Yang, C.K., Goosen, J., Bossche, A., Staufer, U., French, P.J., Keulen, F., 2010. Effects of size and defects on the elasticity of silicon nanocantilevers. J. Micromech. Microeng. 20, 064012.

Sasaki, N., Odajima, S., 1996a. Stress-strain curve and Young's modulus of a collagenmolecule as determined by the X-ray diffraction technique. J. Biomech. 29, 655-658.

Sasaki, N., Odajima, S., 1996b. Elongation mechanism of collagen fibrils and force–strain relations of tendon at each level of structural hierarchy. J. Biomech. 29, 1131-1136.

Savage, K.N., Gosline, J.M., 2008. The role of proline in the elastic mechanism of hydrated spider silks. J. Exp. Biol. 211, 1948-1957.

Schäffer, T.E., Zanetti, C.I., Proksch, R., Fritz, M., Walters, D.A., Almqvist, N., Zaremba, C.M., Belcher, A.M., Smith, B.L., Stucky, G.D., Morse, D.E., Hansma, P.K., 1997. Does abalone nacre form by heteroepitaxial nucleation or by growth through mineral bridges. Chem. Mater. 9, 1731-1740.

Schulgasser, K., Witztum, A., 1997. On the strength of herbaceous vascular plant stems. Ann. Botany 80, 35- 44.

Scott, S.H., Loeb, G.E., 1995. Mechanical properties of aponeurosis and tendon of the cat soleus muscle during whole muscle isometric contractions. J. Morph. 224, 73-86.

Seki, Y., Schneider, M.S., Meyers, M.A., 2011. Structure and mechanical behavior of a toucan beak. Acta Mater. 53, 5281-5296.

Sen, D., Buehler, M.J., 2010. Atomistically-informed mesoscale model of deformation and fracture of hierarchical silica nanocomposites. Int. J. Appl. Mech. 2, 699-717.

Sen, D., Garcia, A., Buehler, M.J., 2011. Mechanics of nano-honeycomb silica structures: A size-dependent brittle-to-ductile transition. J. Nanomech. Micromech. Accepted.

Shankar, M.R., King, A.H., 2007. How surface stresses lead to size-dependent mechanics of tensile deformation in nanowires. Appl. Phys. Lett. 90, 141907

Shenoy, V.B., 2005. Atomistic calculations of elastic properties of metallic fcc crystal surfaces. Phys. Rev. B 71, 094104-1.

Silver, F.H., Freeman, J.W., Seehra, G.P., 2003. Collagen self-assembly and the

development of tendon mechanical properties. J. Biomech. 36, 1529-1553.

Smith, B.L., Schäffer, T.E., Viani, M., Thompson, J.B., Frederick, N.A., Kindt, J., Belcher, A., Stucky, G.D., Morse, D.E., Hansma, P.K., 1999. Molecular mechanistic origin of the toughenss of natural adhesives, fibres and composites. Nature 399,761-763.

Song, F., Soh, A.K., Bai, Y.L., 2003. Structural and mechanical properties of the organic matrix layers of nacre. Biomater. 24, 3623-3631.

Srinivasan, A.V., Haritos, G.K., Hedberg, F.L., 1991. Biomimetics: Advancing man-made materials through guidance from nature. Appl. Mech. Rev. 44, 463-481.

Stempflé, P.H., Pantalé, O., 2007. Friction-induced sheet nacre fracture: Effects of nano-shocks on cracks location. Nanotechnology 4, 712-729.

Stempflé, P.H., Pantalé, O., Rousseau, M., Lopez, E., Bourrat, X., 2010. Mechanical properties of the elemental nanocomponents of nacre structure. Mater. Sci. Eng. C 30, 715-721.

Sundararajan, S., Bhushan, B., 2002. Development of AFM-based techniques to measure mechanical properties of nanoscale structures. Sensor Actuat. A-Phys. 101, 338-351.

Tang, H., Barthelat, F., Espinosa, H.D., 2007. An elasto-viscoplastic interface model for investigating the constitutive behavior of nacre. J. Mech.Phys. Solids 55, 1410-1538.

Tang, H., Buehler, M.J., Moran, B., 2009. A constitutive model of soft tissue: From nanoscale collagen to tissue continuum. Ann. Biomed. Eng. 37, 1117-1130.

Taylor, C.M., Smith, C.W., Miller, W., Evans, K.E., 2011. The effects of hierarchy on the in-plane elastic properties of honeycombs. Int. J. Solids Structures 48, 1330-1339.

Thompson, D.W., 1945. On growth and form. Cambridge University Press, New York, pp. 789-804.

Tian, Y., Pesika, N., Zeng, H., Rosenberg, K., Zhao, B., McGuiggan, P., Autumn, K., 2006. Adhesion and friction in gecko toe attachment and detachment. Proc. Natl. Acad.

Sci. 103, 19320-19325.

Timoshenko, S.P., Gere, J., 1961. Theory of elastic stability, 2nd ed., McGraw-Hill Company, New York, USA.

Tolf, G., 1985. Saint-Venant bending of an orthotropic beam. Comp. Struct. 4, 1-14.

Truman, R.W., Kumaresan, J.A., Mcdonough, C.M., Job, C.K., Hastings, R.C., 1991. Seasonal and spatial trends in the detectability of leprosy in wild Armadillos. Epidemiol. Infect. 106, 549-560.

Truman, R., 2008. Armadillos as a source of infection for leprosy. South. Med. J. 101, 581-582.

Valle, L.D., Nardi, A., Toni, M., Emera, D., Alibardi, L., 2009. Beta-keratins of turtle shell are glycine-proline-tyrosine rich proteins similar to those of crocodilians and birds. J. Anat. 214, 284-300.

Van der Rijt, J.A.J., Van der Werf, K.O., Bennink, M.L., Dijkstra, P.J., Jan, F.J., 2006. Micromechanical testing of individual collagen fibrils. Macromol. Biosci. 6, 697-702.

Varenberg, M., Pugno, N., Gorb, S., 2010. Spatulate structures in biological fibrillar adhesion. Soft Matter 6, 3269-3272.

Venner, S., Jérôme Casas, 2005. Spider webs designed for rare but life-saving catches. Proc. R. Soc. B 272, 1587–1592.

Vickaryous, M.K., Hall, B.K., 2006. Osteoderm morphology and development in the nine-banded Armadillo, *Dasypus novemcinctus* (Mammalia, Xenarthra, Cingulata). J. Morph. 267, 1273-1283

Vollrath, F., 2000. Strength and structure of spiders' silks. Rev. Mol. Biotechnol. 74, 67-83.

Vollrath, F., Madsen, B., Shao, Z., 2001. The effect of spinning conditions on the mechanics of a spider's dragline silk. Proc. R. Soc. Lond. B 268, 2339-2346.

Wadley, H.N.G., 2006. Multifunctional periodic cellular metals. Phil. Trans. R. Soc. A 364, 31-68

Wang, D., 2009. Impact behavior and energy absorption of paper honeycomb sandwich panels. Int. J. Impact Eng. 36, 110-114.

Wang, D., Wang, Z., Liao, Q., 2009. Energy absorption diagrams of paper honeycomb sandwich structures. Packag. Technol. Sci. 22, 63-67.

Wang, G.F., Feng, X.Q., 2009. Surface effects on buckling of nanowires under uniaxial compression. Appl. Phys. Lett. 94, 141913.

Wang, J., Duan, H.L., Huang, Z.P., Karihaloo, B.L., 2006. A scaling law for properties of nano-structured materials. Proc. R. Soc. A. 462, 1355-1363.

Wang, R.Z., Suo, Z., Evans, A.G., Yao, N., Aksay, I.A., 2001. Deformation mechanisms in nacre. J. Mater. Res. 16, 2485-2493.

Wang, X.S., Xia, R., 2010. Size-dependent effective modulus of hierarchical nanoporous foams. Europhys. Lett. 92, 16004.

Warren, W.E., Kraynik, A.M., 1987. Foam mechanics: The linear elastic response of two-dimensional spatially periodic cellular materials. Mech. Mater. 6, 27-37.

Wegst, U.G.K., Ashby, M.F., 2004. The mechanical efficiency of natural materials. Phil. Mag. 84, 2167-2181.

Wegst, U.G.K., Ashby, M.F., 2007. The structural efficiency of orthotropic stalks, stems and tubes. J. Mater. Sci. 42, 9005-9014.

West, G.B., Brown, J.H., Enquist, B.J., 1997, A general model for the origin of allometric scaling laws in biology. Science 276, 122-126.

Williams, M.L., 1957. On the stress distribution at the base of a stationary crack. J. Appl. Mech. 79, 109-114.

Wong, E.W., Sheehan, P.E., Lieber, C.M., 1997. Nanobeam mechanics: Elasticity, strength and toughness of nanorods and nanotubes. Science 277, 1972-1975.

Work, R.W., 1977. Dimensions, brief ringences, and force-elongation behaviour of major and minor ampullate silk fibres from orb-web-spinning spiders-the effect of wetting on these properties. Text. Res. J. 47, 650–662.

Xue, Z.Y., Hutchinson, J.W., 2006. Crush dynamics of square honeycomb sandwich cores. Int. J. Numer. Methods Eng. 65, 2221-2245.

Yang, L., 2008. Mechanical properties of collagen fibrils and elastic fibers explored by AFM. Ph. D. Thesis, University of Twente, Netherlands.

Yang, L., Fitie′, C.F.C., Van der Werf, K.O., Benninkb, M.L., Dijkstra, P.J., Jan, F.J., 2008. Mechanical properties of single electrospun collagen type I fibers. Biomater. 29, 955-962.

Yang, Z., Lu, Z., Zhao Y.P., 2009. Atomistic simulation on size-dependent yield strength and defects evolution of metal nanowires. Comp. Mater. Sci. 46, 142-150.

Yao, H., Gao, H., 2006. Mechanics of robust and releasable adhesion in biology: Bottom–up designed hierarchical structures of gecko. J. Mech. Phys. Solids 54, 1120-1146.

Yao, H., Gao, H., 2007. Multi-scale cohesive laws in hierarchical biological materials, Int. J. Solids Structures 44, 8177-8193.

Yao, H., Dao, M., Carnelli, D., Tai, K., Ortiz, C., 2011. Size-dependent heterogeneity benefits the mechanical performance of bone. J. Mech. Phys. Solids 59, 64-74.

Yin, L.Z., Elliott, D.M., 2004. A biphasic and transversely isotropic mechanical model for tendon: application to mouse tail fascicles in uniaxial tension. J. Biomech. 37, 907-916.

Zakeri, A.A., Mazraehshahi, H.T., 2010. Experimental study on mechanical properties of aircraft honeycomb sandwich structures. EPJ Web of Conferences, 6.

Zhang, K., Duan, H.L., Karihaloo, B.L., Wang, J., 2010. Hierarchical, multilayered cell walls reinforced by recycled silk cocoons enhance the structural integrity of honeybee combs. Proc. Natl. Acad. Sci. 107, 9502-9506.

Zhang, J., Ashby, M.F., 1992. Buckling of honeycombs under in-plane biaxial stresses. Int. J. Mech. Sci. 34, 491-509.

Zhang, E.J., Wang, T.J., Chen, X., 2010. Effect of surface/interface stress on the plastic deformation of nanoporous materials and nanocomposites. Int. J. Plasticity 26,

957-975.

Zhang, Z., Zhang, Y.W., Gao, H., 2011. On optimal hierarchy of load-bearing biological materials. Proc. Biol. Sci. 278, 519-525

Zheng, X.P., Cao, Y.P., Li, B., Feng, X.Q., Wang, G.F., 2010. Surface effects in various bending-based test methods for measuring the elastic property of nanowires. Nanotechnology 21, 205702

Zhou, L.G., Huang, H.C., 2004. Are surfaces elastically softer or stiffer? Appl. Phys. Lett. 2004, 84, 1940-1942.

Zhou, H., Zhang, Y., 2005. Hierarchical chain model of spider capture silk elasticity. Phys. Rev. Lett., 94, 028104.